

# **Microswimmers and microflyers in various complex environments**

**Inaugural dissertation**

**for the attainment of the title of doctor  
in the Faculty of Mathematics and Natural Sciences  
at the Heinrich Heine University Düsseldorf**

presented by

**Soudeh Jahanshahi**  
from Kerman, Iran

Düsseldorf, October 2019

from the institute for Theoretical Physics II: Soft Matter  
at the Heinrich Heine University Düsseldorf

Published by permission of the  
Faculty of Mathematics and Natural Sciences at  
Heinrich Heine University Düsseldorf

**Supervisor:** Prof. Dr. Hartmut Löwen

**Co-supervisor:** Priv.-Doz. Dr. Alexei Ivlev

**Date of the oral examination:** 09/12/2019

# Abstract

Active Brownian particles can propel themselves by taking energy from their environment and converting it into mechanical motion while being subject to the fluctuating random kicks of the surrounding medium. The dynamics of such self-propelled particles, hence, exhibits a nonequilibrium Brownian phenomenon. The core functionalities of active Brownian particles include transport, sensing, and manipulation.

For microscopic active Brownian particles *swimming* in a Newtonian liquid (*microswimmers*), viscous forces are dominant and inertial effects are negligible relative to the viscous effects. One of the most popular descriptions of microswimmers is provided by *active Brownian motion*, wherein the overdamped dynamics is modeled through Gaussian white noise as solvent kicks and an effective self-propulsion force. Inertia becomes relevant in the dynamics for micron-sized active Brownian particles *flying* in a gaseous medium (*microflyers*), where viscous friction becomes such small that the inertial effects get dominant. The dynamics is then coined as *active Langevin motion*. Here we study the behavior of active Brownian particles moving in a plane both analytically and using computer simulations. Our studies include both active Langevin motion and its overdamped counterpart, i.e. active Brownian motion.

We observe a distinct *inertial delay* between orientation and velocity of microflyers. The velocity of microflyers –unlike microswimmers– does not instantaneously pursue their orientation. We characterize the inertial delay via the cross correlations of velocity and orientation and derive the corresponding analytic expression describing inertial delay. Using analytical calculations we demonstrate that inertia significantly influences the dynamics and enables novel control strategies in active systems. Our theoretical predictions are confirmed by experiments. We also generalize the equations of motion to time-dependent parameters. Assuming a slow power-law time-dependence for these parameters, we predict an anomalous diffusion involving long-time dynamics.

we report on the design, experimental realization and characterization of an in-situ adjustable trapping mechanism for microswimmers which does not require any body-forces (or associated torques) and is entirely based on self-propulsion. In particular, this trapping mechanism solely hinges on systematic force-free rotations of active colloids towards the center of the trap. The force-free rotations originate from a motility gradient. The fact that the trapping mechanism acts on the orientation of the microswimmers, rather than on their center of mass,

---

facilitates controllably transfer of active particles over a potential barrier using the trap as a tweezer. This force-free trapping mechanism also enables extracting coupling coefficients of microswimmers to external fields that can cause a better understanding of their mutual interactions.

Furthermore, we study the segregation dynamics in a repulsively interacting binary mixture of microswimmers with a triangular-like motility field using computer simulations and experiments. We observe segregation of microswimmers near the intensity minima while one species is localized close to the minimum (*bottom*) and the other one is centered around in an outer shell (*top*). Through attributing an effective *heaviness* to microswimmers, we define a *colloidal Brazil nut effect* in analogy to shaken granular matter in gravity. The demixing of the binary mixture exhibits a Brazil nut effect when the particles of the *heavier* species are floating on the *lighter* ones.



# Affidavit

I declare under oath that I have produced my thesis independently and without any undue assistance by third parties under consideration of the “Principles for the Safeguarding of Good Scientific Practice at Heinrich Heine University Düsseldorf”

Düsseldorf, \_\_\_\_\_



# Preface

The content of this dissertation is based on the subsequent publications, submitted paper, and planned but still ongoing research project:

I. Christian Scholz, Soudeh Jahanshahi, Anton Ldov, and Hartmut Löwen, *Inertial delay of self-propelled particles*, Nature Communications **9**, 5156 (2018).  
This publication is presented in chapter 2.

II. Soudeh Jahanshahi, Celia Lozano, Borge ten Hagen, Clemens Bechinger, and Hartmut Löwen, *Colloidal Brazil nut effect in microswimmer mixtures induced by motility contrast*, The Journal of Chemical Physics **150**, 114902 (2019).  
Note: This article is part of the Special Topic “Chemical Physics of Active Matter” in J. Chem. Phys.  
This paper was selected as Featured and is presented in chapter 5.

III. Soudeh Jahanshahi, Celia Lozano, Benno Liebchen, Hartmut Löwen, and Clemens Bechinger, *Realization of a motility-trap for active particles*, submitted to Science Advances.  
The basic model of this submitted paper is presented in chapter 4.

IV. Soudeh Jahanshahi, and Hartmut Löwen et al., *Normal and anomalous diffusion in active Langevin motion*, (in progress).  
This research project is presented in chapter 3.

My contributions to these scientific projects are specified in their corresponding chapters.



# Acknowledgments

I would like to express my deepest appreciation to all those who provided me the possibility to complete this project. Especially, I would like to express my gratitude to my supervisor Prof. Dr. Hartmut Löwen, who continuously and convincingly takes a spirit of adventure in regard to research. Without his guidance and persistent help, this thesis would not have been possible. I cannot say thank you enough for his tremendous support and help.

My heartfelt thanks also go to Prof. Dr. Clemens Bechinger, Prof. Dr. Benno Liebchen, Dr. Celia Lozano, Dr. Christian Scholz, Dr. Borge ten Hagen and Anton Ldov, with whom I had the incredible privilege to co-author papers: working alongside anyone of these people extended my insight into science in general and into physics in specific. Especially, I would here like to thank Dr. Celia Lozano for valuable discussions and advice, and for her great spirit.

None of my studies and learning would have been possible without all the people working at “Heinrich-Heine-Universität Düsseldorf”, in particular at our institute. Specifically, I thank Claudia Stader, who has facilitated my work in our group immensely. I also thank Joachim Wenk the system administrator of the “Institut für Theoretische Physik II: Weiche Materie”.

My special thanks go to my fellow doctoral candidates with whom I shared a very significant time, in particular Christian Hoell, Mate Puljiz and Sonja Tarama. I am also grateful for constant support and help of the members of the “Institut für Theoretische Physik II: Weiche Materie”. I hereby would like to thank Priv.-Doz. Dr. Alexei Ivlev for accepting to advise and review my thesis.

Moreover, I am deeply grateful to my parents and my sisters for always being there for me, for cheering me up when things did not work out the way I wanted, and also for sharing many unforgettable happy moments. Last but not least, I am very happy and incredibly thankful to have my husband Soroosh Alighanbari by my side. His belief in me and his continuous support have always encouraged me and have been an important milestone for my personal development and development of my career.



# Contents

<b>Abstract</b>	<b>i</b>
<b>Preface</b>	<b>v</b>
<b>1 Introduction</b>	<b>1</b>
1.1 The basic model . . . . .	2
1.2 Inertia-dominated active Brownian particles . . . . .	3
1.2.1 Circle flyer with time-independent self-propulsion, inertia, damping, and fluctuations . . . . .	3
1.2.2 Circle flyer with time-dependent self-propulsion, inertia, damping, and fluctuations . . . . .	8
1.3 Active Brownian particles in the overdamped limit . . . . .	12
1.3.1 Experiment . . . . .	13
1.3.2 Theory . . . . .	14
<b>2 Inertial delay of self-propelled particles</b>	<b>17</b>
<b>3 Normal and anomalous diffusion in active Langevin motion</b>	<b>33</b>
3.1 Introduction . . . . .	34
3.2 The basic model of active Langevin motion . . . . .	35
3.3 Time-independent self-propulsion, inertia, damping, and fluctuations . . . . .	38
3.3.1 Results for vanishing noise . . . . .	39
3.3.2 Effect of Brownian noise . . . . .	40
3.4 Time-dependent self-propulsion, inertia, damping, and fluctuations . . . . .	46
3.4.1 Adiabatic approximation for slow variations . . . . .	46
3.4.2 Non-adiabatic correction to the adiabatic approximation . . . . .	47
3.4.3 Fast variations . . . . .	48
3.5 Oscillating self-propulsion speed . . . . .	49
3.5.1 Results for vanishing noise . . . . .	49
3.5.2 Effect of Brownian noise . . . . .	50
3.6 Conclusion . . . . .	52
<b>4 Localization of a microswimmer in a triangular trap</b>	<b>55</b>
4.1 Introduction . . . . .	56
4.2 Theory . . . . .	56

<b>5 Colloidal Brazil nut effect in microswimmer mixtures induced by motility contrast</b>	<b>61</b>
<b>6 Concluding remarks</b>	<b>73</b>
<b>Bibliography</b>	<b>75</b>



# 1 Introduction

Converting energy stored in the environment into systematic movement is the defining characteristic of active matter systems [1]. The main characteristic features of living entities are likewise caused by a continuous injection of energy at the microscale [2]; hence, active systems provide a powerful platform to investigate the natural processes of life [3]. Through transduction of free energy into mechanical work, active agents drive themselves locally far from thermodynamic equilibrium [4], which makes them a useful framework in studying non-equilibrium statistical physics [5]. Their application delves though into various disciplines beyond physics; for instance, ecology for stochastic modeling of movement [6, 7], biomedical areas as drug carriers or sensors for biological targets [8, 9], robotics to develop systems that exhibit swarm intelligence [10], traffic flow [11] and environmental science [12].

Self-propelled particles were originally introduced to study the mass-migrating animal groups [13, 14, 15]. As a special class of self-propelled agents, active Brownian particles –unlike their passive counterparts whose equilibrium motion is driven just by thermal fluctuations due to erratic collisions with the surrounding medium [16]– propel themselves by a motility beyond random thermal fluctuations [17, 18]. The main applications of active Brownian particles –whether biological like bacteria [19, 20] or artificial such as Janus particles [21, 22, 23]– are centered around their functionalities in transport, sensing, and manipulation [24].

Here we study the behavior of active Brownian particles both as a single agent and when in interaction with other particles both analytically and using computer simulations. We assume the active agents to be spherical particles whose translational and rotational motions are confined to a two-dimensional plane. The self-propulsion is modeled through a coarse-grained approach by an effective force and torque fixed in the particle’s body frame [25].

Moving on a surface brings about hydrodynamic couplings between the self-propelled particles and the substrate [26, 27, 28]. The consequence of these couplings is that the particle orientation is always almost parallel to the nearby surface [29, 30]. For dry active matter systems, including vibrated granular particles on a plate [31, 5, 32], for highly crowded environments when no global flow is built up [33, 24], and for half-coated Janus colloids with a weakly nonuniform surface mobility at typical densities [34, 35], hydrodynamic interactions can be negligible. In this scientific research, apart from hydrodynamic fric-

tion, hydrodynamic interactions are disregarded. However, restriction of the rotational dynamics to two dimensions takes the hydrodynamic effects near a boundary into account. The validity of this model and our theoretical results are confirmed by real-space experiments.

## 1.1 The basic model

We use Langevin equation to investigate the stochastic dynamics of a subset of the degrees of freedom [36]. For a self-propelled particle confined in two spatial dimensions, the characteristic degrees of freedom are the center of mass position  $\mathbf{r}(t)$  and the rotational angle  $\varphi$ . The latter specifies the orientation of the particle  $\mathbf{n}(t) = (\cos \varphi(t), \sin \varphi(t))$ . Where no physical barriers or other particles are present, the equations of motion for a single particle with mass  $m$  and moment of inertia  $J$  are [37, 38]

$$m\ddot{\mathbf{r}}(t) + \xi\dot{\mathbf{r}}(t) = \xi v \mathbf{n}(t) + \xi \sqrt{2D} \mathbf{f}_{\text{st}}(t), \quad (1.1)$$

$$J\ddot{\varphi}(t) + \xi_r \dot{\varphi}(t) = \xi_r \omega + \xi_r \sqrt{2D_r} \tau_{\text{st}}(t). \quad (1.2)$$

The self-propulsion speed  $v$  corresponds to an effective force  $\mathbf{F} = \xi v \mathbf{n}(t)$ , which acts along the particle orientation  $\mathbf{n}(t)$ .  $\omega$  is the *circling frequency* corresponding to an effective torque  $\tau = \xi_r \omega$ . In order to restrict the rotational motion to two dimensions, the effective torque has to be perpendicular to the plane of motion. Within the picture of effective force and torque, we track the net motion of the particle and ignore completely the microscopic mechanism of movement.  $\xi$  and  $\xi_r$  denote the translational and rotational friction coefficients. The latter couples the circling frequency to the effective torque, while the former associates the propulsion speed to the effective force. The translational and rotational Brownian motions are modeled by independent zero-mean Markovian white noise processes  $\mathbf{f}_{\text{st}}(t)$  and  $\tau_{\text{st}}(t)$  with unitary variance, such that [24]

$$\langle \mathbf{f}_{\text{st}}(t) \otimes \mathbf{f}_{\text{st}}(t') \rangle = \delta(t - t') \mathbb{1}, \quad (1.3)$$

$$\langle \tau_{\text{st}}(t) \tau_{\text{st}}(t') \rangle = \delta(t - t'). \quad (1.4)$$

Here the brackets  $\langle \cdot \rangle$  indicate noise average and  $\mathbb{1}$  is the unit matrix. Thermal fluctuations are quantified by the short-time translational and rotational diffusion coefficients  $D$  and  $D_r$ . For a spherical particle with diameter  $\sigma$  in bulk situation, the diffusion coefficients fulfill  $D/D_r = \sigma^2/3$ . This ratio could change for particles moving near walls or system boundaries [39, 23].

## 1.2 Inertia-dominated active Brownian particles

The class of inertia-dominated active Brownian particles includes macroscopic self-propelled particles with non-negligible inertial effects and micron-sized active particles *flying* in a gaseous medium, where friction becomes such small that the inertial effects get dominant. The motion is affected by the random kicks of the surrounding medium. Therefore, the dynamics is coined as *active Langevin motion* and these inertia-dominated active Brownian particles are referred to as *microflyers* [40].

A particular example is dusty plasma, also called complex plasma, which is composed of mesoscopic dust particles in a weakly ionized gas [41, 42, 43, 44, 45]. Dusty plasmas are ubiquitous in space; for instance, they are found in planetary rings, cometary tails, interplanetary and interstellar clouds, the mesosphere and thunderclouds [46].

Other examples include vibration-driven granular particles [47, 48, 49, 50, 51, 52, 53, 54, 55], which get propelled through converting vibrational energy of the vibrating baseplate into directed motion, and mini-robots [56, 57], which are driven by an internal motor. Further examples are autorotating seeds and fruits [58, 59], which are equipped with appendages that act as wing and enable them to fly. Furthermore, the dynamics of animals [60, 61, 62] and insects [63, 64, 65, 66] can be analyzed within active Langevin motion, because of a two-fold reason: first, they are self-propelled with dominant inertial effects; second, the impact of environmental noise in their motion can be modeled by Brownian noise.

The model of active Langevin motion successfully describes active systems with nonvanishing inertial effects. However, the theoretical results are usually provided in the overdamped limit of rotational motion, i.e., case of negligible moment of inertia [67, 68, 69, 70, 38, 71]. In practice, neglecting the impact of the moment of inertia in dynamics is solely a good approximation for microflyers with fast rotational relaxation [72]. We have theoretically and experimentally demonstrated in the publication presented in chapter 2 that generically the dynamics of inertia-dominated Brownian particle is explicitly affected by the moment of inertia. Then, we have studied, as addressed in chapter 3, how the dynamics of the microflyer can be changed by taking temporally varying parameters into account.

### 1.2.1 Circle flyer with time-independent self-propulsion, inertia, damping, and fluctuations

When a microflyer undergoes chiral motion through the impact of an effective torque, we call it *circle flyer*. The chiral motion may, for instance, arise from

shape anisotropy [73, 74] or from particle imperfections [75] or from external fields [76, 77, 78]. Here we study the dynamics of a circle flyer with time-independent parameters. The translational and rotational motions are restricted to a two-dimensional plane. This restriction on rotational motion dictates that the effective torque is perpendicular to the plane of motion. The subsequent discussions are addressed in the publication presented in chapter 2, where we have performed real-space experiments and through which we have confirmed the theoretical predictions.

### 1.2.1.1 Experiment

Our experimental microflyers are minimalistic robots called vibrobots, which convert vibrational energy into directed motion using their tilted elastic legs [50]. Our vibrobots are made from a proprietary methacrylate-based photopolymer using a 3D printer at a precision of 0.05 mm. A new microflyer with new parameter combinations and consequently new dynamics can be created by varying the leg inclination, mass or moment of inertia of the vibrobot.

A single vibrobot of radius about 10 mm is placed on a circular acrylic baseplate with diameter of 300 mm and thickness of 15 mm. An electromagnetic shaker (Tira TV 51140) is attached to and shakes the baseplate. Due to the vibrations of the baseplate, the vibrobot skips by repeated collisions of its tilted elastic legs on the vibrating surface. Motion is confined to the two dimensional circular baseplate by an enclosing barrier [32]. To ensure that the vibrobot does a stable quasi-two-dimensional motion, the frequency and amplitude of excitations are fixed to  $f = 80$  Hz and  $A = 66$   $\mu$ m, respectively.

Brownian motion originates from microscopic surface inhomogeneities and in case of sufficiently strong driving, also from a bouncing ball instability [79], that gives rise to asynchronous jumps of the particle's legs and so to a tiny but very irregular precession, which in turn leads to random reorientations of the vibrobot. The propulsion speed depends on the frequency and the amplitude of the excitations, and on leg inclination. Since the elasticity and friction coefficients depend on material properties, the propulsion speed depends on material properties too [50, 79, 80, 81]. Owing to the strong non-equilibrium nature of the system, the Stokes-Einstein relation does not hold, i.e., the diffusion and friction coefficients are not related though  $D = k_B T / \xi$ , where  $k_B T$  is the effective thermal energy. [82].

Any object with inertia carries out ballistic motion, even if only on minuscule time and length scales. For instance, ballistic motion of colloids, whose inertial effects are overwhelmed by viscous friction, takes place on length scales smaller than 1 Å for approximately 100 ns. The reason is that, ballistic motion happens when dynamics is dominated by the inertia. Observation of such *short* ballistic motion requires high accuracy measurements and has been performed only for

passive colloids [83, 84, 85]. Inertia-dominated active Brownian particles, on the other hand, perform ballistic motion on larger time scales. For example, the ballistic regime of our vibrobots lasts between 0.1 s to around 1 s. As a consequence, we observe a clear transition from purely ballistic motion to normal diffusion in our experiments for mean-square displacement.

### 1.2.1.2 Theory

The profound influence of inertia on dynamics is portrayed by *inertial delay*, i.e. a time delay between the orientation variations and the subsequent changes in the velocity direction. In case of vanishing inertial effects, velocity direction pursues the orientation instantaneously, and the inertial delay is zero.

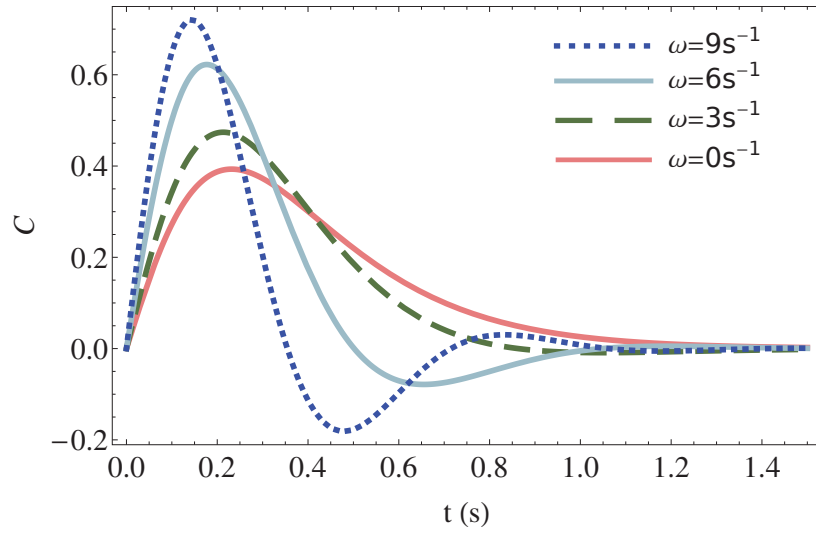


**Figure 1.1:** Time-dependence of the inertial delay  $C(\dot{\mathbf{r}}(t), \mathbf{n}(t))$  for different circling frequencies (see legend). The other parameters are as follows:  $\gamma = 8 \text{ s}^{-1}$ ,  $\gamma_r = 7 \text{ s}^{-1}$ ,  $D = 8 \times 10^{-5} \text{ m}^2 \text{ s}^{-1}$ , and  $D_r = 5 \text{ s}^{-1}$ .

The retarded response of the velocity to the orientation variations can be quantified via the correlations between the velocity and the orientation. The inertial delay is hence defined as the average difference between the projection of the orientation at time  $t_0$  on the velocity at some later time  $t + t_0$  and projection of the velocity at time  $t_0$  on the orientation at some later time  $t + t_0$ , i.e.

$$C(\dot{\mathbf{r}}(t), \mathbf{n}(t)) = \frac{\langle \dot{\mathbf{r}}(t) \cdot \mathbf{n}(0) - \dot{\mathbf{r}}(0) \cdot \mathbf{n}(t) \rangle_T}{v}. \quad (1.5)$$

The inertial delay is made dimensionless by scaling with the propulsion speed. Here the brackets  $\langle \cdot \rangle_T$  indicate time average through which the impact of  $t_0$  is averaged out, more specifically the impact of the initial configuration is averaged out.

The effects of initial configurations can be canceled out also by an ensemble average over all possible initial configurations. An ensemble average is generally associated with a density function. The required density function can be provided by taking into account a *steady-state initial condition*, i.e. first, the system is let to reach the steady-state, then the measurement begins. Consequently, the average over all possible initial configurations becomes the steady-state average. For example, the averaged initial angular and translational velocities are

$$\int d\dot{\phi}_0 P(\dot{\phi}_0) \dot{\phi}_0 = \lim_{t_0 \rightarrow \infty} \langle \dot{\phi}(t_0) \rangle = \omega, \quad (1.6)$$

$$\int d\dot{\mathbf{r}}_0 P(\dot{\mathbf{r}}_0) \dot{\mathbf{r}}_0 = \lim_{t_0 \rightarrow \infty} \langle \dot{\mathbf{r}}(t_0) \rangle = 0, \quad (1.7)$$

respectively. Here  $P(\dot{\phi}_0)$  and  $P(\dot{\mathbf{r}}_0)$  indicate the steady-state distributions of the respective angular and translational velocities. Specifically, due to the steady-state initial condition, the average over all possible initial states of a quantity is evaluated as an ensemble average over that quantity according to its steady-state distribution.

Based on the ergodic hypothesis [86, 87, 88], the former, time average, is equivalent to the latter, steady-state average,

$$\langle x(t) \rangle_T = \lim_{t_0 \rightarrow \infty} \langle x(t + t_0) \rangle, \quad (1.8)$$

where  $x$  represents an arbitrary quantity. While noise average contains the information of the initial configuration, this information is lost in time average. In other words, a system that evolves for a long time (like in steady-state), *forgets* its initial state.

Different time-scales which characterize the motion of the circle flyer are as follows: the translational and rotational damping times  $\gamma^{-1} = m/\xi$  and  $\gamma_r^{-1} = J/\xi_r$ , the persistence time  $D_r^{-1}$ , the translational and rotational crossover times  $2D/v^2$  and  $2D_r/\omega^2$ , and the reorientation time  $\omega^{-1}$ .

As visualized in Fig. 1.1, the inertial delay starts from zero at time equal to zero and grows until reaches its maximum. Then it decays and re-approaches zero for times much larger than the damping times. In case of nonvanishing circling frequency, the inertial delay may undergo damped oscillations between positive and negative values during the decaying stage (see Fig. 1.1). Moments with negative inertial delay stem from the fact that the orientation may get lag behind the velocity direction because of rapid circling. Thermal fluctuations accelerate the decay rate such that in case of smaller random noise, the velocity and the orientation remain correlated for a longer time.

In case of vanishing random noise, the circle flyer performs circular motion after some transient initial revolutions. The transient initial regime is attributed to the inertial effects, i.e. the higher the moment of inertia, the more difficult

the change in the angular velocity. Because of this higher resistance towards any change in the angular velocity, it takes longer for a circle flyer with larger moment of inertia to arrive its final circular flying path. The radius of the final circular flying path

$$r = \frac{v}{\omega} \sqrt{\frac{\gamma^2}{\gamma^2 + \omega^2}}, \quad (1.9)$$

does not depend on the moment of inertia, however, the center of the circular flying path is an increasing function of the moment of inertia. This demonstrates that during the transient initial regime, the *stretched* particle with higher moment of inertia flies away farther than the *shrunk* one with smaller moment of inertia. When inertia vanishes, the radius of the final flying path reduces to the one for a noise-free overdamped circle flyer, referred to as circle swimmer, namely if  $\gamma \rightarrow \infty$ , Eq. (1.9) approaches the radius of the swimming path of a noise-free circle swimmer, i.e.  $r = v_0/\omega$  [89].

In the presence of thermal noise, the distribution of the angular velocity for times much larger than the rotational damping time reaches its stationary state around the circling frequency with width  $\sqrt{2D_r\gamma_r}$ , while the distribution of the rotational angle keeps spreading over the angle domain as time passes. The correlation function of the angular velocity mimics the correlations of a colored noise. Therefore, due to the angular velocity, the dynamics of the rotational angle is subject to an exponentially correlated Gaussian colored noise [90, 91]. The time-scale of the correlations in the orientation is the persistence time which reflects the fact that the fluctuating torque decorrelates the orientation. The additional short-time correlations in the orientation is due to the colored noise imposed by the angular velocity.

The translational velocity correlation function results in the mean-square displacement through [92]

$$\langle (\mathbf{r}(t) - \mathbf{r}_0)^2 \rangle = 2 \int_0^t ds (t-s) \langle \dot{\mathbf{r}}(s) \cdot \dot{\mathbf{r}}(0) \rangle_T. \quad (1.10)$$

In the short-time limit, the dynamics of the circle flyer is still in the ballistic regime such that

$$\langle (\mathbf{r}(t) - \mathbf{r}_0)^2 \rangle = \langle \dot{\mathbf{r}}^2 \rangle t^2, \quad (1.11)$$

while the second moment of the translational velocity  $\langle \dot{\mathbf{r}}^2 \rangle = \langle \dot{\mathbf{r}}(0) \cdot \dot{\mathbf{r}}(0) \rangle_T$  is comprised of the thermal energy and the injected kinetic energy. In the long-time limit, the circle flyer undergoes diffusive motion, i.e.  $\langle (\mathbf{r}(t) - \mathbf{r}_0)^2 \rangle = 4D_L t$  with long-time diffusion coefficient

$$D_L = D + \frac{v^2}{2\gamma_r} \operatorname{Re} \left[ e^{D_r/\gamma_r} \left( \frac{D_r}{\gamma_r} \right)^{-\left( \frac{D_r - i\omega}{\gamma_r} \right)} \gamma \left( \frac{D_r - i\omega}{\gamma_r}, \frac{D_r}{\gamma_r} \right) \right]. \quad (1.12)$$



Here

$$\gamma(a, x) = \int_0^x t^{a-1} e^{-t} dt, \quad (1.13)$$

is the lower incomplete gamma function [93]. The first term in Eq. (1.12) is related to the equilibrium diffusive behavior of a passive particle when  $v = 0$ . In the limit of vanishing inertia, the long-time diffusion coefficient goes to that for overdamped microflyers (microswimmers), i.e.  $D_L = D + v_0^2 D_r^{-1}/2$  when  $\omega = 0$  [94]. The long-term diffusive dynamics does not explicitly depend on the mass, but it depends on the mass distribution around the axis of rotation, namely on the moment of inertia. There is no dependence on the translational friction coefficient in the long-time dynamics.

When the moment of inertia shrinks to small values, the asymptotic long-time diffusion coefficient of the circle flyer grows proportional to the moment of inertia such that

$$D_L = D + \frac{v^2}{2} \frac{D_r}{D_r^2 + \omega^2} + \frac{v^2}{2\xi_r} \frac{D_r^2}{D_r^2 + \omega^2} J + \mathcal{O}(J^2). \quad (1.14)$$

The terms independent of moment of inertia in Eq. (1.14) characterize the long-time diffusion coefficient for circle swimmers [95].

On the other hand, as the moment of inertia grows to large values, the long-time diffusion coefficient of the circle flyer asymptotically vanishes to zero. This stems from the fact that circling diffusion becomes more difficult by increasing the moment of inertia due to getting trapped in circular *cages* of the trajectory. However, in case of vanishing circling frequency, the asymptotic behavior of the long-time diffusion coefficient for large moments of inertia grows proportional to the square root of the moment of inertia

$$D_L = D + v^2 \sqrt{\frac{\pi}{8D_r\xi_r}} \sqrt{J} + \mathcal{O}(\sqrt{J}^{-1}). \quad (1.15)$$

The reason behind this different behavior in case of vanishing circling frequency is that a very large moment of inertia brings about huge resistance to changing the angular velocity. This causes the impact of fluctuating torque fades away by the large moment of inertia and the microflyer diffusively moves with the optimum speed along the preferred direction.

### 1.2.2 Circle flyer with time-dependent self-propulsion, inertia, damping, and fluctuations

When animals move while swimming, flying, walking or running, the maneuverability of motion is provided by changes in the body shape [96, 97]. As



a consequence, the moment of inertia changes constantly and becomes time-dependent. Along with propulsion speed, this can result in temporally-varying rotational parameters such as friction coefficient [98, 99]. The randomness in motion, caused by environmental stimuli, can also be included through Brownian noise.

Variable-mass systems, whose mass changes with time, comprise an important class in transportation technology. Examples include rockets, which are propelled by continuously losing mass, and robots with discrete mass variation through picking up or releasing objects [100]. Time-dependent mass can bring about time-dependent friction coefficient [101]. Variable-mass systems can be also affected by noise, e.g. because of thermal fluctuations in microscopic scales. Therefore, active Langevin motion provides an efficient model to study such systems with temporally varying mass.

When inertia is time-dependent, the coupled Langevin equations in Eqs. (1.1) and (1.2) must now include the terms proportional to the temporal change of inertia. This results in the following coupled equations of motion

$$m(t)\ddot{\mathbf{r}}(t) + (\xi(t) + \dot{m}_{en})\dot{\mathbf{r}}(t) = \xi(t)v(t)\mathbf{n}(t) + \xi(t)\sqrt{2D(t)}\mathbf{f}_{st}(t) \quad (1.16)$$

$$J(t)\ddot{\varphi}(t) + (\xi_r(t) + \dot{J})\dot{\varphi}(t) = \xi_r(t)\omega(t) + \xi_r(t)\sqrt{2D_r(t)}\tau_{st}(t), \quad (1.17)$$

in which self-propulsion, damping, and thermal fluctuations are considered to be time-dependent, too. Here  $\dot{m}_{en}$  denotes the isotropic change in mass due to the interaction with the environment and can be positive or negative. Also, we have to take in mind that in case of rockets, the propulsion force depends on the rate of change in mass due to eject the exhaust fluid, i.e. on  $\dot{m}_p$ , which is negative. Therefore,  $\xi(t)v\mathbf{n}(t) = \dot{m}_p\mathbf{u}$ , where  $\mathbf{u} = -v\mathbf{n}(t)$  is the velocity of exhaust relative to the rocket.

While for *normal* diffusion, the mean-square displacement is proportional to  $t$ , in case of *anomalous* diffusion, this proportionality becomes  $t^\alpha$ , where the anomalous exponent  $\alpha$  is a real positive number and  $\alpha \neq 1$  [102, 103, 104, 105, 106, 107, 108, 109]. When  $\alpha < 1$  subdiffusive behavior emerges, while for  $\alpha > 1$  the circle flyer superdiffuses. We have demonstrated that temporal variations of parameters can give rise to anomalous diffusion. This results in the transport process of the diffusion to be adjustable through choosing the temporal behavior of parameters [110]. The subsequent discussions are regarding chapter 3.

### 1.2.2.1 Oscillating self-propulsion speed

In case of oscillating self-propulsion

$$v(t) = v_0 \left( 1 + \chi \sin(\nu t + \theta_0) \right), \quad (1.18)$$

while inertia, damping, fluctuations, and circling frequency are time-independent, the inertial delay is the same as that for a circle flyer with constant self-propulsion speed. The reason stems from the sinusoidal nature of time-dependence, where the oscillations cancel out the impact of each other over the course of each propulsion period, hence only the term corresponding to the constant propulsion, i.e.  $v_0$ , contributes to the inertial delay. In Eq. (1.18),  $\nu$  and  $v_0\chi$  denote the frequency and the amplitude of the self-propulsion, respectively, where  $\chi \leq 1$ , and  $\theta_0$  is the initial phase of the oscillation. The here presented results are for the situation when the ratio of the frequencies  $\omega$  and  $\nu$  is rational and for non-vanishing circling frequency.

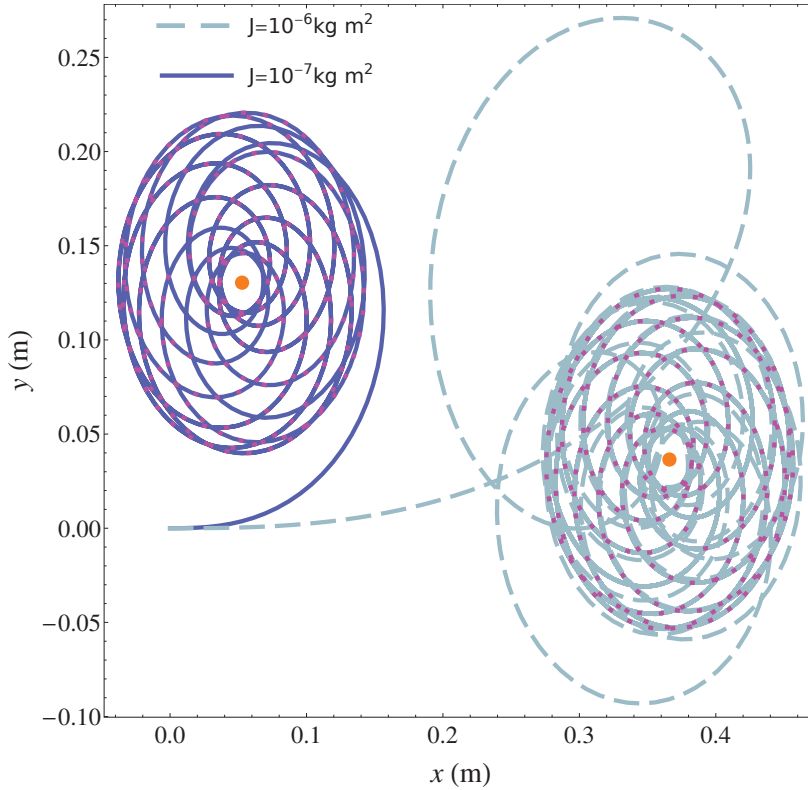


**Figure 1.2:** Noise-free trajectories for two different moments of inertia (see legend). The circle flyer starts its motion from the origin along  $x$  direction with zero initial velocity and vanishing initial angular velocity. The flying paths after relaxation of the initial conditions are visualized by dotted magenta curves. The centers of the flying paths are shown by orange circles. The other parameters are as follows:  $\xi_r = 7 \times 10^{-8} \text{ kg m}^2 \text{ s}^{-1}$ ,  $\gamma = 8 \text{ s}^{-1}$ ,  $v_0 = 0.07 \text{ m s}^{-1}$ ,  $\chi = 0.5$ ,  $\omega = 1.3 \text{ s}^{-1}$ ,  $\nu = 0.7 \text{ s}^{-1}$ , and  $\theta_0 = 0$ .

The translational dynamics of the circle flyer with oscillating propulsion speed demonstrates an interplay between different frequencies, i.e. circling frequency  $\omega$ , sum frequency  $\omega + \nu$ , and difference frequency  $\omega - \nu$ . Specifically, the contri-

bution of the terms, which contain circling frequency in sec. 1.2.1, expands now to three different terms regarding the circling frequency, the sum frequency, and the difference frequency.

In case of vanishing noise, after the relaxation of the initial regime which includes some transient revolutions and takes longer for a higher moment of inertia, the circle flyer reaches its final periodic flying path. This feature is visualized in Fig. 1.2 for a circle flyer when it is stretched and when it is shrunk. The period of the final trajectory is  $T = 2\pi \text{LCM}(\omega^{-1}, (\omega + \nu)^{-1}, |\omega - \nu|^{-1})$ . Here LCM denotes the lowest common multiple. In special case when  $\omega = \nu$ , the period of the trajectory is simply  $T = 2\pi/\omega$ . The final flying path does not depend on the moment of inertia, however, its center (shown by orange circles in Fig. 1.2) is an increasing function of moment of inertia. In the overdamped limit, a noise-free circle swimmer with oscillating self-propulsion is also confined to a periodic swimming path as reported in Refs. [111, 112].

In the presence of thermal noise, as the moment of inertia grows to very large values, the long-time diffusion coefficient goes asymptotically to zero. This happens because the growth of the moment of inertia increases the resistance to circling motion and this results in vanishing circling diffusion.

However, when  $\omega = \nu$ , the long-time diffusion coefficient asymptotically grows proportional to  $\sqrt{J}$  by increasing the moment of inertia to very large values. This comes from the contribution of the difference frequency  $(\omega - \nu)$  in the long-time dynamics and corresponds to a resonance situation when the particle flies with the optimum speed along the preferred direction.

### 1.2.2.2 Adiabatic approximation for slow variations

The appearance of the anomalous diffusion in a system is usually attributed to power law variations in the system's parameters [109]. A slow power law in time for the moment of inertia, self-propulsion, rotational friction, and diffusion coefficients

$$J(t) = j_0 t^\alpha, \quad V_p(t) = v_0 t^\beta, \quad \xi_r(t) = \xi_{r0} t^\delta, \quad D_r(t) = D_{r0} t^\varepsilon, \quad (1.19)$$

can cause the emergence of anomalous diffusion in long-time dynamics of the microflyer.  $j_0, v_0, \xi_{r0}$  and  $D_{r0}$  are constant values, and  $\alpha, \beta, \delta$  and  $\varepsilon$  are exponents whose combination shapes the anomalous exponent.

In case of vanishing circling frequency and large  $j_0$ , within adiabatic approximation, the long-time mean-square displacement is proportional to

$$\langle (\mathbf{r}(t) - \mathbf{r}_0)^2 \rangle \sim v_0^2 \sqrt{\frac{j_0}{D_{r0} \xi_{r0}}} t^{1+2\beta+(\alpha-\delta-\varepsilon)/2}. \quad (1.20)$$

When

$$2\beta + (\alpha - \delta - \varepsilon)/2 > 0, \quad (1.21)$$

Eq. (1.20) manifestly demonstrates superdiffusive behavior in the long-time dynamics for large moments of inertia. In case of

$$2\beta + (\alpha - \delta - \varepsilon)/2 < 0, \quad (1.22)$$

random forces overwhelm the subdiffusive behavior of Eq. (1.20) and as a result, normal diffusion emerges in the long-time dynamics. In the limit  $j_0 \rightarrow 0$ , the mean-square displacement goes to that of a microswimmer with power law time-dependent self-propulsion, which is reported in Ref. [111]. The first order non-adiabatic correction to the adiabatic approximation of the mean-square displacement demonstrates a ballistic phase in the long-time dynamics.

Since there is no explicit dependence on mass or translational friction coefficient in the long-time diffusion coefficient, temporal behavior of  $m(t)$  or  $\xi(t)$  can not indeed alter the long-time dynamics. For noise-free cases, which is relevant to the macroscopic variable-mass systems such as rockets, a time-dependent mass can, for instance, change the final flying path, on which circle flyer arrives after relaxation of the initial regime.

### 1.2.2.3 Fast variations

In case of rapidly varying parameters, the system is able to dynamically respond just to the mean variations. For example, a rapidly oscillating moment of inertia

$$J(t) = j_0(1 + \sin(\nu_j t)), \quad (1.23)$$

with a very large oscillation frequency  $\nu_j$ , when  $\omega = 0$  and  $j_0 \rightarrow \infty$ , gives rise to the long-time dynamics

$$\langle (\mathbf{r}(t) - \mathbf{r}_0)^2 \rangle \sim 4Dt + 2v^2 \sqrt{\frac{\pi j_0}{2D_r \xi_r}} t, \quad (1.24)$$

which is the same as the long-time behavior of a microflyer with a large constant moment of inertia, here  $j_0$ , given by Eq. (1.15).

## 1.3 Active Brownian particles in the overdamped limit

For microscopic particles *swimming* in a Newtonian liquid, viscous effects are dominant and inertial effects are negligible. Such agents are called active Brownian particles, also referred to as microswimmers and their describing model is called *active Brownian motion*, wherein the overdamped dynamics is modeled through Gaussian white noise as solvent kicks, and an effective self-propulsion

force [95, 113, 23, 114]. This is referred to as *low Reynolds number* regime since Reynolds number quantifies the strength of inertial effects relative to viscous forces in the system [115]. In this case, the coupled Langevin equations, given by Eqs. (1.1) and (1.2), are presented in the overdamped limit where inertia is negligible

$$\dot{\mathbf{r}}(t) = v\mathbf{n}(t) + \sqrt{2D}\mathbf{f}_{\text{st}}(t), \quad (1.25)$$

$$\dot{\varphi}(t) = \omega + \sqrt{2D_r}\tau_{\text{st}}(t). \quad (1.26)$$

Typical microswimmers are micron-sized biological or artificial objects swimming in a viscous fluid medium, e.g., water. Examples of biological microswimmers include spermatozoa [116, 117, 118], and bacteria species, such as *E. coli* [119, 120], and *vibrio cholera* [20]. One famous example of man-made microswimmers is Janus particle; it is named after the two-faced Roman deity because its surface has two or more distinct physical properties [94, 121, 122, 123, 124, 125]. When a microswimmer performs chiral motion because of the impact of an effective torque, it is named circle swimmer [126, 127]. In nature, certain bacteria [128, 129, 19, 130] and spermatozoa [116, 117, 131] exhibit circling swimming on a planar substrate.

Using experiments, simulations and analytical theory, we have studied the dynamics of a single Janus particle as well as collective effects of many such microswimmers, whose motility, i.e. individual swimming speed of a single particle, is tunable by light [132, 133, 134, 135, 136]. The subsequent discussion is regarding chapter 4 and the publication presented in and chapter 5.

### 1.3.1 Experiment

Artificial microswimmers are Janus particles made of silica spheres, with diameter of a few micrometers, which are half-coated with a nanometer carbon layer. The microswimmers are suspended in a critical mixture of water and 2,6-lutidine. The whole sample is homogeneously illuminated with laser light at  $\lambda = 532 \text{ nm}$ , which is mainly absorbed at capped hemisphere. This results in a temperature gradient across the microswimmer. When the cap temperature locally exceeds the critical temperature of the solvent  $T_c = 34.1^\circ\text{C}$ , the solvent locally demixes, and the Janus particle exhibits self-propulsion. The resultant swimming speed depends linearly on the incident laser intensity [132]. Below and above a threshold intensity  $I_r$ , microswimmers propel with the carbon cap at the rear and at the front, respectively [133].

Demixing of solvent near the cap results in the appearance of a droplet nucleating around the microswimmer [137]. In the presence of intensity gradients, the cap becomes inhomogeneously heated leading to the nucleation of asymmetric

droplets [137, 132]. This brings about an active torque aligning the particle's cap towards the intensity gradient. Consequently, negative and positive phototactic behaviors happen for  $I < I_r$  and  $I > I_r$ , respectively [133, 136]. When intensity is lower than the threshold intensity, the particle is directed towards the regions with lower intensity (i.e. negative phototaxis). Whereas for  $I > I_r$ , the orientation of the particle is aligned towards increasing light intensity (i.e. positive phototaxis).

Creation of periodic triangular intensity pattern is achieved by a laser line focus being scanned across the sample plane with a frequency of 200 Hz. Synchronization of the scanning motion with the input voltage of an electro-optical modulator leads to a quasi-static illumination landscape [132, 136]. Due to the large thermal diffusivity of the carbon cap, the temperature field around the particle responds to illumination intensity variations on time scales below  $10^{-5}$ s. This gives rise to an almost immediate response of the particle motility to the light intensity changes [133, 136].

Active colloidal mixtures with different size ratios are prepared by doping active suspension of small particles with a few large active colloids. Since the propulsion speed depends linearly on the absorbed intensity across the particle's cap, the speed can be varied in a linear pattern by changing the thickness of the cap's carbon layer [133].

### 1.3.2 Theory

The microswimmer is confined to a two-dimensional substrate in a static periodic triangular-like light intensity field. Since the motility of the particles is proportional to the imposed light intensity, the triangular-like intensity field leads to a triangular motility profile for the microswimmer. The self-propulsion is periodic in the  $x$ -coordinate with a characteristic length  $l_v$ , and depends on the particle's position along the  $x$ -direction, but it is independent of the  $y$ -coordinate. In one spatial period, in case of negative phototaxis, the motility profile is defined as

$$v(x) = 2\frac{\Delta v}{l_v}|x| + V^{\min} \quad \text{for } |x| \leq l_v/2, \quad (1.27)$$

while for positive phototaxis, it is specified by

$$v(x) = -2\frac{\Delta v}{l_v}|x| + V^{\max} \quad \text{for } |x| \leq l_v/2, \quad (1.28)$$

with  $\Delta v = V^{\max} - V^{\min}$ . The propulsion velocity spatially varies between the maximum value  $V^{\max}$  and the minimum value  $V^{\min}$ .

The aligning active torque generates the angular velocity

$$\omega(\varphi, x) = \frac{c}{\sigma} v_p(x) v'_p(x) \sin \varphi, \quad (1.29)$$

which depends on the  $x$ -coordinate through the propulsion speed. Here,  $v'(x) = \frac{dv(x)}{dx}$  denotes the velocity gradient. The magnitude of the aligning torque is inversely tuned by the particle diameter  $\sigma$ . The constant  $c$  follows from experiments while its sign depends on whether the particle moves with the cap in the rear or in the front:  $c < 0$  corresponds to the positive phototaxis case and  $c > 0$  is for the negative phototaxis situation [138, 132, 133, 136].

The axial symmetry of the velocity field around the particle breaks due to the light intensity gradient leading to the alignment of the orientation towards the direction of the negative or positive intensity gradient [132, 133]. Consequently, the aligning torque is perpendicular to both orientation and intensity gradient, which induces dependence on  $\sin \varphi$  in Eq. (1.29).

For positive phototaxis situation, the microswimmer becomes effectively localized near motility maximum [136]. In case of negative phototaxis, the microswimmer gets dynamically trapped in the dark spots where its motility is minimum [139, 140, 141].

When granular mixtures of variously sized particles are subjected to shaking or vibration, Brazil nut effect emerges where the largest particles rise to the top against the gravitational gradient; once at the top, they stay there (on the surface of the mixture) [142]. In analogy to shaken granular matter in gravity, we define a *colloidal Brazil nut effect* in a repulsively interacting binary mixture of small negative phototactic microswimmers doped with large ones, wherein particles interact via a short-ranged repulsive Weeks-Chandler-Andersen (WCA) pair potential [143].

In the binary mixture of microswimmers, we observe a segregation of active particles near the intensity minimum where one species is localized close to the minimum (*bottom*) and the other one is centered around in an outer shell (*top*). When the aligning torque is very strong, there is an exact mapping of the nonequilibrium system onto an equilibrium system in an effective external potential, which is similar to (height-dependent) gravity. Accordingly, we define effective *heaviness* of the particles. We call the situation with *heavier* microswimmers on *top* of the *lighter* ones *colloidal Brazil nut effect*. Apart from size (diameter) and maximum velocity  $V^{\max}$ , the small and large microswimmers of the binary mixture are exactly the same in different parameters. The results of real-space experiments confirm the theoretical predictions.





## 2 Inertial delay of self-propelled particles

Reproduced from

Christian Scholz, Soudeh Jahanshahi, Anton Ldov, and Hartmut Löwen

Nature Communications **9**, 5156 (2018)

published by *Nature Publishing Group / Springer Nature*

Digital Object Identifier (DOI): 10.1038/s41467-018-07596-x

Link to version of record:

<https://www.nature.com/articles/s41467-018-07596-x>

### **Statement of contribution**

H.L. has planned the project. C.S. designed the experimental setup. C.S. and A.L. carried out the experiments. C.S. and I and A.L. analyzed the measurements. I and C.S. wrote the simulation code. I and C.S. performed and analyzed the simulations. I developed the theoretical results. All authors discussed the results and wrote the manuscript.

### **Copyright and license notice**

©Nature Publishing Group / Springer Nature

The author of articles published by Springer Nature do not usually need to seek permission for re-use of their material as long as the journal is credited with initial publication.

Ownership of copyright in original research articles remains with the Author, and provided that, when reproducing the contribution or extracts from it or from the Supplementary Information, the Author acknowledges first and reference publication in the Journal, the Author retains the non-exclusive rights to reproduce the contribution in whole or in part in any printed volume (book or thesis) of which they are the author(s).

Nature Communications articles are published open access under a CC BY license (Creative Commons Attribution 4.0 International License), which permits use, sharing, adaptation, distribution and reproduction in any medium or format, as long as you give appropriate credit to the original author(s) and the source, provide a link to the Creative Commons license, and indicate if changes were made.



## ARTICLE

DOI: 10.1038/s41467-018-07596-x

OPEN

# Inertial delay of self-propelled particles

Christian Scholz<sup>1</sup>, Soudeh Jahanshahi<sup>1</sup>, Anton Ldov<sup>1</sup> & Hartmut Löwen<sup>1</sup>

The motion of self-propelled massive particles through a gaseous medium is dominated by inertial effects. Examples include vibrated granulates, activated complex plasmas and flying insects. However, inertia is usually neglected in standard models. Here, we experimentally demonstrate the significance of inertia on macroscopic self-propelled particles. We observe a distinct inertial delay between orientation and velocity of particles, originating from the finite relaxation times in the system. This effect is fully explained by an underdamped generalisation of the Langevin model of active Brownian motion. In stark contrast to passive systems, the inertial delay profoundly influences the long-time dynamics and enables new fundamental strategies for controlling self-propulsion in active matter.

<sup>1</sup>Institut für Theoretische Physik II: Weiche Materie, Heinrich-Heine-Universität Düsseldorf, 40225 Düsseldorf, Germany. Correspondence and requests for materials should be addressed to C.S. (email: christian.scholz@hhu.de) or to H.L. (email: hlowen@thphy.uni-duesseldorf.de)

Newton's first law states that because of inertia, a massive object resists any change of momentum. Before this groundbreaking idea, the dominant theory of motion was based on Aristotelian physics, which posits that objects come to rest unless propelled by a driving force. In retrospect, this perception is unsurprising, as the motions of everyday objects are influenced significantly by friction. In microscopic systems such as colloids, inertial forces are completely overwhelmed by viscous friction. In fact, in the absence of inertia, particles cannot move by reciprocal shape deformations due to kinematic reversibility. Biological organisms such as bacteria must therefore self-propel by implementing non-reciprocal motion<sup>1</sup>.

However, any finitely massive object performs ballistic motion, even if only on minuscule time and length scales. For example, colloidal particles undertake ballistic motion below 1 Å for approximately 100 ns. Experimental verification of this motion requires high accuracy measurements and has been achieved only for passive colloids<sup>2–4</sup>. In contrast, for macroscopic self-propelled particles, such as animals and robots, the magnitude of inertial forces can be comparable to that of the propulsion forces and influence the dynamics on large time scales.

A particularly simple example of a macroscopic self-propelled particle is a minimalistic robot called a vibrobot, which converts vibrational energy into directed motion using its tilted elastic legs<sup>5</sup>. Collectives of such particles exhibit novel non-equilibrium dynamics<sup>6–9</sup>, self-organisation<sup>10</sup>, clustering<sup>5,11</sup> and swarming<sup>12–15</sup>. Along with animals<sup>16</sup>, artificial and biological microswimmers<sup>17–19</sup>, vibrobots belong to the class of active soft matter.

Here, we demonstrate that the inertia of self-propelled particles causes a significant delay between their orientation and velocity and increases the long-time diffusion coefficient through persistent correlations in the underdamped rotational motion. Standard models, such as the Vicsek-model<sup>20</sup> and active Brownian motion<sup>21</sup> cannot explain this behaviour as they neglect inertia. Instead, the dynamics can be understood in terms of underdamped Langevin equations with a self-propulsion term that couples the rotational and translational degrees of freedom. Using the mean squared displacements (MSDs) and velocity distributions, fitted by numerical and analytical results, we extract a unique set of parameters for the model. We derive analytic solutions for the short- and long-time behaviour of the MSD and prove that the long-time diffusion coefficient explicitly depends on the moment of inertia.

## Results

**Experimental observation of inertial effects.** Our experimental particles are 3D-printed vibrobots driven by sinusoidal vibrations from an electromagnetic shaker. To investigate a wide range of parameter combinations, we varied the leg inclination, mass and moment of inertia of the particles (see Fig. 1a–d). The excitation frequency and amplitude were fixed to  $f = 80$  Hz and  $A = 66$  μm, respectively, which ensures stable quasi-two-dimensional motion of the particles.

The mechanism is illustrated in Fig. 1e and Supplementary Movie 1. The vibrobots move by a ratcheting mechanism driven by repeated collisions of their tilted elastic legs on the vibrating surface. Their propulsion velocity depends on the excitation frequency, amplitude, leg inclination and material properties such as the elasticity and friction coefficients<sup>5,22–24</sup>. Long-time random motions are induced by microscopic surface inhomogeneities and (under sufficiently strong driving) a bouncing ball instability<sup>24</sup>, that causes the particle's legs to jump asynchronously and perform a tiny but very irregular precession, which in turn leads to random reorientations of the particle. Thereby, the vibrobot motion is considered as a macroscopic realisation of active

Brownian motion<sup>12,13,25,26</sup>. Figure 1f shows three representative trajectories of particles with different average propulsion velocities (see also Supplementary Movie 2). The persistence length is noticeably shorter for slower particles than for faster particles, as generally expected for self-propelled particles<sup>19</sup>.

However, the significance of inertial forces is an important difference between motile granulates and microswimmers<sup>11,27</sup>. Massive particles do not move instantaneously, but accelerate from rest when the vibration is started. The time dependence of the initial velocity (averaged over up to 165 runs per particle) is shown in Fig. 2a. The particles noticeably accelerated up to the steady state on a time scale of  $10^{-1}$  s, one order of magnitude larger than the inverse excitation frequency and the relaxation time of the shaker. When perturbed by an external force, vibrationally driven particles approach their steady state on a similar time scale<sup>10</sup>. The relaxation process is well fitted by an exponential function, as expected for inertial relaxation. Inertia also influences the dynamical behaviour of the particles' orientation relative to their velocity. The orientation (red arrows in Fig. 2b) systematically deviates from the movement direction (black arrows in Fig. 2b). Particularly, during sharp turns the orientation deviates towards the centre of the curve, whereas the velocity is obviously tangential to the trajectory. We compare the angle of orientation  $\phi$  to the angle of velocity  $\Theta = \arctan 2(\dot{Y}, \dot{X})$  in Fig. 2b and find that  $\Theta$  systematically pursues  $\phi$  with an inertial delay of order  $10^{-1}$  s. A slow-motion recording of one particle in Supplementary Movie 3 illustrates the dynamic delay between motion and orientation. The particle quickly reorients, but its previous direction is retained by inertia. Consequently, the particle drifts around the corner, mimicking the well-known intentional oversteering of racing cars.

**Underdamped Langevin model.** Despite the complex non-linear dynamics of the vibrobots<sup>5,23,24,28,29</sup>, our observations can be fully described by a generalised active Brownian motion model with explicit inertial forces. The dynamics are characterised by the centre-of-mass position  $\mathbf{R}(t) = (X(t), Y(t))$  and the orientation  $\mathbf{n}(t) = (\cos\phi(t), \sin\phi(t))$ , where  $\phi(t)$  defines the direction of the propulsion force. The coupled equations of motion for  $\mathbf{R}(t)$  and  $\phi(t)$ , describing the force balance between the inertial, viscous and random forces, are given by

$$M\ddot{\mathbf{R}}(t) + \xi\dot{\mathbf{R}}(t) = \xi V_p \mathbf{n}(t) + \xi\sqrt{2D}\mathbf{f}_{st}(t), \quad (1)$$

$$J\ddot{\phi}(t) + \xi_r\dot{\phi}(t) = \tau_0 + \xi_r\sqrt{2D_r}\tau_{st}(t). \quad (2)$$

Here,  $M$  and  $J$  are the mass and moment of inertia, respectively, and  $\xi$  and  $\xi_r$  denote the translational and rotational friction coefficients. The translational and rotational Brownian fluctuations are quantified by their respective short-time diffusion coefficients  $D$  and  $D_r$ . The random forces  $\mathbf{f}_{st}(t)$  and torque  $\tau_{st}(t)$  are white noise terms with zero mean and correlation functions  $\langle \mathbf{f}_{st}(t) \otimes \mathbf{f}_{st}(t') \rangle = \delta(t - t')\mathbf{1}$  and  $\langle \tau_{st}(t)\tau_{st}(t') \rangle = \delta(t - t')$ , respectively, where  $\langle \dots \rangle$  denotes the ensemble average and  $\mathbf{1}$  is the unit matrix. Owing to the strong non-equilibrium nature of the system, the diffusion and damping constants are not related by the Stokes–Einstein relation<sup>30</sup>. Moreover, as typical particles are not perfectly symmetrical, they tend to perform circular motions on intermediate time scales. To capture this behaviour, we applied an external torque  $\tau_0$  that induces circular movement with average velocity  $\omega = \tau_0/\xi_r$ <sup>31,32</sup>. Similar models applied in the literature have typically neglected the moment of inertia or have only been solved numerically<sup>1,13,33–37</sup>. The motion of a particle governed by Eqs. (1) and (2) is determined by different time scales given by the friction rates  $\xi/M = \tau^{-1}$  and  $\xi_r/J = \tau_r^{-1}$ , the



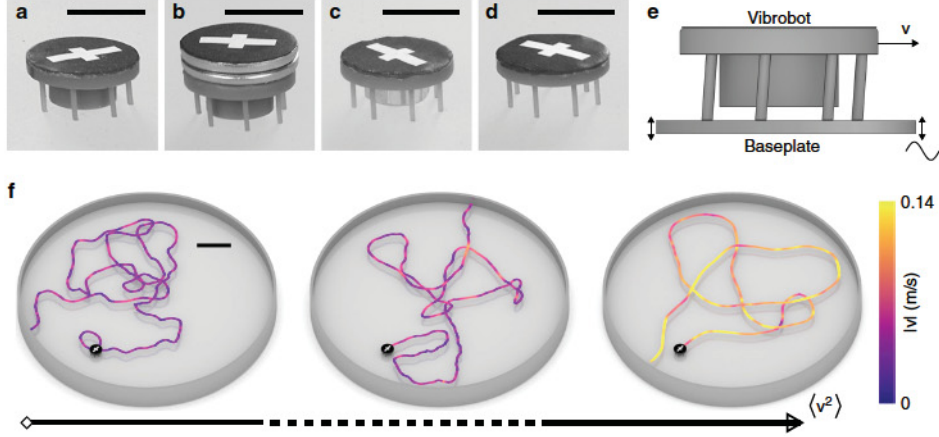


**Fig. 1** 3D-printed particles, setup and trajectories. **a** Generic particle. **b** Carrier particle with an additional outer mass. **c** Tug particle with an additional central mass. **d** Ring particle without a central core. Scale bars represent 10 mm. **e** Illustration of the mechanism with a generic particle on a vibrating plate. **f** Three exemplary trajectories with increasing average particle velocities. Particle images mark the starting point of each trajectory. The trajectory colour indicates the magnitude of the velocity. Scale bar represents 40 mm

rotational diffusion rate  $D_r$ , the angular frequency  $\omega$  and the crossover times  $2D/V_p^2$  and  $2D_r/\tau_0^2$ . In the limit of vanishing  $M$  and  $J$  the model is equivalent to the well-known active Brownian motion formulation<sup>21</sup>.

The trajectories obtained by numerically integrating the Langevin model compare well with the experimental observations. As show by the representative trajectory in Fig. 2d, e, the model reproduces the delay between the orientation and velocity, when the friction is sufficiently weaker than the inertia. The model can be analytically solved by averaging and integration. The orientational correlation

$$\langle \mathbf{n}(t) \cdot \mathbf{n}(0) \rangle_T = \cos(\omega t) e^{-D_r(t - \tau_r(1 - e^{-t/\tau_r}))}, \quad (3)$$

where  $\langle \dots \rangle_T$  is the time average, quantifies the temporal evolution of the active noise term. The periodic cosine term results from the external torque and captures the induced circular motion. The rotational noise, quantified by  $D_r$ , decorrelates the orientation on long-time scales. This decorrelation is described by the exponential term in Eq. (3). The double exponential reflects the additional orientation correlation on short time scales imposed by the inertial damping rate  $\tau_r^{-1}$ . Consequently, the particle dynamics non-trivially depend on the orientation, even in the short- and long-time limits. In the short-time limit the MSD is given by

$$\langle (\mathbf{R}(t) - \mathbf{R}_0)^2 \rangle = \langle \dot{\mathbf{R}}^2 \rangle t^2 \quad (4)$$

with

$$\langle \dot{\mathbf{R}}^2 \rangle = 2D/\tau + f(\mathfrak{D}_0, \mathfrak{D}_1, \mathfrak{D}_2) V_p^2. \quad (5)$$

The first term is the equilibrium solution for a passive particle, and the second term arises from the active motion term. The latter is proportional to  $V_p^2$ , i.e. the kinetic energy injected by the propulsion. This contribution is quantified by the ratio of competing time scales, i.e. the dimensionless delay numbers

$$\mathfrak{D}_0 = D_r \tau_r, \mathfrak{D}_1 = \omega \tau_r, \mathfrak{D}_2 = \tau_r / \tau, \quad (6)$$

through the function

$$f(\mathfrak{D}_0, \mathfrak{D}_1, \mathfrak{D}_2) = \mathfrak{D}_2 e^{\mathfrak{D}_0} \text{Re} \left[ \mathfrak{D}_0^{-(\mathfrak{D}_0 - i\mathfrak{D}_1 + \mathfrak{D}_2)} \times \gamma(\mathfrak{D}_0 - i\mathfrak{D}_1 + \mathfrak{D}_2, \mathfrak{D}_0) \right], \quad (7)$$

where  $\text{Re}$  denotes the real part and  $\gamma$  is the lower incomplete gamma function. The long-time behaviour of the motion is diffusive, with the long-time diffusion coefficient

$$D_L = D + \frac{V_p^2}{2} t(\tau_r, \mathfrak{D}_0, \mathfrak{D}_1). \quad (8)$$

In Eq. (8), the first term is the passive diffusion coefficient and the second term represents the contribution from the driving force with persistence time given by

$$t(\tau_r, \mathfrak{D}_0, \mathfrak{D}_1) = \tau_r e^{\mathfrak{D}_0} \text{Re} \left[ \mathfrak{D}_0^{-(\mathfrak{D}_0 - i\mathfrak{D}_1)} \gamma(\mathfrak{D}_0 - i\mathfrak{D}_1, \mathfrak{D}_0) \right]. \quad (9)$$

Equation (8) is similar to the active Brownian motion model, where the persistence time  $1/D_r$  is replaced by Eq. (9). The long-time diffusion coefficient is therefore a function of the inertial correlations introduced by  $J$  through  $\mathfrak{D}_0$ . This starkly contrasts with passive Brownian motion, which assumes an inertia-independent diffusion coefficient.

**Comparison between model and measurement.** Equations (5) and (8) depend non-trivially on six independent parameters. They are determined by fitting the MSD given by Eq. (4) and the linear and absolute velocity distributions, obtained by numerically solving Eqs. (1) and (2), to the measurements. The measurements and fitting curves for the four different particle types are summarised in Fig. 3. The angular MSDs in Fig. 3a–d show a ballistic short-time regime and a diffusive long-time regime (dashed lines) from which we can determine  $\tau_r$  and  $D_r$  respectively. The  $\phi$ -distribution in Fig. 3e–h is a shifted Gaussian. The minor deviations at small velocities are caused by the finite tracking accuracy. The first moment of this distribution gives the mean angular velocity  $\omega$ . The parameters  $\tau$ ,  $D$  and  $V_p$  are extracted from the linear velocity distributions  $P(v_{\text{lin}}) = P(\dot{X}) = P(\dot{Y})$

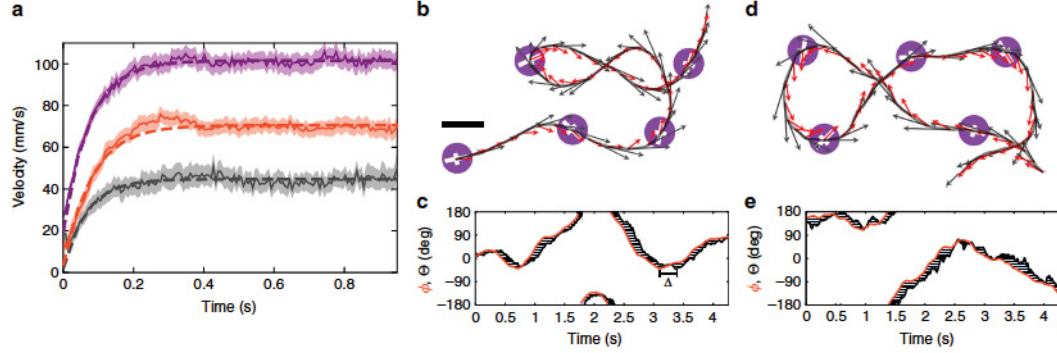


**Fig. 2** Inertial delay in particle trajectories. **a** Time-dependence of the average particle velocity starting from rest at  $t_0$  for three particles with different leg inclinations  $2^\circ$  (grey),  $4^\circ$  (red) and  $6^\circ$  (violet). **b** Measured particle trajectory showing the direction (black arrows) and orientation (red arrows) of a particle. Scale bar represents 20 mm. **c** The measured orientation curve  $\phi(t)$  (red) lags the velocity direction curve  $\Theta(t)$  (black) by an inertial delay  $\Delta$ . **d** Corresponding simulated trajectory with velocity direction (black arrows) and orientation (red arrows). The model parameters are  $\xi/M = 6.46 \text{ s}^{-1}$ ,  $\xi_\theta/J = 5.4 \text{ s}^{-1}$ ,  $D = 8 \times 10^{-5} \text{ m}^2 \text{ s}^{-1}$ ,  $D_\theta = 2.59 \text{ s}^{-1}$ ,  $V_p = 0.092 \text{ ms}^{-1}$ ,  $\omega = 0.7 \text{ s}^{-1}$ . **e** Simulated orientation (red) and velocity curves (black)

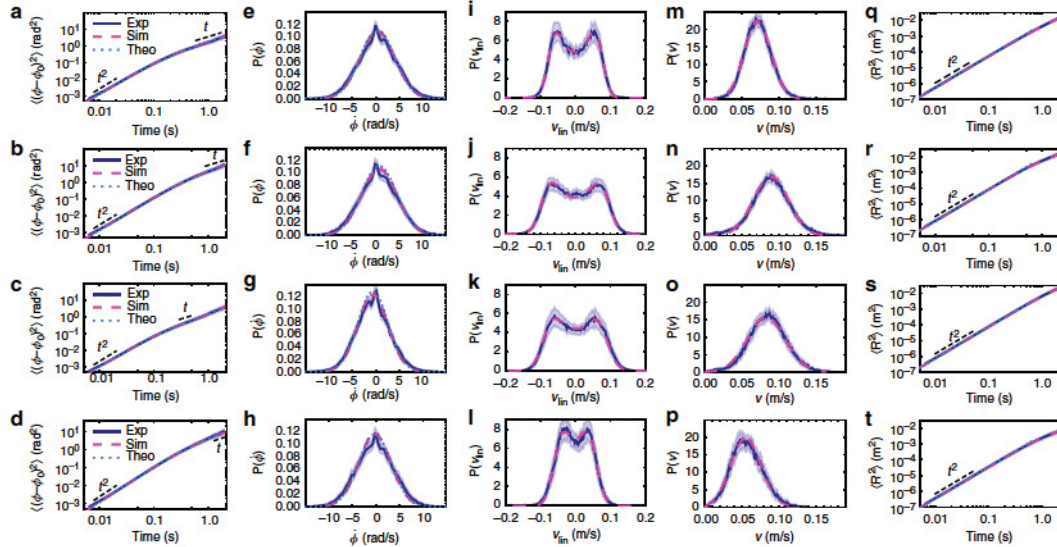


**Fig. 3** Determination of model parameters for the generic, carrier, tug and ring particles (ordered from top to bottom). **a–d** Rotational mean squared displacement, **e–h** rotational velocity distribution, **i–l** linear velocity distribution, **m–p** absolute velocity distribution, **q–t** translational mean squared displacement. Solid dark blue and dashed magenta curves show the experimental data and simulation results, respectively. Dotted light blue plots are the theoretical solutions. Experimental error intervals represent the standard error of the mean (3 s.e.m). The parameter values are listed in Supplementary Table 1

(Fig. 3i–p) and the translational MSDs (Fig. 3q–t), which can be directly fitted by Eqs. (4) and (5). The linear velocity distribution is not a simple Gaussian, but shows a double peak related to the activity. The absolute velocity distribution also clearly deviates from the two-dimensional Maxwell–Boltzmann distribution of passive particles, especially, the maximum is shifted by the propulsion force. The translational MSD mainly depicts the ballistic short-time behaviour, because the persistence length of our particles is of the order of the system size. To test the parameters on an independent quantity, we systematically compared the model with the measured inertial delay. We define the correlation

function

$$C(\dot{\mathbf{R}}(t), \mathbf{n}(t)) = \langle \dot{\mathbf{R}}(t) \cdot \mathbf{n}(0) \rangle_T - \langle \dot{\mathbf{R}}(0) \cdot \mathbf{n}(t) \rangle_T, \quad (10)$$

i.e. the average difference between the projection of the orientation on the initial velocity and projection of the velocity on the initial orientation. This function starts at zero and re-approaches zero in the limit  $t \rightarrow \infty$ . In overdamped systems, Eq. (10) is zero at all times. In the underdamped case the velocity direction pursues the orientation and  $C(\dot{\mathbf{R}}(t), \mathbf{n}(t))$  reaches its maximum after a specific delay. Pronounced peaks, related to the decay



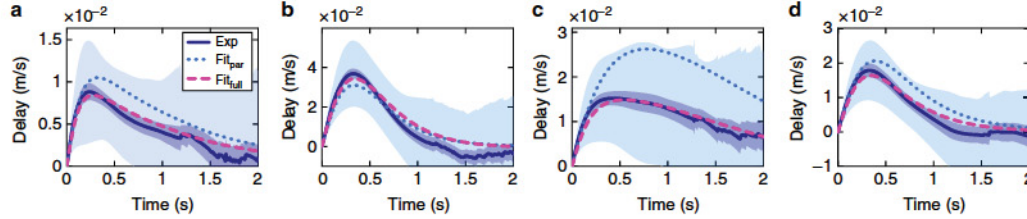


**Fig. 4** Time-dependence of the delay function. Delay functions for the **a** generic, **b** carrier, **c** tug and **d** ring particle. The solid dark blue curve shows the experimental result. The light blue area expresses the standard deviation of the ensemble, the dark blue area illustrates the standard error (2 s.e.m.). The dotted light blue curve is the theoretical expectation for the parameters from Fig. 3. The dashed magenta line is the theoretical expectation where the parameters have been obtained from a full fit to velocity distributions, mean squared displacements and the delay function (see Supplementary Table 2)

numbers and  $\tau_r$  are observed in Fig. 4a–d. The measurements and theoretical predictions using the parameters determined from Fig. 3 are consistent. Some deviations above the statistical error are visible, in particular for the tug particle (dotted line in Fig. 4c), due to overfitting the parameters, when the delay function is not explicitly taken into account. This is confirmed by a more general fit, which minimises the total mean squared error for the curves from Figs. 3 and 4. All curves obtained from this agree with the measurements within the statistical error (see dashed magenta lines in Fig. 4a–d).

**Inertial dependence.** Strikingly, both the short- and long-time particle dynamics in our system depend on the delay number  $\mathfrak{D}_0$ . The fundamental reason is the additional orientational correlation in Eq. (3), which is delayed by the rotational friction rate  $\tau_r^{-1}$ . The exponent in this expression represents the MSD of  $\phi$ , which is dominated by order  $t^2$  at short times and order  $t$  at long times. Consequently, neglecting external torque, this function follows a Gaussian decay at short times and an exponential decay at long times. The significance of the inertial delay is quantified by  $\mathfrak{D}_0$ . For small  $\mathfrak{D}_0$ , the correlation approaches the overdamped result and for large  $\mathfrak{D}_0$  the correlation time is significantly delayed by  $\tau_r$ . To confirm this prediction, we compare the measured correlation functions and the solutions of Eq. (3). The results are consistent, as shown in Fig. 5a.

The numerical and analytical dependence of the ballistic and diffusive regimes on the moment of inertia are displayed in Fig. 5b, c, which show that  $\langle \dot{\mathbf{R}}^2 \rangle$  and  $D_L$  increase with  $J$ . The effects of finite  $J$  can be simply demonstrated mathematically by expanding Eqs. (5) and (8) in the limit  $J \rightarrow 0, \infty$ . As  $J$  vanishes, we find that

$$\lim_{J \rightarrow 0} \langle (\mathbf{R}(t) - \mathbf{R}_0)^2 \rangle = \left( 2D \frac{\xi}{M} + V_P^2 \frac{\xi}{\xi + MD_r} \right) t^2, \quad (11)$$

which agrees with the results reported in ref. <sup>34</sup>. For infinitely large  $J$  we obtain

$$\lim_{J \rightarrow \infty} \langle (\mathbf{R}(t) - \mathbf{R}_0)^2 \rangle = \left( 2D \frac{\xi}{M} + V_P^2 \right) t^2, \quad (12)$$

which simply corresponds to the sum of the thermal and injected kinetic energies. For the long-time diffusion constant the asymptotic behaviour for small moments of inertia is

$$D_L = D + \frac{V_P^2}{2D_r} + \frac{V_P^2}{2\xi_r} J + \mathcal{O}(J^2), \quad (13)$$

which intuitively demonstrates, how, the leading order  $J$  increases the persistence time (namely by a linear term proportional to  $\xi_r$ ).

$J^{-1}$ ). The dependence of  $D_L$  on  $\mathfrak{D}_0$  has no upper bound, and its asymptotic behaviour is described by

$$D_L = D + V_P^2 \sqrt{\frac{\pi}{8D_r \xi_r}} \sqrt{J} + \mathcal{O}(\sqrt{J^{-1}}). \quad (14)$$

The origin of this dependence can be intuitively understood by considering the turn-around manoeuvre of a simple noise-free active particle. When a torque is applied perpendicularly to the velocity, the particle will turn around at point  $P$  and eventually approach circular motion. As the moment of inertia quantifies the resistance of a particle to changing its angular momentum, a particle with low  $J$  will turn faster than one with high  $J$ , as shown in Fig. 5d. This applies only to the transient states, where  $\phi \neq 0$ . In the steady state, the radius  $r$  of the final circle is independent of  $J$ . The angular momentum of an active particle with random reorientations is constantly changing. Its inertia resists these changes and modifies the distribution of reorientations directly opposing the effect of rotational noise.

## Discussion

Our observations demonstrate the profound influence of inertia on the long- and short-time dynamics of self-propelled particles. Considering the relevance of inertia<sup>30</sup>, our model is applicable to various systems, such as levitating<sup>38,39</sup> and floating<sup>40</sup> granular particles and dusty plasmas<sup>41</sup>. It is straightforward to extend the model to elongated particles<sup>5,11,12,14,37,42</sup> and it was shown numerically that collective motion of rod-like particles is well described by similar equations of motion<sup>37</sup>. Qualitatively, in our system, rod-like particles show an inertial delay as well (see Supplementary Fig. 2). In a more general framework, diffusion and friction coefficient could be tensorial and additional non-linear force terms, such as a self-aligning torque reported in refs. <sup>27,33</sup>, might be added to the force balance. Our model predicts that microswimmers perform a short-time ballistic motion like passive particles, but in practice, their motion also depends on their specific propulsion mechanism<sup>43,44</sup> and hydrodynamic effects<sup>45,46</sup>. Generally, the inertial effects will depend on the corresponding time scales in the system. In numerical experiments, this can be demonstrated by gradually reducing the density of hypothetical particles, retaining all other parameters as constants. At very low densities, the MSD exhibits four different regimes: short-time ballistic, short-time diffusive, active ballistic and long-time diffusive regime (see Fig. 6).

The long-time diffusion coefficient of passive particles is independent of inertia and is related to the friction coefficient via the Stokes–Einstein relation. However, for actively moving particles we find an explicit dependence on the moment of inertia



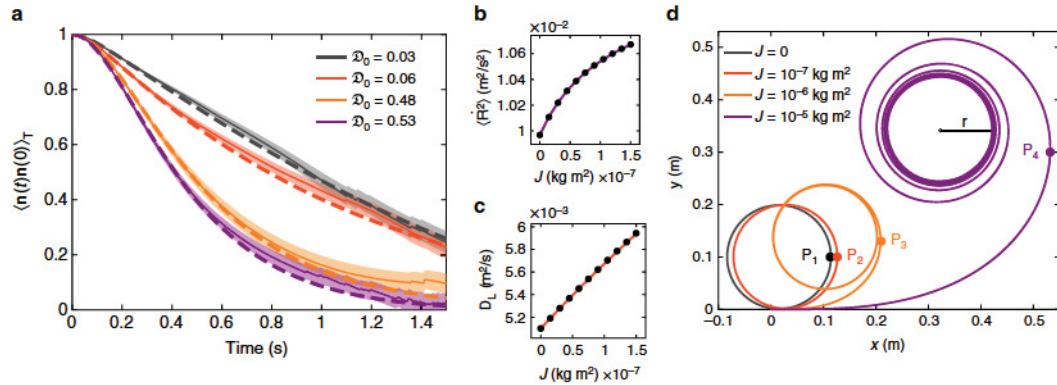


**Fig. 5** Particle dynamics dependence on rotational inertial delay. **a** Time dependence of orientational correlation functions. Solid lines represent the measurements, error bands represent the standard error of the mean. Dashed lines are the analytic results using the parameters from Fig. 3. **b** Slope of the ballistic regime, i.e. the second moment of the velocity  $\langle \dot{\mathbf{r}} \rangle$ , as a function of  $J$  (the circles and solid line are the numerical results and the analytic solution to Eq. (5), respectively). The model parameters (except  $J$ ) are those used in Fig. 6. **c** Long-time diffusion coefficient  $D_L$  as a function of  $J$  (the circles and solid line are the numerical results and the analytic solution to Eq. (8), respectively). **d** Trajectories of active particles under a constant torque applied at  $t_0$ . As  $J$  increases the turn-around manoeuvre becomes increasingly difficult, so the distance and time increase until the turning point  $P_{12,3,4}$  is reached

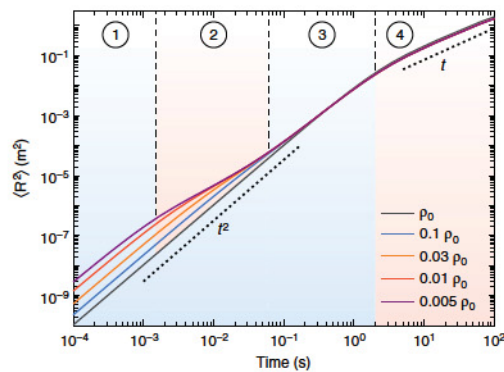


**Fig. 6** Time dependence of MSD for gradually decreasing density. MSD of hypothetical particles with successively reduced material density (i.e.  $M$  and  $J$  are reduced by a common fraction). The other parameters are fixed as  $M_0 = 4$  g,  $J_0 = 1.5 \times 10^{-7}$  kg m<sup>2</sup>,  $\xi/M = 6.5$  s<sup>-1</sup>,  $\xi_r/J = 5.5$  s<sup>-1</sup>,  $D = 1 \times 10^{-4}$  m<sup>2</sup> s<sup>-1</sup>,  $D_r = 1$  s<sup>-1</sup>,  $V_p = 0.1$  ms<sup>-1</sup>,  $\omega = 0$ . When  $\rho = \rho_0$ , two regimes are visible. When the density drops below  $0.01\rho_0$  the MSD divides into four regimes: 1. inertial ballistic, 2. short-time diffusive, 3. active ballistic and 4. active diffusive. In the limit of large damping and vanishing torque the 1-2, 2-3 and 3-4 transition times are given by  $M/\xi$ ,  $D/2V_p^2$  and  $D_r^{-1}$ , respectively

(with no explicit dependence on the total mass  $M$ ). This finding illustrates the importance of  $J$  for macroscopic self-propelled particles. While mass distribution and shape are generally important for efficient motion of animals<sup>47–50</sup> and adaptation to the environment<sup>51,52</sup>, our results suggest that  $J$  can be exploited in novel control strategies for active matter. Biological organisms cannot rapidly vary their mass, but they can change  $J$  by moving their limbs. For instance, cheetahs use tail motion to stabilise fast turns<sup>53</sup>. While the effect on the long-time diffusivity of vibrobots is a few percent, our theory predicts that for flying and floating particles these changes are more dramatic. For similar sized

particles flying in air (e.g. insects) we can expect that friction is about two orders of magnitude smaller. Also, biological organisms can vary their moment of inertia dynamically for up to almost two orders of magnitude, depending on the position and the axis of rotation<sup>54</sup>. In this case, from Eq. (8), the long-time diffusion coefficient changes up to a factor of about three per order of magnitude in  $J$ . By increasing  $J$ , animals can then faster explore a large area. Conversely, by decreasing  $J$ , they can more easily dodge obstacles or predators and counteract sensorial<sup>55</sup> and behavioural delay<sup>16</sup>. Even under conditions, where animals cannot control their rotational deflections, such as aerodynamic turbulence, or during random collisions with neighbours<sup>56</sup>, they could stabilise their movements through variations of  $J$ .

## Methods

**Particle fabrication.** Four particle types were designed and printed: The generic particle consists of a cylindrical core (diameter 9 mm, length 4 mm) topped by a cylindrical cap (diameter 15 mm, length 2 mm). Beneath the cap, seven tilted cylindrical legs (each of diameter 0.8 mm) were attached in parallel in a regular heptagon around the core. The legs lift the bottom of the body by 1 mm above the surface. The typical mass was about  $m = 0.76$  g. From the mass and shape of the particle the moment of inertia was approximated as  $J = 1.64 \times 10^{-8}$  kg m<sup>2</sup>. To vary the propulsion velocity of the particles, we printed five types with different leg inclination angles 0°, 2°, 4°, 6° and 8°.

The carrier particle was fabricated with the same core as generic, but its cap was topped with a 1 mm tall, 8.5 mm diameter cylinder. The carrier socket held two galvanised steel washers, each with an outer diameter of 16 mm and a mass of 1.6 g. The leg inclination of carrier particles was fixed at 2°, and mass and moment of inertia were  $m = 4.07$  g,  $J = 1.46 \times 10^{-7}$  kg m<sup>2</sup>, respectively.

The tug particle was a generic with a fixed leg inclination of 2° and thinner core (diameter 4 mm). This core held a hexagonal M5 threaded galvanised steel nut with a short diagonal and height of 8 and 3.75 mm, respectively. The mass and moment of inertia were  $m = 1.57$  g and  $J = 2.54 \times 10^{-8}$  kg m<sup>2</sup>, respectively.

The ring particle had a leg inclination of 4° and a ring-shaped cap with a hole (diameter 9 mm) in the middle. The mass and moment of inertia were  $m = 0.33$  g and  $J = 1.26 \times 10^{-8}$  kg m<sup>2</sup>, respectively.

All particles were labelled with a simple high contrast image allowing the detection software to identify the particle's position and orientation. The particles were printed from a proprietary methacrylate-based photopolymer (FormLabs Grey V3, FLGPGR03) of typical density 1.11(1) kg/L at a precision of 0.05 mm. They were subsequently cleaned in high purity (>97%) isopropyl alcohol in a still bath, followed by an ultrasound bath, then hardened by three 10-min bursts under four 9 W UVA bulbs. Finally, irregularities were manually filed away and the label sticker was attached.

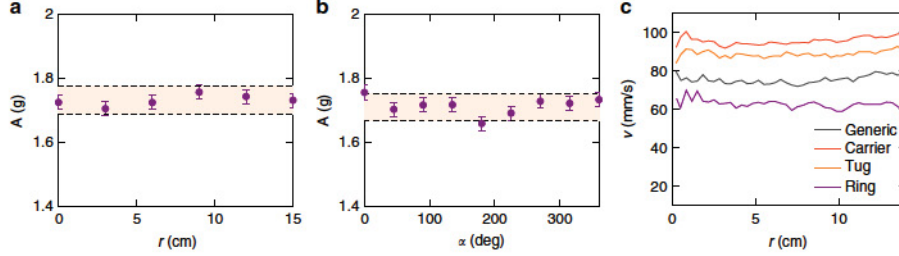


**Fig. 7** Spatial variation of excitation amplitude and particle velocity. Excitation amplitude in dependence of **a** radial positions at a fixed azimuthal angle ( $\alpha = 0$ ) and **b** azimuthal angle at fixed radial position ( $r = 6$  cm). The shaded area illustrates a width of  $\pm 2.5\%$  around the mean. Error bars illustrate the sensorial accuracy (s.e.m.). **c** Average velocity of particles as a function of the radial position for all particle types

**Experimental setup.** The vibrobots were excited by vertical vibrations generated by a circular acrylic baseplate (diameter 300 mm, thickness 15 mm) attached to an electromagnetic shaker (Tira TV 51140) and surrounded by a barrier to confine the particles. The tilt of the plate was adjusted with an accuracy of 0.01°. The vibration frequency and amplitude was set to  $f = 80$  Hz and  $A = 66(4)$   $\mu\text{m}$ , respectively, guaranteeing stable excitation with peak accelerations of 1.7(1)  $g$  (measured by four LIS3DH accelerometers). To ensure homogeneous excitation, the acceleration amplitude was measured at different radial and azimuthal positions in steps of 3 cm and 45° respectively, at constant frequency. The variation of amplitudes at a mean acceleration of 1.7  $g$  is below 5% (see Fig. 7a, b). To ensure that no other factors significantly affect the isotropy of the system, the average particle velocity was measured as a function of the radial distance to the centre (Fig. 7c). The resulting fluctuations are small compared to the mean (standard deviation lies between 1.8 and 3.6% of the respective mean). Experiments were recorded using a high-speed camera system (Allied Vision Mako-U130B) operating at up to 152 fps with a spatial resolution of  $1024 \times 1024$  pixels. Single particles were tracked to sub-pixel accuracy using standard image recognition methods. The tracking accuracy was determined from test measurements of a particle rigidly attached to the plate at different locations. A bivariate Gaussian distribution was fitted to the positions, from which the covariance matrix was obtained. The accuracy  $2 \cdot \sigma_{\text{max}}$  is defined from the maximum of the diagonal entries in this covariance matrices  $\sigma_{\text{max}}^2$  (see Fig. 8a). For the angular position, the error is directly obtained from the 95.4% confidence interval, since the distribution is non-normal due to pixel locking effects (see Fig. 8b). The resulting accuracy is  $\pm 4.7 \times 10^{-4}$  m and  $\pm 0.013$  rad. Multiple single trajectories were recorded for each particle, until 10 min of data were acquired. Events involving particle-border collisions were discarded.

**Analytic results.** The rotational behaviour of the particle was obtained by stochastic integration<sup>57</sup> of Eq. (2). The angular frequency and angular coordinate were obtained as

$$\dot{\phi}(t) = \omega + (\dot{\phi}_0 - \omega)e^{-t/\tau} + \sqrt{2D_t} \frac{\xi}{J} e^{-t/\tau} \int_0^t dt' e^{t'/\tau} \tau_{\text{an}}(t'), \quad (15)$$

and

$$\phi(t) = \phi_0 + \omega t + \frac{\omega - \dot{\phi}_0}{\tau} J (e^{-t/\tau} - 1) + \sqrt{2D_t} \frac{\xi}{J} \int_0^t dt' e^{-t'/\tau} \int_0^{t'} dt'' e^{t''/\tau} \tau_{\text{an}}(t''), \quad (16)$$

respectively. Here,  $\phi_0$  and  $\dot{\phi}_0$  are initial angle and angular velocity, respectively, and the initial time was set to zero. As  $\dot{\phi}(t)$  and  $\phi(t)$  are both linear combinations of Gaussian variables, the corresponding probability distributions are also Gaussian. Thus, by calculating the mean

$$\langle \phi(t) \rangle = \phi_0 + \omega t + \frac{\omega - \dot{\phi}_0}{\tau} J (e^{-t/\tau} - 1), \quad (17)$$

and the variance

$$\mu(t) = 2D_t t + \frac{2D_t}{\tau} J \left( e^{-t/\tau} - 1 - \frac{(e^{-t/\tau} - 1)^2}{2} \right), \quad (18)$$

one obtains the angular probability distribution

$$P(\phi, t) = \frac{1}{\sqrt{2\pi\mu(t)}} \exp\left(-\frac{(\phi - \langle \phi(t) \rangle)^2}{2\mu(t)}\right). \quad (19)$$

At times much longer than the reorientation time scale  $1/D_t$ , and the rotational

friction rate  $J/\xi$ , the variance of the angular distribution far exceeds  $2\pi$ , while the mean cycles between 0 and  $2\pi$ . This behaviour converges to the stationary state with a uniform distribution of  $\phi$ . At times much longer than the rotational friction rate  $J/\xi$ , the stationary distribution of the angular velocity reduces to

$$P(\dot{\phi}) = \sqrt{\frac{J}{2\pi D_t \xi \tau}} \exp\left(-\frac{J(\dot{\phi} - \omega)^2}{2D_t \xi \tau}\right). \quad (20)$$

The width of this distribution is inversely proportional to the moment of inertia.

From the translational equation of motion i.e. Eq. (1), the velocity in the laboratory frame of reference is obtained as

$$\dot{\mathbf{R}}(t) = \dot{\mathbf{R}}_0 e^{-t/\tau} + \frac{\xi}{M} V_p e^{-t/\tau} \int_0^t dt' e^{t'/\tau} \mathbf{n}(t') + \sqrt{2D_t} \frac{\xi}{M} e^{-t/\tau} \int_0^t dt' e^{t'/\tau} \mathbf{f}_{\text{an}}(t'), \quad (21)$$

where the initial velocity is denoted by  $\dot{\mathbf{R}}_0$ . The centre-of-mass position of a particle beginning its motion from the origin is calculated as

$$\mathbf{R}(t) = \mathbf{R}_0 + \dot{\mathbf{R}}_0 \frac{M}{\tau} (1 - e^{-t/\tau}) + \frac{\xi}{M} V_p \int_0^t dt' \int_0^{t'} dt'' e^{-t''/\tau} \mathbf{n}(t'') + \sqrt{2D_t} \frac{\xi}{M} \int_0^t dt' \int_0^{t'} dt'' e^{-t''/\tau} \mathbf{f}_{\text{an}}(t''). \quad (22)$$

The mean square displacement  $\langle R^2 \rangle$  is obtained in the following integral form:

$$\begin{aligned} \langle R^2(t) \rangle &= \dot{\mathbf{R}}_0^2 \frac{M^2}{\tau^2} (1 - e^{-t/\tau})^2 + 2V_p (1 - e^{-t/\tau}) \\ &\times \int_0^t dt' e^{-t'/\tau} \int_0^{t'} dt'' e^{t''/\tau} \dot{\mathbf{R}}_0 \cdot \langle \mathbf{n}(t'') \rangle + \frac{\xi^2}{M^2} V_p^2 \\ &\times \int_0^t dt' e^{-t'/\tau} \int_0^{t'} dt'' e^{t''/\tau} \int_0^{t''} dt''' e^{-t'''/\tau} \\ &\times \int_0^{t'''} dt'''' e^{t''''/\tau} \langle \mathbf{n}(t''') \cdot \mathbf{n}(t'') \rangle + 4D_t t \\ &+ \frac{4D_t}{\tau} M \left( e^{-t/\tau} - 1 - \frac{1}{2} (e^{-t/\tau} - 1)^2 \right), \end{aligned} \quad (23)$$

where  $\langle \mathbf{n}(t) \rangle = e^{-\mu(t)/2} (\cos \langle \phi(t) \rangle, \sin \langle \phi(t) \rangle)$  and  $\langle \mathbf{n}(t_1) \cdot \mathbf{n}(t_2) \rangle$  is defined by

$$\begin{aligned} \langle \mathbf{n}(t_1) \cdot \mathbf{n}(t_2) \rangle &= e^{-D_t |t_1 - t_2| / \tau} \exp\left[-\frac{D_t}{J} \int_{t_1}^{t_2} dt' \right. \\ &\times \left( e^{-\frac{2}{\tau} t_1} + e^{-\frac{2}{\tau} t_2} - \frac{1}{2} (e^{-\frac{2}{\tau} t_1} + e^{-\frac{2}{\tau} t_2}) \right) \\ &\times \cos\left[\omega(t_1 - t_2) + \frac{\omega - \dot{\phi}_0}{\tau} J (e^{-t_1/\tau} - e^{-t_2/\tau})\right]. \end{aligned} \quad (24)$$

The inertial delay correlation function Eq. (10) is given by

$$\begin{aligned} \langle \dot{\mathbf{R}}(t) \cdot \mathbf{n}(0) \rangle_T - \langle \dot{\mathbf{R}}(0) \cdot \mathbf{n}(t) \rangle_T &= V_p D_t e^{D_t t / \tau} \langle \mathbf{D}_0 - \mathbf{D}_t \rangle e^{-t/\tau} \\ &\times \text{Re} \left[ \langle \mathbf{D}_0^{2D_1} \rangle (\langle \mathbf{D}_0 - i\mathbf{D}_1 + \mathbf{D}_2, \mathbf{D}_0 \rangle \right. \\ &- e^{2t/\tau} \langle \mathbf{D}_0^{2D_2} \rangle \gamma(\langle \mathbf{D}_0 - i\mathbf{D}_1 + \mathbf{D}_2, \mathbf{D}_0 e^{-t/\tau} \rangle) \\ &- \gamma(\langle \mathbf{D}_0 - i\mathbf{D}_1 - \mathbf{D}_2, \mathbf{D}_0 e^{-t/\tau} \rangle) \\ &\left. + \gamma(\langle \mathbf{D}_0 - i\mathbf{D}_1 - \mathbf{D}_2, \mathbf{D}_0 \rangle) \right]. \end{aligned} \quad (25)$$

In the stationary case the Fokker–Planck equation of our model projected into one dimension reduces to

$$\int_{-\infty}^{\infty} d\phi \partial_{\dot{\phi}} \left( \frac{\xi}{M} V_p \cos \phi - \frac{\xi}{M} \dot{\phi} - D \left( \frac{\dot{\phi}}{M} \right)^2 \right) P(\dot{\phi}, \phi) = 0. \quad (26)$$



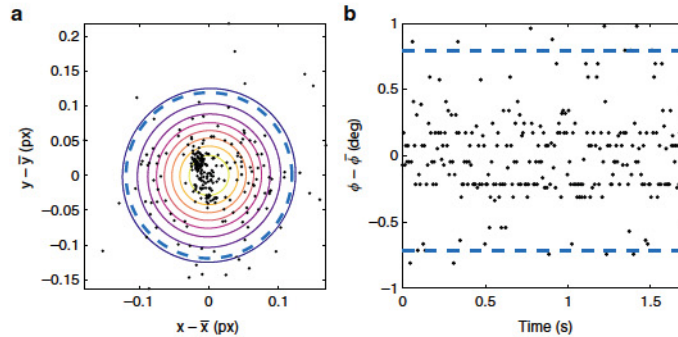


**Fig. 8** Accuracy of spatial and angular detection. **a** Tracked positions of a sticking particle during a time interval of 1.2 s. Solid lines show the isocontours of a bivariate mixed Gaussian distribution. The dashed line shows a circle with a radius equal to two times the square root of the maximum diagonal entry of the covariance matrix. **b** Orientations of a sticking particle. Dashed lines mark the confidence interval that includes at least 95.4% of the data points

One can anticipate the linear velocity distribution to be in the following form:

$$P(\dot{X}) = \frac{1}{\sqrt{2\pi}q} \int_{-\pi}^{\pi} d\phi \frac{1}{2\pi} \exp\left(-\frac{(\dot{X} - W\cos\phi)^2}{2q}\right), \quad (27)$$

where  $q$  and  $W$  are functions of  $D$ ,  $D_0$ ,  $\tau$ ,  $\tau_0$ ,  $V_p$  and  $\omega$ . Analytic approximations for  $q$  and  $W$  are obtained from comparing the second and fourth moments to the solution of the Langevin equation (see Supplementary Methods).

**Parameter matching.** All parameters are obtained from fitting analytic and numeric results to the measurements of MSDs, velocity distributions and eventually the delay function, which describes a cross-correlation between orientation and velocity. The velocity in experiments is defined from the displacement of successive positions of the particle  $\mathbf{v}(t) = (\mathbf{r}(t + \Delta t) - \mathbf{r}(t))/\Delta t$ , where  $\Delta t$  is the time between two frames. Correspondingly the angular velocity is defined as  $\dot{\phi} = (\phi(t + \Delta t) - \phi(t))/\Delta t$ . The recording frame rate is 152 Hz, which corresponds to a minimal  $\Delta t_0 = 0.0066$  s. When  $\Delta t$  is small enough, i.e. below  $\tau$ , such that the ballistic motion of the particle can be captured accurately, the distribution of  $\mathbf{v}$  and  $\dot{\phi}$  will approach the stationary state. In our experiment we find  $\tau$  is on the order of 0.1 s and  $\Delta t = \Delta t_0$  is noticeably smaller. However, to ensure that the choice of  $\Delta t$  does not significantly alter the parameters, fits with  $\Delta t = 2, 3, 4\Delta t_0$  were checked and show no significant difference within the error bars of the parameters. The distribution and delay functions are provided for  $\Delta t = 1, 2, 3, 4\Delta t_0$  in Supplementary Fig. 1 as reference. Note that for the experimental linear velocity distribution, i.e. the distribution of the components of the velocity vector, each trajectory is numerically rotated by a random angle to reduce anisotropy of the distribution that arises from the initial conditions, where each particle, at start, points towards the plate centre.

Initial parameters can be obtained from analytic results of the model directly. The parameters  $\tau$ ,  $D$ , and  $\tau_0$  are straightforwardly determined from fitting the well-known solution to Eq. (2) (Ornstein–Uhlenbeck process). The first moment of the angular velocity distribution gives  $\tau_0 = \omega\tau$ . Angular diffusion coefficient and relaxation time are determined from the fit to the angular MSD.

The determination of the remaining parameters  $D$ ,  $\tau$  and  $V_p$  is more sophisticated. The analytic solution for the initial slope of the translational MSD is given by Eq. (5) and an analytic approximation of the linear velocity distribution is obtained from Eq. (27). The function  $f(\mathcal{D}_0, \mathcal{D}_1, \mathcal{D}_2)$  in Eq. (5) starts from zero and goes asymptotically to 1 as  $\mathcal{D}_2$  grows large, such that it is confined to the interval  $[0, 1]$ . This gives upper and lower bounds for  $V_p$ , namely

$$V_p \in \left[ \sqrt{\langle \dot{X}^2 \rangle - 2D\tau^{-1}}, \sqrt{\langle \dot{X}^2 \rangle - 2D\tau^{-1}} \right]. \text{ Accordingly, the following iterative procedure is used to determine a set of parameters.}$$

The iteration starts with the initial guess  $V_p = \sqrt{\langle \dot{X}^2 \rangle}$  and  $f = 1$ . The analytic approximation of the linear velocity distribution, Eq. (27), is fitted to the measurement to estimate  $\tau$  and  $D$ . After this initial stage, there are two different choices for the post-iterations; either keeping  $f = 1$  and changing the value of  $V_p$  to  $\sqrt{\langle \dot{X}^2 \rangle - 2D\tau^{-1}}$ , or computing the value of  $f$  with respect to the estimated value for  $\tau$  from the pre-iteration, such that  $V_p = \sqrt{\langle \dot{X}^2 \rangle - 2D\tau^{-1}}$ . This leads to two estimates for  $\tau$  and  $D$  via fitting the linear velocity distribution to the outcomes of the experiment.

By comparing the agreement between the resulting  $\tau$  and  $D$  from both choices and the measurement through taking MSD and absolute velocity distribution into account, the estimate with the worst agreement gets discarded. The iteration continues with the accepted estimate for the set of values of the parameters until the resulting curves agree below the standard error.

The resulting set of parameters fit the experimental curves in Fig. 3 with high accuracy. Note that the delay function is not explicitly fitted in this scheme, but used as a cross-check of our parameters. However, this can potentially overfit the parameters, such as for the tug particle (see Fig. 4c). We additionally implemented a numerical optimisation routine (Nelder–Mead optimisation<sup>58</sup>), which fits the numerical solution of the model to all experiment curves (MSDs, velocity distributions and delay function, where velocities are defined such that they match the experimental time scale  $\Delta t_0$ ), by minimising the weighted sum of the mean squared errors. For the generic, carrier and ring particle only minor improvements were found. In the case of the tug particle a significantly better agreement for the delay function can be found by slightly sacrificing the agreement of the other curves. In particular,  $\tau$  and  $D$  are sensitive to small variations. This is in accordance with our model, where only the product of  $\tau$  and  $D$  enters in dominating terms. Nevertheless, the deviation between parameters without and with taking the delay function into account vary in the worst case by about 50% (tug particle) in  $\tau$  and  $D$  and much less for all other parameters. Both sets of parameter values are shown in Supplementary Tables 1 and 2 for comparison. In the latter case an error estimate was obtained from the parameter variation that quadruples the mean squared error.

**Code availability.** The custom code that supports the findings of this study is available from the corresponding authors upon reasonable request.

#### Data availability

The data that support the findings of this study are available from the corresponding authors upon reasonable request.

Received: 19 July 2018 Accepted: 12 November 2018

Published online: 04 December 2018

#### References

- Purcell, E. M. Life at low Reynolds number. *Am. J. Phys.* **45**, 3–11 (1977).
- Blum, J. et al. Measurement of the translational and rotational brownian motion of individual particles in a rarefied gas. *Phys. Rev. Lett.* **97**, 230601 (2006).
- Li, T., Kheifets, S., Medellin, D. & Raizen, M. G. Measurement of the instantaneous velocity of a brownian particle. *Science* **328**, 1673–1675 (2010).
- Huang, R. et al. Direct observation of the full transition from ballistic to diffusive brownian motion in a liquid. *Nat. Phys.* **7**, 576 (2011).
- Gioni, L., Hawley-Weld, N. & Mahadevan, L. Swarming, swirling and stasis in sequestered bristle-bots. *Proc. R. Soc. A* **469**, 20120637– (2013).
- Tsai, J.-C., Ye, F., Rodriguez, J., Gollub, J. P. & Lubensky, T. C. A chiral granular gas. *Phys. Rev. Lett.* **94**, 214301 (2005).
- Briand, G. & Dauchot, O. Crystallization of self-propelled hard discs. *Phys. Rev. Lett.* **117**, 098004 (2016).



8. Scholz, C. & Pöschel, T. Velocity distribution of a homogeneously driven two-dimensional granular gas. *Phys. Rev. Lett.* **118**, 198003 (2017).
9. Junot, G., Briand, G., Ledesma-Alonso, R. & Dauchot, O. Active versus passive hard disks against a membrane: mechanical pressure and instability. *Phys. Rev. Lett.* **119**, 028002 (2017).
10. Scholz, C., Engel, M. & Pöschel, T. Rotating robots move collectively and self-organize. *Nat. Commun.* **9**, 931 (2018).
11. Deblais, A. et al. Boundaries control collective dynamics of inertial self-propelled robots. *Phys. Rev. Lett.* **120**, 188002 (2018).
12. Kudrolli, A., Lumay, G., Volfson, D. & Tsimring, L. S. Swarming and swirling in self-propelled polar granular rods. *Phys. Rev. Lett.* **100**, 058001 (2008).
13. Deseigne, J., Dauchot, O. & Chaté, H. Collective motion of vibrated polar disks. *Phys. Rev. Lett.* **105**, 098001 (2010).
14. Patterson, G. A. et al. Clogging transition of vibration-driven vehicles passing through constrictions. *Phys. Rev. Lett.* **119**, 248301 (2017).
15. Manacorda, A. & Puglisi, A. Lattice model to derive the fluctuating hydrodynamics of active particles with inertia. *Phys. Rev. Lett.* **119**, 208003 (2017).
16. Attanasi, A. et al. Information transfer and behavioural inertia in starling flocks. *Nat. Phys.* **10**, 691 (2014).
17. Cates, M. E. & Tailleur, J. Motility-induced phase separation. *Annu. Rev. Condens. Matter Phys.* **6**, 219–244 (2015).
18. Menzel, A. M. Tuned, driven, and active soft matter. *Phys. Rep.* **554**, 1–45 (2015).
19. Bechinger, C. et al. Active particles in complex and crowded environments. *Rev. Mod. Phys.* **88**, 045006 (2016).
20. Vicsek, T., Czirók, A., Ben-Jacob, E., Cohen, I. & Shochet, O. Novel type of phase transition in a system of self-driven particles. *Phys. Rev. Lett.* **75**, 1226–1229 (1995).
21. Golestanian, R., Liverpool, T. B. & Ajdari, A. Designing phoretic micro- and nano-swimmers. *New J. Phys.* **9**, 126–126 (2007).
22. Alshuler, E., Pastor, J. M., Garcimartín, A., Zuriguel, I. & Maza, D. Vibrot, a simple device for the conversion of vibration into rotation mediated by friction: preliminary evaluation. *PLoS ONE* **8**, e67838 (2013).
23. Koumakis, N., Gnoli, A., Maggi, C., Puglisi, A. & Di Leonardo, R. Mechanism of self-propulsion in 3d-printed active granular particles. *New J. Phys.* **18**, 113046 (2016).
24. Scholz, C., D'Silva, S. & Pöschel, T. Ratcheting and tumbling motion of Vibrots. *New J. Phys.* **18**, 123001 (2016).
25. Walsh, L. et al. Noise and diffusion of a vibrated self-propelled granular particle. *Soft Matter* **13**, 8964–8968 (2017).
26. Lanoiselée, Y., Briand, G., Dauchot, O. & Grebenkov, D. S. Statistical analysis of random trajectories of vibrated disks: towards a macroscopic realization of brownian motion. Preprint at <https://arxiv.org/abs/1712.00770> (2017).
27. Lam, K.-D. N. T., Schindler, M. & Dauchot, O. Self-propelled hard disks: implicit alignment and transition to collective motion. *New J. Phys.* **17**, 113056 (2015).
28. Torres, H., Freixas, V. M. & Perez, D. The Newtonian mechanics of a vibrot. *Rev. Cuba. Física* **33**, 39–43 (2016).
29. Scholz, C. & Pöschel, T. Actively rotating granular particles manufactured by rapid prototyping. *Rev. Cuba. Física* **33**, 37–38 (2016).
30. Jaeger, H. M., Nagel, S. R. & Behringer, R. P. Granular solids, liquids, and gases. *Rev. Mod. Phys.* **68**, 1259–1273 (1996).
31. Kümmel, F. et al. Circular motion of asymmetric self-propelling particles. *Phys. Rev. Lett.* **110**, 198302 (2013).
32. Kurzthaler, C. & Franosch, T. Intermediate scattering function of an anisotropic brownian circle swimmer. *Soft Matter* **13**, 6396–6406 (2017).
33. Weber, C. A. et al. Long-range ordering of vibrated polar disks. *Phys. Rev. Lett.* **110**, 208001 (2013).
34. Mokhtari, Z., Aspelmeier, T. & Zippelius, A. Collective rotations of active particles interacting with obstacles. *Europhys. Lett.* **120**, 14001 (2017).
35. Zhu, W., Huang, X. & Ai, B. Transport of underdamped self-propelled particles in active density waves. *J. Phys. A* **51**, 115101 (2018).
36. Prathyusha, K., Henkes, S. & Sknepnek, R. Dynamically generated patterns in dense suspensions of active filaments. *Phys. Rev. E* **97**, 022606 (2018).
37. Parisi, D. R., Cruz Hidalgo, R. & Zuriguel, I. Active particles with desired orientation flowing through a bottleneck. *Sci. Rep.* **8**, 9133 (2018).
38. Workamp, M., Ramirez, G., Daniels, K. E. & Dijkstra, J. Symmetry-reversals in chiral active matter. *Soft Matter* **14**, 5572–5580 (2018).
39. Farhadi, S. et al. Dynamics and thermodynamics of air-driven active spinners. *Soft Matter* **14**, 5588–5594 (2018).
40. Harth, K., Trittel, T., Wegner, S. & Stannarius, R. Free cooling of a granular gas of rodlike particles in microgravity. *Phys. Rev. Lett.* **120**, 214301 (2018).
41. Ivlev, A. V. et al. Statistical mechanics where newton's third law is broken. *Phys. Rev. X* **5**, 011035 (2015).
42. Sánchez, R. & Daz-Leyva, P. Self-assembly and speed distributions of active granular particles. *Phys. A Stat. Mech. Appl.* **499**, 11–19 (2018).
43. Maass, C. C., Krüger, C., Herminghaus, S. & Bahr, C. Swimming droplets. *Annu. Rev. Condens. Matter Phys.* **7**, 171–193 (2016).
44. Michelin, S. & Lauga, E. Geometric tuning of self-propulsion for janus catalytic particles. *Sci. Rep.* **7**, 42264 (2017).
45. Pesce, G., Volpe, G., Volpe, G. & Sasso, A. Long-term influence of fluid inertia on the diffusion of a brownian particle. *Phys. Rev. E* **90**, 042309 (2014).
46. Elgeti, J., Winkler, R. G. & Gompper, G. Physics of microswimmers - single particle motion and collective behavior: a review. *Rep. Prog. Phys.* **78**, 056601 (2015).
47. Kram, R., Wong, B. & Full, R. Three-dimensional kinematics and limb kinetic energy of running cockroaches. *J. Exp. Biol.* **200**, 1919–1929 (1997).
48. Raichlen, D. A. Effects of limb mass distribution on mechanical power outputs during quadrupedalism. *J. Exp. Biol.* **209**, 633–644 (2006).
49. Dudley, R. & Vermeij, G. J. Do the power requirements of flapping flight constrain folivory in flying animals? *Funct. Ecol.* **6**, 101–104 (1992).
50. Dudley, R. Mechanisms and implications of animal flight maneuverability. *Integr. Comp. Biol.* **42**, 135–140 (2002).
51. Xu, H.-J. et al. Two insulin receptors determine alternative wing morphs in planthoppers. *Nature* **519**, 464 (2015).
52. Lin, X., Xu, Y., Jiang, J., Lavine, M. & Lavine, L. C. Host quality induces phenotypic plasticity in a wing polyphenic insect. *Proc. Natl. Acad. Sci. USA* **115**, 7563–7568 (2018).
53. Wilson, A. M. et al. Locomotion dynamics of hunting in wild cheetahs. *Nature* **498**, 185 (2013).
54. Zatsiorsky, V. M. *Kinetics of Human Motion* (Human Kinetics, Champaign (IL), 2002).
55. Mijalkov, M., McDaniel, A., Wehr, J. & Volpe, G. Engineering sensorial delay to control phototaxis and emergent collective behaviors. *Phys. Rev. X* **6**, 011008 (2016).
56. Zuriguel, I. et al. Clogging transition of many-particle systems flowing through bottlenecks. *Sci. Rep.* **4**, 7324 (2014).
57. Risken, H. Fokker–Planck equation. In *The Fokker-Planck Equation* (Haken, H. (Ed.), Springer, New York, 1996).
58. Nelder, J. A. & Mead, R. A simplex method for function minimization. *Comput. J.* **7**, 308–313 (1965).

#### Acknowledgements

We acknowledge funding by the German Research Foundation (Grant Nos. SCHO 1700/1-1 and LO 418/23-1).

#### Author contributions

C.S. designed the experimental setup. C.S. and A.L. carried out the experiments. C.S., S.J., and A.L. analysed the measurements. S.J. and C.S. wrote the simulation code. S.J. and C.S. performed and analysed the simulations. S.J. developed the theoretical results. All authors discussed the results and wrote the manuscript.


#### Additional information

**Supplementary Information** accompanies this paper at <https://doi.org/10.1038/s41467-018-07596-x>.

**Competing interests:** The authors declare no competing interests.

**Reprints and permission** information is available online at <http://npg.nature.com/reprintsandpermissions/>

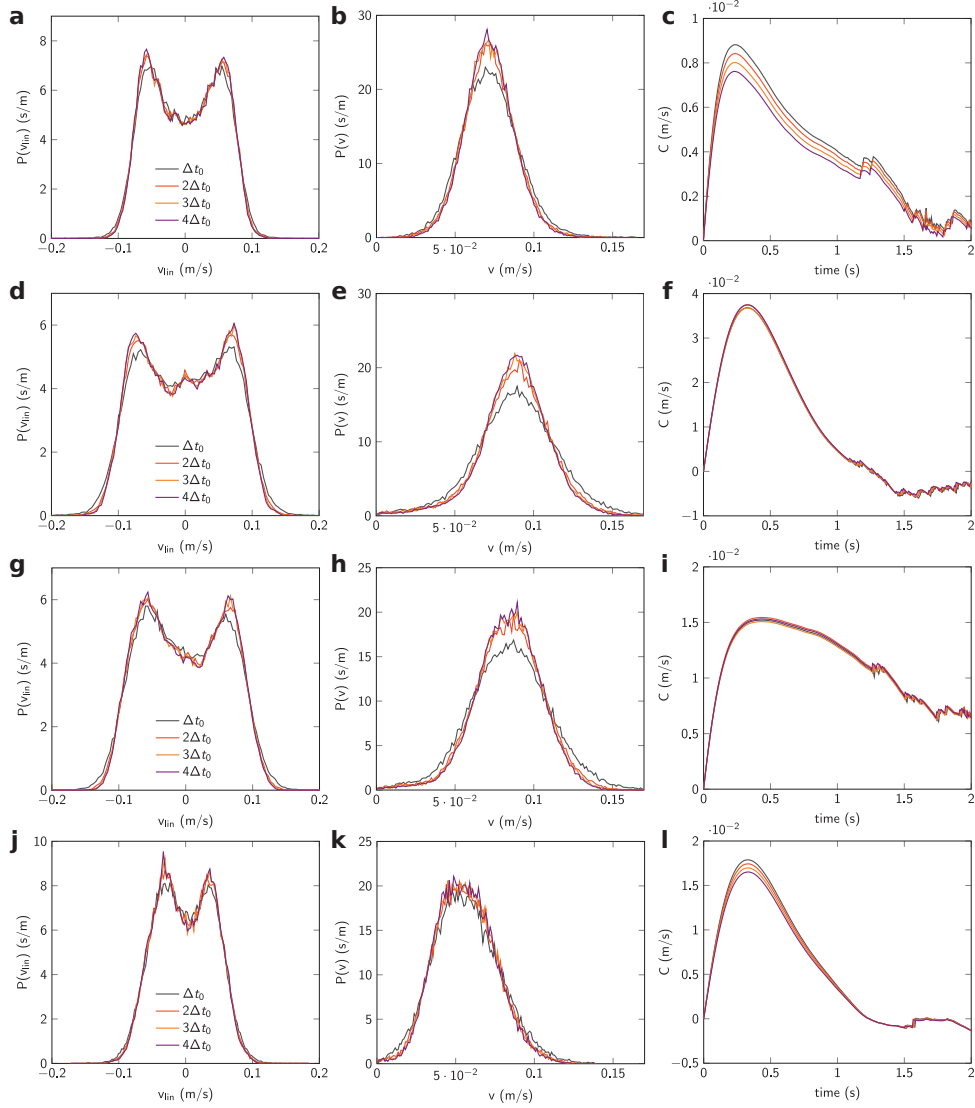
**Publisher's note** Springer Nature remains neutral with regard to jurisdictional claims in published maps and institutional affiliations.

 **Open Access** This article is licensed under a Creative Commons Attribution 4.0 International License, which permits use, sharing, adaptation, distribution and reproduction in any medium or format, as long as you give appropriate credit to the original author(s) and the source, provide a link to the Creative Commons license, and indicate if changes were made. The images or other third party material in this article are included in the article's Creative Commons license, unless indicated otherwise in a credit line to the material. If material is not included in the article's Creative Commons license and your intended use is not permitted by statutory regulation or exceeds the permitted use, you will need to obtain permission directly from the copyright holder. To view a copy of this license, visit <http://creativecommons.org/licenses/by/4.0/>.

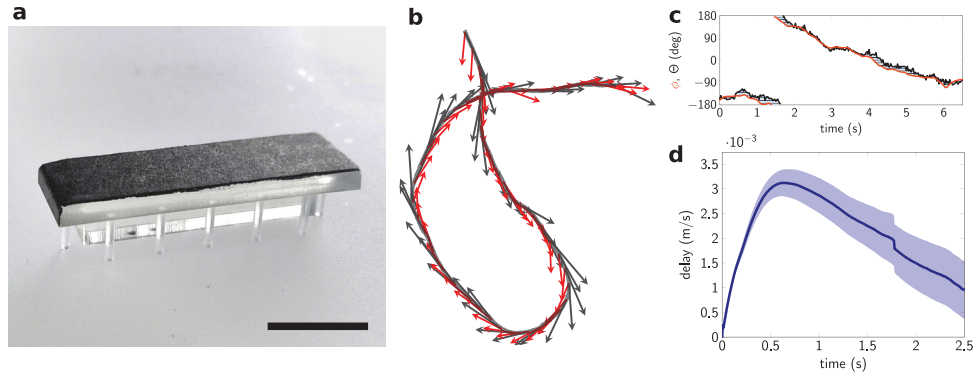
© The Author(s) 2018

**Supplementary Information**  
**Inertial delay of self-propelled particles**

Scholz et al.



**Supplementary Figure 1. Linear and absolute velocity distributions and delay function.** (a-c) Generic particle, (d-e) carrier particle, (g-i) tug particle and (j-l) ring particle. The timescale  $\Delta t$  in the velocity definition is changed in the range 1, 2, 3, 4  $\Delta t_0$ . Only small differences are observed in some curves, which lead only to minor changes in the fit parameters.



**Supplementary Figure 2. Inertial delay of a rod-like particle.** (a) 3D-printed rod-like vibrobot with aspect ratio three, printed from clear resin. Scale bar represents 10 mm. (b) Sample trajectory showing delay of velocity direction (black) and orientation angle (red). (c) Delay between velocity direction angle  $\Theta$  (black) and orientation angle  $\phi$  (red) demonstrates that  $\Theta$  typically lags behind  $\phi$ . (d) Delay function showing the characteristic shape.

**Supplementary Table 1. Mass, moment of inertia and model parameters obtained from analytic solutions and fits to measurements in Fig. 3.**

Particle	M [kg]	J [kg m <sup>2</sup> ]	V <sub>p</sub> [m s <sup>-1</sup> ]	$\tau^{-1}$ [s <sup>-1</sup> ]	D [m <sup>2</sup> s <sup>-1</sup> ]	D <sub>r</sub> [rad <sup>2</sup> s <sup>-1</sup> ]	$\tau_r^{-1}$ [s <sup>-1</sup> ]	$\omega_p$ [rad s <sup>-1</sup> ]
<i>Generic</i>	$0.76 \times 10^{-3}$	$1.64 \times 10^{-8}$	0.071	9.3	$3.56 \times 10^{-5}$	0.91	14.9	0.354
<i>Carrier</i>	$4.07 \times 10^{-3}$	$1.46 \times 10^{-7}$	0.0929	6.85	$7.7 \times 10^{-5}$	2.7	5.1	0.714
<i>Tug</i>	$1.57 \times 10^{-3}$	$2.54 \times 10^{-8}$	0.087	3.0	$2.2 \times 10^{-4}$	0.59	17.6	-0.614
<i>Ring</i>	$0.33 \times 10^{-3}$	$1.26 \times 10^{-8}$	0.057	5.0	$8.4 \times 10^{-5}$	2.4	5.0	-0.19

**Supplementary Table 2. Model parameters obtained from numerical fits to measurements in Fig. 3 and Fig. 4. Experimental uncertainty is specified in brackets in iso notation starting from the last respective digit.**

Particle	V <sub>p</sub> [m s <sup>-1</sup> ]	$\tau^{-1}$ [s <sup>-1</sup> ]	D [m <sup>2</sup> s <sup>-1</sup> ]	D <sub>r</sub> [rad <sup>2</sup> s <sup>-1</sup> ]	$\tau_r^{-1}$ [s <sup>-1</sup> ]	$\omega_p$ [rad s <sup>-1</sup> ]
<i>Generic</i>	0.0708(55)	12.45(211)	$2.48(105) \times 10^{-5}$	0.94(10)	15.20(454)	0.346(13)
<i>Carrier</i>	0.0954(76)	6.11(151)	$8.20(336) \times 10^{-5}$	2.73(35)	5.17(97)	0.734(28)
<i>Tug</i>	0.0846(72)	6.20(120)	$9.74(327) \times 10^{-5}$	0.60(7)	16.78(482)	-0.622(23)
<i>Ring</i>	0.0553(33)	7.15(107)	$5.90(117) \times 10^{-5}$	2.45(13)	4.98(122)	-0.181(4)

## SUPPLEMENTARY METHODS

### Analytic approximation of linear velocity distribution

One can obtain the time-dependent probability distribution through the corresponding Fokker-Planck equation which can be derived from Langevin equations as

$$\begin{aligned}
 -\frac{\partial}{\partial t}P(\mathfrak{R}, t) &= \partial_X \dot{X}P(\mathfrak{R}, t) + \partial_Y \dot{Y}P(\mathfrak{R}, t) + \partial_\phi \dot{\phi}P(\mathfrak{R}, t) \\
 &+ \partial_{\dot{X}} \left( \frac{\xi}{m} V_p \cos \phi - \frac{\xi}{m} \dot{X} - D \left( \frac{\xi}{m} \right)^2 \partial_{\dot{X}} \right) P(\mathfrak{R}, t) \\
 &+ \partial_{\dot{Y}} \left( \frac{\xi}{m} V_p \sin \phi - \frac{\xi}{m} \dot{Y} - D \left( \frac{\xi}{m} \right)^2 \partial_{\dot{Y}} \right) P(\mathfrak{R}, t) \\
 &+ \partial_{\dot{\phi}} \left( \frac{\xi_r}{J} \omega - \frac{\xi_r}{J} \dot{\phi} - D_r \left( \frac{\xi_r}{J} \right)^2 \partial_{\dot{\phi}} \right) P(\mathfrak{R}, t), \tag{1}
 \end{aligned}$$

with  $\mathfrak{R} = (X \ Y \ \phi \ \dot{X} \ \dot{Y} \ \dot{\phi})$ . The stationary distribution is obtained by setting the r.h.s of Supplementary Eq. (1) to zero. Since we are interested in the stationary linear velocity distribution along (for instance)  $X$  direction, we integrate the other variables such that the Fokker Planck equation reduces to

$$\int_{-\infty}^{\infty} d\phi \partial_{\dot{X}} \left( \frac{\xi}{m} V_p \cos \phi - \frac{\xi}{m} \dot{X} - D \left( \frac{\xi}{m} \right)^2 \partial_{\dot{X}} \right) P(\dot{X}, \phi) = 0. \tag{2}$$

Because the stationary distribution of the angle  $\phi$  is uniform, based on Supplementary Eq. (2), one can anticipate the linear velocity distribution to be in the following form

$$P(\dot{X}) = \frac{1}{\sqrt{2\pi q}} \int_{-\pi}^{\pi} d\phi \frac{1}{2\pi} \exp \left( -\frac{(\dot{X} - W \cos \phi)^2}{2q} \right). \tag{3}$$

In analogy to [1], via computing the respective second and forth moments and by using the ansatz of Supplementary Eq. (3),

$$\begin{aligned}
 \langle \dot{X}^2 \rangle &= q + \frac{1}{2} W^2, \\
 \langle \dot{X}^4 \rangle &= 3q^2 + 3qW^2 + \frac{3}{8} W^4, \tag{4}
 \end{aligned}$$

it is deduced that under the condition

$$\mathcal{E}_c = \frac{|\mathfrak{W}^4 - \mathfrak{w}_{\text{dev}}|}{\mathfrak{W}^4} \ll 1, \tag{5}$$

$W$  and  $q$  can be evaluated as

$$\begin{aligned} W &= \mathfrak{W} + \frac{\mathfrak{W}^4 - \mathfrak{w}_{\text{dev}}}{4\mathfrak{W}^3}, \\ q &= D \frac{\xi}{m} - \frac{\mathfrak{W}^4 - \mathfrak{w}_{\text{dev}}}{4\mathfrak{W}^2}, \end{aligned} \quad (6)$$

where

$$\mathfrak{W} = V_p \sqrt{\mathfrak{f}(\mathfrak{D}_0, \mathfrak{D}_1, \mathfrak{D}_2)} \quad (7)$$

and

$$\begin{aligned} \mathfrak{w}_{\text{dev}} &= \mathfrak{D}_2^2 V_p^4 e^{2\mathfrak{D}_0} \mathfrak{D}_0^{-2(2\mathfrak{D}_2 + \mathfrak{D}_0)} \text{Re} \left[ \gamma(3\mathfrak{D}_2 + \mathfrak{D}_0 - i\mathfrak{D}_1, \mathfrak{D}_0) \right. \\ &\quad \times \left[ \gamma(\mathfrak{D}_2 + \mathfrak{D}_0 + i\mathfrak{D}_1, \mathfrak{D}_0) + \mathfrak{D}_0^{2i\mathfrak{D}_1} \gamma(\mathfrak{D}_2 + \mathfrak{D}_0 - i\mathfrak{D}_1, \mathfrak{D}_0) \right. \\ &\quad \times \left( 1 + 2\mathfrak{D}_2 e^{4\mathfrak{D}_0} (4\mathfrak{D}_0)^{-2(\mathfrak{D}_2 + 2\mathfrak{D}_0 - i\mathfrak{D}_1)} \right. \\ &\quad \left. \left. \left. \times \gamma(2\mathfrak{D}_2 + 4\mathfrak{D}_0 - 2i\mathfrak{D}_1, 4\mathfrak{D}_0) \right) \right] \right], \end{aligned} \quad (8)$$

where  $\mathfrak{f}$  is given by Eq. (7) in the main manuscript.

#### SUPPLEMENTARY REFERENCES

- [1] U. Basu, S. N. Majumdar, A. Rosso, and G. Schehr, Preprint at <https://arxiv.org/abs/1804.09027> (2018).



### 3 Normal and anomalous diffusion in active Langevin motion

This chapter is according to an already planned but still ongoing project with the same title by

Soudeh Jahanshahi, and Hartmut Löwen et al.

**Statement of contribution corresponding to this ongoing project**

H.L. has planned the project. I have developed the theoretical results. All authors are discussing the results and editing the manuscript.

### 3.1 Introduction

The non-equilibrium dynamics of the active Brownian particles –also referred to as microswimmers– is typically described in the overdamped limit, where inertial effects are sufficiently negligible relative to viscous ones [94, 144, 145, 24]. This is a good approximation for micron-sized self-propelled particles swimming in a Newtonian liquid where viscous forces are dominant [115]. However, for big active Brownian particles when inertial effects becomes larger or in case of flying in gaseous environment where viscous forces gets smaller, inertial effects are involved in the dynamics. The relevant model to study such flyers with non-negligible or even dominant inertial effects is referred to as *active Langevin motion* [40].

Examples include a complex plasma consisting of mesoscopic dust particles in a weakly ionized gas [41, 42, 43, 44, 45], vibration-driven granular particles [47, 48, 49, 50, 37, 52, 53, 54, 55], animals [60, 61, 62] and insects [63, 64, 65, 66], autorotating seeds and fruits [58, 59], and mini-robots [56, 57]. Most of the previous work of inertial active Langevin motion [67, 68, 69, 70, 38, 71] has included inertia in the translational motion by including a finite particle mass  $m$ , but has ignored inertia in the rotational motion; or in other terms, the moment of inertia  $J$  was set to zero. However, in general, this moment of inertia plays a decisive role as has been shown recently for the example of vibrated granulates (see chapter 2).

The aim of this paper is twofold: first of all, we collect analytical results for the dynamical correlations of a single particle governed by active Langevin dynamics. In particular we present an analytical expression for the time-resolved mean-squared-displacement (MSD) of the particle. In doing so, we generalize the previous expression of Howse et al [94], valid in the overdamped limit where the particle mass  $m$  and the moment of inertia  $J$  are zero, to finite  $m$  and  $J$ . In the long-time limit, as shown in chapter 2, the MSD scales linear in time  $t$  indicating *normal* translational diffusion with a long-time self-diffusion coefficient  $D_L$ .

Second we generalize the equation to a novel situation where all system parameters, namely the self-propulsion speed  $v_p$ , the translational and orientational frictions and noise strengths, and  $m$  and  $J$  depend explicitly on time. A time-dependent moment of inertia,  $J(t)$ , for instance, is motivated by the fact that the maneuverability of animal motion is provided by changes in the body shape [96, 97] which implies a change in the moment of inertia at fixed total mass  $m$ . On the contrary, variable-mass systems, whose mass  $m(t)$  changes with time, comprise another class important in transportation technology. Examples include rockets, which are propelled by continuously losing mass, and robots with discrete mass variation through picking up or releasing objects [100]. Time-dependent mass can bring about time-dependent friction coefficients [101]. Finally, other external stimuli may govern a time-dependence of the other system

parameters. For example, the self-propulsion speed  $V_p(t)$  can be made time-dependent by external optical fields [135], the noise strength and damping by governing the solvent viscosity externally [98, 99] etc.

Here we assume a slow variation in time for these parameters and use an adiabatic approximation to access the MSD. Again we generalize previous work for overdamped systems [111] towards finite mass and moment of inertia. In particular, for a change in the system parameters described by a power law in time we predict a superdiffusive *anomalous* diffusion involving an MSD  $\propto t^\alpha$  which scales as a power law in time with a non-trivial exponent  $\alpha$  [102, 103, 104, 105, 106, 107, 109]. The exponent  $\alpha$  is determined and we also calculate non-adiabatic corrections to the adiabatic limit. Finally we further provide analytical results for the dynamical correlations in case the self-propulsion speed is oscillatory in time. This may mimic and model run-and-tumble motion. In this case, the MSD exhibits again normal diffusion.

Our results can be tested in various experimental set-ups ranging from macroscopic vibrated granular matter, robots or living systems to self-propelled microparticles which are flying in a gaseous medium or in a plasma.

This paper is organized as follows: in sec.3.2, we introduce the theoretical model for active Langevin motion describing a microflyer. We study a microflyer with time-independent self-propulsion, inertia, damping and fluctuations in sec.3.3: the results are provided for both the noise-free case and the general situation with Brownian noise. In sec.3.4, we demonstrate how time-dependent parameters change the dynamics of the system: here, we study slow temporal variations and rapid oscillations. We also present the first order non-adiabatic correction to the adiabatic approximation. In sec.3.5, we consider a microflyer with oscillating propulsion speed, while the other parameters are kept constant: results are provided for both noise-free case and general situation with Brownian noise. Finally, we conclude in sec.3.6.

## 3.2 The basic model of active Langevin motion

In our basic model of active Langevin motion in two dimensions, a microflyer with inertia is characterized by its time-dependent center-of-mass position  $\mathbf{R}(t) = (X(t), Y(t))$  and the orientational unit vector  $\mathbf{n}(t) = (\cos \phi(t), \sin \phi(t))$ , which defines the direction of its internal self-propulsion velocity. The angle  $\phi(t)$  describes its time-dependent orientation. While previous work, as addressed in chapter 2, has considered constant particle mass and moment of inertia, we generalize the model here towards time-dependent parameters: a time-dependent particle mass  $m(t)$ , a time-dependent moment of inertia  $J(t)$  for the rotation around the  $z$ -axis, and a time-dependent self-propulsion velocity  $V_p(t)$ . The time -dependence is imposed externally, i.e.  $m(t)$ ,  $J(t)$  and  $V_p(t)$

are known prescribed functions. In order to give the model as general as possible we also assume in the same spirit a time-dependent external torque  $M(t)$ , a time-dependent translational friction  $\xi(t)$  and a time-dependent rotational friction coefficient  $\xi_r(t)$  and time-dependent noise strengths of the translational and rotational fluctuations. Then the equations of the translational and the rotational motion are governed by the following coupled Langevin equations for  $\mathbf{R}(t)$  and  $\phi(t)$ , respectively, such that

$$\frac{d}{dt} \left( m(t) \dot{\mathbf{R}}(t) \right) + \xi(t) \dot{\mathbf{R}}(t) = \xi(t) V_p(t) \mathbf{n}(t) + \xi(t) \sqrt{2D(t)} \mathbf{f}_{\text{st}}(t), \quad (3.1)$$

$$\frac{d}{dt} \left( J(t) \dot{\phi}(t) \right) + \xi_r(t) \dot{\phi}(t) = M(t) + \xi_r(t) \sqrt{2D_r(t)} M_{\text{st}}(t). \quad (3.2)$$

We use the notations  $\frac{d}{dt} A(t) \equiv \dot{A}(t)$  equivalently for the time derivative of the time-dependent function  $A(t)$ . Here we assumed that the change in translational momentum is equal to the total force and the change in angular momentum is equal to the total torque. As far as the translational dynamics is concerned, the force has a frictional component  $-\xi(t) \dot{\mathbf{R}}(t)$  and a self-propelling effective force along the particle orientation  $\xi(t) V_p(t) \mathbf{n}(t)$ . The latter couples the orientational and translational degrees of freedom. Furthermore there are stochastic forces (“noise”)  $\xi(t) \sqrt{2D(t)} \mathbf{f}_{\text{st}}(t)$  where the effective translational diffusion coefficient  $D(t) > 0$  quantifies the noise strength. We describe the stochastic term  $\mathbf{f}_{\text{st}}(t)$  as zero-mean Markovian white noise with variance

$$\langle \mathbf{f}_{\text{st}}(t) \otimes \mathbf{f}_{\text{st}}(t') \rangle = \delta(t - t') \mathbb{1}, \quad (3.3)$$

where  $\langle \dots \rangle$  indicates a noise average and  $\mathbb{1}$  is the unit matrix. Likewise, the rotational dynamics involves the frictional torque  $-\xi_r(t) \dot{\phi}(t)$  and the imposed torque  $M(t)$  plus the stochastic torque  $\xi_r(t) \sqrt{2D_r(t)} M_{\text{st}}(t)$  where the effective rotational diffusion coefficient  $D_r(t) > 0$  quantifies the rotational noise strength and the Markovian Gaussian noise  $M_{\text{st}}(t)$  has zero-mean and variance

$$\langle M_{\text{st}}(t) M_{\text{st}}(t') \rangle = \delta(t - t'). \quad (3.4)$$

Obviously for constant parameters  $m$ ,  $J$ ,  $\xi$ ,  $\xi_r$ ,  $M$ ,  $D$  and  $D_r$  we recover the standard modeling of active Langevin motion considered earlier. We shall revisit this standard situation again in sec.3.3. In the absence of any inertial effects, i.e. when  $m = J = 0$ , the equations of motion are overdamped and were already considered previously in Ref. [111].

For an analytical solution of the equations of motion we first consider the rotational part Eq.(3.2) which is uncoupled to the translational ones. Denoting the initial conditions for the orientational angle and angular velocity as

$\phi(t=0) = \phi_0$  and  $\dot{\phi}(t=0) = \dot{\phi}_0$ , the solution of Eq. (3.2) is

$$\begin{aligned} \dot{\phi}(t) = & e^{-\Gamma_r(t)} \int_0^t dt' e^{\Gamma_r(t')} \gamma_r(t') \left( \omega(t') + \sqrt{2D_r(t')} M_{\text{st}}(t') \right) \\ & + \dot{\phi}_0 e^{-\Gamma_r(t)}, \end{aligned} \quad (3.5)$$

and thus

$$\begin{aligned} \phi(t) = & \int_0^t dt' e^{-\Gamma_r(t')} \int_0^{t'} dt'' e^{\Gamma_r(t'')} \gamma_r(t'') \left( \omega(t'') + \sqrt{2D_r(t'')} M_{\text{st}}(t'') \right) \\ & + \phi_0 + \dot{\phi}_0 \int_0^t dt' e^{-\Gamma_r(t')}, \end{aligned} \quad (3.6)$$

where  $\Gamma_r(t) = \int_0^t dt' \gamma_r(t') + \ln(J(t)/J(t=0))$ ,  $\gamma_r(t) = \xi_r(t)/J(t)$  and  $\omega(t) = M(t)/\xi_r(t)$ . The temporal behavior of the orientation is characterized by different rotational time scales. The most basic rotational time-scales include the rotational damping time  $\gamma_r^{-1} = J/\xi_r$ , the persistence time  $D_r^{-1}$  and the re-orientation time  $\omega^{-1}$ . Additional time-scales are embedded in the time-scales corresponding to the variations of time-dependent parameters, for instance, the restyling time  $J/\dot{J}$ . In the course of restyling time, the particle restyles its mass distribution around the axis of rotation through change its shape.

According to Eqs. (3.5) and (3.6), both  $\dot{\phi}(t)$  and  $\phi(t)$  are linear combinations of Gaussian variables. This implies that the probability distributions of the angular velocity and orientational angle are Gaussian, uniquely determined by the corresponding means and variances, such that

$$P(\dot{\phi}, t) = \frac{1}{\sqrt{2\pi\mu_1(t)}} \exp \left( -\frac{\left( \dot{\phi}(t) - \langle \dot{\phi}(t) \rangle \right)^2}{2\mu_1(t)} \right), \quad (3.7)$$

and

$$P(\phi, t) = \frac{1}{\sqrt{2\pi\mu_2(t)}} \exp \left( -\frac{\left( \phi(t) - \langle \phi(t) \rangle \right)^2}{2\mu_2(t)} \right). \quad (3.8)$$

Here, the mean of angular velocity and the mean of orientational angle are given by

$$\langle \dot{\phi}(t) \rangle = \dot{\phi}_0 e^{-\Gamma_r(t)} + e^{-\Gamma_r(t)} \int_0^t dt' e^{\Gamma_r(t')} \gamma_r(t') \omega(t'), \quad (3.9)$$

and

$$\begin{aligned} \langle \phi(t) \rangle = & \int_0^t dt' e^{-\Gamma_r(t')} \int_0^{t'} dt'' e^{\Gamma_r(t'')} \gamma_r(t'') \omega(t'') \\ & + \phi_0 + \dot{\phi}_0 \int_0^t dt' e^{-\Gamma_r(t')}, \end{aligned} \quad (3.10)$$

respectively, while the respective variances of the angular velocity and orientational angle are

$$\begin{aligned}\mu_1(t) &= \left\langle \left( \dot{\phi}(t) - \langle \dot{\phi}(t) \rangle \right)^2 \right\rangle \\ &= 2e^{-2\Gamma_r(t)} \int_0^t dt' e^{2\Gamma_r(t')} \gamma_r^2(t') D_r(t'),\end{aligned}\quad (3.11)$$

and

$$\begin{aligned}\mu_2(t) &= \left\langle \left( \phi(t) - \langle \phi(t) \rangle \right)^2 \right\rangle = 4 \int_0^t dt' e^{-\Gamma_r(t')} \\ &\quad \times \int_0^{t'} dt'' e^{-\Gamma_r(t'')} \int_0^{t''} dt''' e^{2\Gamma_r(t''')} \gamma_r^2(t''') D_r(t''').\end{aligned}\quad (3.12)$$

The translational equation of motion yields for the particle velocity

$$\begin{aligned}\dot{\mathbf{R}}(t) &= e^{-\Gamma(t)} \int_0^t dt' e^{\Gamma(t')} \gamma(t') \left( V_p(t') \mathbf{n}(t') + \sqrt{2D(t')} \mathbf{f}_{\text{st}}(t') \right) \\ &\quad + \dot{\mathbf{R}}_0 e^{-\Gamma(t)},\end{aligned}\quad (3.13)$$

where the initial velocity is denoted by  $\dot{\mathbf{R}}_0$  and  $\Gamma(t) = \int_0^t dt' \gamma(t') + \ln(m(t)/m(0))$ . Hence, the center-of-mass position of a microflyer is calculated as

$$\begin{aligned}\mathbf{R}(t) &= \int_0^t dt' e^{-\Gamma(t')} \int_0^{t'} dt'' e^{\Gamma(t'')} \gamma(t'') \left( V_p(t'') \mathbf{n}(t'') + \sqrt{2D(t'')} \mathbf{f}_{\text{st}}(t'') \right) \\ &\quad + \mathbf{R}_0 + \dot{\mathbf{R}}_0 \int_0^t dt' e^{-\Gamma(t')},\end{aligned}\quad (3.14)$$

with  $\mathbf{R}_0 = (X_0, Y_0)$  indicating the initial position. The most basic time-scale corresponding to the translational motion is the translational damping time  $\gamma^{-1} = m/\xi$ . The temporal behavior of time-dependent parameters introduce additional time-scales to the dynamics, such as  $m/\dot{m}$ , namely the time-scale in the course of which the inertia varies.

### 3.3 Time-independent self-propulsion, inertia, damping, and fluctuations

We now turn to the special case for time-independent parameters summarizing some results of chapter 2 but also providing some new analytical results. In doing so, we first consider the noise-free case and then include effects of noise.

### 3.3.1 Results for vanishing noise

Here, we take the dynamics of a circle flyer with constant self-propulsion speed  $v_0$  at zero temperature, when thermal fluctuations vanish, into consideration. The noise-free rotational coordinate of the circle flyer is

$$\phi(t) = \phi_0 + \omega t + \frac{\omega - \dot{\phi}_0}{\gamma_r} (e^{-\gamma_r t} - 1). \quad (3.15)$$

This results in the noise-free translational velocity

$$\dot{\mathbf{R}}(t) = \dot{\mathbf{R}}_0 e^{-\gamma t} + \tilde{\gamma} v_0 \hat{\mathbb{P}} \left[ e^{i(\phi_0 + \dot{\phi}_0 - \tilde{\omega})} \mathcal{L}(\tilde{\omega}, -1, 0) \right], \quad (3.16)$$

which leads to the noise-free translational coordinate

$$\mathbf{R}(t) = \mathbf{R}_0 + \frac{\dot{\mathbf{R}}_0}{\gamma} (1 - e^{-\gamma t}) + \frac{v_0}{\gamma_r} \hat{\mathbb{P}} \left[ e^{i(\phi_0 + \dot{\phi}_0 - \tilde{\omega})} \mathcal{L}(\tilde{\omega}, 1, 1) \right]. \quad (3.17)$$

Here

$$\begin{aligned} \mathcal{L}(\tilde{\omega}, a, b) &= \left( i(\dot{\phi}_0 - \tilde{\omega}) \right)^{\tilde{\gamma} + i\tilde{\omega}} a e^{-\gamma t} \left[ \gamma \left( -\tilde{\gamma} - i\tilde{\omega}, i(\dot{\phi}_0 - \tilde{\omega}) e^{-\gamma_r t} \right) \right. \\ &\quad \left. - \gamma \left( -\tilde{\gamma} - i\tilde{\omega}, i(\dot{\phi}_0 - \tilde{\omega}) \right) \right] + \left( i(\dot{\phi}_0 - \tilde{\omega}) \right)^{i\tilde{\omega}} b \\ &\quad \times \left[ \gamma \left( -i\tilde{\omega}, i(\dot{\phi}_0 - \tilde{\omega}) \right) - a \gamma \left( -i\tilde{\omega}, i(\dot{\phi}_0 - \tilde{\omega}) e^{-\gamma_r t} \right) \right], \end{aligned} \quad (3.18)$$

where

$$\gamma(a, x) = \int_0^x t^{a-1} e^{-t} dt, \quad (3.19)$$

is the lower incomplete gamma function [93]. The letters with a tilde above represent the corresponding parameters now scaled by  $\gamma_r$ , e.g.  $\tilde{D}_r = D_r/\gamma_r$  and  $\tilde{\omega} = \omega/\gamma_r$ . The operator  $\hat{\mathbb{P}} = (\text{Re}, \text{Im})^T$  is defined to extract the real and the imaginary part of the complex function for  $x$  and  $y$  coordinate, respectively.

According to the trajectory given by Eq. (3.17), it takes longer for a microflyer with larger moment of inertia to change its direction of motion and start turning around in response to the effective torque. To be more specific, the higher moment of inertia brings about higher resistance towards any change in the angular velocity. The transient initial revolutions due to the initial transient resistance eventually relax to the final circular flying path

$$\mathbf{R}_{\text{osc}}(t) = \gamma v_0 \hat{\mathbb{P}} \left[ e^{i(\phi_0 + \dot{\phi}_0 - \tilde{\omega})} \mathcal{C}(t, \omega) \right], \quad (3.20)$$

where

$$\mathcal{C}(t, \omega) = \frac{-ie^{i\omega t}}{\omega(\gamma + i\omega)}. \quad (3.21)$$

The center of the final circular motion, after the relaxation of the transient initial regime, is located at

$$\mathbf{R}_c = \mathbf{R}_0 + \frac{\dot{\mathbf{R}}_0}{\gamma} + \frac{v_0}{\gamma_r} \hat{\mathbb{P}} \left[ e^{i(\phi_0 + \dot{\phi}_0 - \tilde{\omega})} \mathcal{L}(\tilde{\omega}, 0, 1) \right], \quad (3.22)$$

while the radius of the final circular flying path is

$$r = \frac{v_0}{\omega} \sqrt{\frac{\gamma^2}{\gamma^2 + \omega^2}}. \quad (3.23)$$

The final flying path and its radius do not depend on the moment of inertia. In contrast, the center of circular motion is an increasing function of the moment of inertia indicating that during the transient initial regime, the stretched particle (with larger  $J$ ) flies away farther than the shrunk one (with smaller  $J$ ). In case of vanishing inertia, i.e.  $\gamma \rightarrow \infty$ , the radius of the final flying path, given by Eq. (3.23), reduces to the radius of the swimming path of a noise-free circle swimmer, i.e.  $r = v_0/\omega$ .

### 3.3.2 Effect of Brownian noise

In case of time-independent self-propulsion, inertia, damping, and fluctuations, the distributions of the angular velocity and orientational angle, given by Eqs. (3.7) and (3.8), become

$$P(\dot{\phi}, t, \dot{\phi}_0) = \frac{\exp\left(\frac{-\left(\dot{\phi} - \omega - \dot{\phi}_0 e^{-\gamma_r t} + \omega e^{-\gamma_r t}\right)^2}{2D_r \gamma_r (1 - e^{-2\gamma_r t})}\right)}{\sqrt{2\pi D_r \gamma_r (1 - e^{-2\gamma_r t})}}, \quad (3.24)$$

and

$$P(\phi, t, \dot{\phi}_0, \phi_0) = \frac{1}{\sqrt{\pi}} \frac{\exp\left(\frac{-\left(\phi - \phi_0 - \omega t - \frac{\omega - \dot{\phi}_0}{\gamma_r} (e^{-\gamma_r t} - 1)\right)^2}{4D_r t + \frac{4D_r}{\gamma_r} \left(e^{-\gamma_r t} - 1 - \frac{(e^{-\gamma_r t} - 1)^2}{2}\right)}\right)}{\sqrt{4D_r t + \frac{4D_r}{\gamma_r} \left(e^{-\gamma_r t} - 1 - \frac{(e^{-\gamma_r t} - 1)^2}{2}\right)}}, \quad (3.25)$$

respectively. In the course of time, the distributions spread over their corresponding domains; while the distribution of the angular velocity reaches its



steady-state around the circling frequency with width  $\sqrt{2D_r\gamma_r}$  for times much larger than the rotational damping time, such that

$$P(\dot{\phi}) = \frac{1}{\sqrt{2\pi D_r\gamma_r}} \exp\left(\frac{-(\dot{\phi} - \omega)^2}{2D_r\gamma_r}\right), \quad (3.26)$$

the distribution of the orientational angle keeps becoming wider as time passing.

In the presence of thermal fluctuations, the rotational mean-square displacement is described via

$$\left\langle \left( \phi(t) - \phi_0 \right)^2 \right\rangle = 2D_r t + \frac{2D_r}{\gamma_r} \left( e^{-\gamma_r t} - 1 \right) + \omega^2 t^2. \quad (3.27)$$

Accordingly, at very early times when  $t \ll \gamma_r^{-1}$  and for very late times  $t \gg \gamma_r^{-1}$ , the circle flyer undergoes a ballistic rotational expansion with circling frequency  $\omega$ . The effects of initial configurations are averaged out by considering a *steady-state initial condition*, i.e., the system reaches the steady-state before the measurement begins. That is to say, averaging over all possible initial configurations results in a steady-state average, for instance,

$$\int d\dot{\phi}_0 P(\dot{\phi}_0) \dot{\phi}_0 = \lim_{t \rightarrow \infty} \langle \dot{\phi}(t) \rangle = \omega, \quad (3.28)$$

$$\int d\dot{\phi}_0 P(\dot{\phi}_0) \dot{\phi}_0^2 = \lim_{t \rightarrow \infty} \langle \dot{\phi}^2(t) \rangle = D_r\gamma_r + \omega^2. \quad (3.29)$$

Here  $P(\dot{\phi}_0)$  is the steady-state distribution of the angular velocity given by Eq. (3.26).

The angular velocity correlation function

$$\langle \dot{\phi}(t)\dot{\phi}(0) \rangle_T = \omega^2 + D_r\gamma_r e^{-\gamma_r t}, \quad (3.30)$$

indicates that the different times' rotational frequencies always remain correlated through the mediation of the circling frequency. Here  $\langle \cdots \rangle_T$  denotes time average, which according to the ergodic hypothesis [86, 87], is equivalent to the steady-state average. Specifically,

$$\langle \dot{\phi}(t)\dot{\phi}(0) \rangle_T = \lim_{\substack{t_1 \rightarrow \infty \\ t_2 \rightarrow \infty}} \langle \dot{\phi}(t_1)\dot{\phi}(t_2) \rangle, \quad (3.31)$$

when the time difference is finite and equal to  $t_1 - t_2 = t$ . While noise average contains the information of the initial configuration, this information is lost through time average.

The exponentially decaying term of the angular velocity correlation function (see Eq. (3.30)) mimics the correlations of a colored noise; that is to say, the

angular velocity imposes an exponentially correlated Gaussian colored noise on the orientational angle [90, 91]. According to the orientational correlation

$$\langle \mathbf{n}(t) \cdot \mathbf{n}(0) \rangle_T = \cos(\omega t) e^{-D_r(t - \gamma_r^{-1}(1 - e^{-\gamma_r t}))}, \quad (3.32)$$

rotational thermal fluctuations cause the orientation to decorrelate on time scales longer than the persistence time. Colored noise induces the additional correlation on time scales shorter than the persistence time.

The correlations in the translational velocity as introduced by

$$\langle \dot{\mathbf{R}}(t) \cdot \dot{\mathbf{R}}(0) \rangle_T = 2D\gamma e^{-\gamma t} + \frac{v_0^2}{2} \tilde{\gamma} e^{-\gamma t} \operatorname{Re} \left[ \mathcal{V}(\omega, t) \right], \quad (3.33)$$

are damped exponentially at the translational damping rate  $\gamma$ . Here the function

$$\begin{aligned} \mathcal{V}(\omega, t) = & e^{\tilde{D}_r \tilde{D}_r^{-}(\tilde{D}_r - i\tilde{\omega} + \tilde{\gamma})} \left[ e^{2\gamma t} \gamma (\tilde{D}_r - i\tilde{\omega} + \tilde{\gamma}, \tilde{D}_r e^{-\gamma_r t}) \right. \\ & - \tilde{D}_r^{2\tilde{\gamma}} \gamma (\tilde{D}_r - i\tilde{\omega} - \tilde{\gamma}, \tilde{D}_r e^{-\gamma_r t}) + \tilde{D}_r^{2\tilde{\gamma}} \gamma (\tilde{D}_r - i\tilde{\omega} - \tilde{\gamma}, \tilde{D}_r) \\ & \left. + \gamma (\tilde{D}_r - i\tilde{\omega} + \tilde{\gamma}, \tilde{D}_r) \right], \end{aligned} \quad (3.34)$$

captures the impact of the additional correlation due to the rotational correlations. This additional correlation is imposed by the rotational damping rate  $\gamma_r$  on short time scales.

The mean-square displacement can be obtained through the velocity correlation function [92], which results in

$$\begin{aligned} \langle (\mathbf{R}(t) - \mathbf{R}_0)^2 \rangle = & 2v_0^2 \operatorname{Re} \left[ \frac{t}{\gamma_r} \mathcal{D}(\omega) + \frac{e^{-\gamma t}}{2\gamma\gamma_r} \Delta(\omega, t) + \mathcal{F}(\omega, t) \right] \\ & + 4D \left( t + \frac{e^{-\gamma t} - 1}{\gamma} \right), \end{aligned} \quad (3.35)$$

with

$$\mathcal{D}(\omega) = e^{\tilde{D}_r \tilde{D}_r^{-}(\tilde{D}_r - i\tilde{\omega})} \gamma (\tilde{D}_r - i\tilde{\omega}, \tilde{D}_r), \quad (3.36)$$

$$\begin{aligned} \Delta(\omega, t) = & e^{\tilde{D}_r \tilde{D}_r^{-}(\tilde{D}_r - i\tilde{\omega})} \left[ \tilde{D}_r^{\tilde{\gamma}} \gamma (\tilde{D}_r - i\tilde{\omega} - \tilde{\gamma}, \tilde{D}_r) + \tilde{D}_r^{-\tilde{\gamma}} e^{2\gamma t} \right. \\ & \times \gamma (\tilde{D}_r - i\tilde{\omega} + \tilde{\gamma}, \tilde{D}_r e^{-\gamma_r t}) + \tilde{D}_r^{-\tilde{\gamma}} (1 - 2e^{\gamma t}) \gamma (\tilde{D}_r - i\tilde{\omega} + \tilde{\gamma}, \tilde{D}_r) \\ & \left. - \tilde{D}_r^{\tilde{\gamma}} \gamma (\tilde{D}_r - i\tilde{\omega} - \tilde{\gamma}, \tilde{D}_r e^{-\gamma_r t}) \right], \end{aligned} \quad (3.37)$$

and

$$\begin{aligned} \mathcal{F}(\omega, t) = \frac{e^{\tilde{D}_r}}{(D_r - i\omega)^2} & \left[ - {}_2F_2(\tilde{\Omega}, \tilde{\Omega}; \tilde{\Omega} + 1, \tilde{\Omega} + 1; -\tilde{D}_r) \right. \\ & \left. + e^{-(D_r - i\omega)t} {}_2F_2(\tilde{\Omega}, \tilde{\Omega}; \tilde{\Omega} + 1, \tilde{\Omega} + 1; -\tilde{D}_r e^{-\gamma_r t}) \right], \end{aligned} \quad (3.38)$$

where in the latter function,  ${}_2F_2$  represents the generalized hypergeometric function [146] and  $\tilde{\Omega} = \tilde{D}_r - i\tilde{\omega}$ .

In the short-time limit, the circle flyer undergoes ballistic motion such that

$$\langle (\mathbf{R}(t) - \mathbf{R}_0)^2 \rangle = \langle \dot{\mathbf{R}}(0) \cdot \dot{\mathbf{R}}(0) \rangle_T t^2, \quad (3.39)$$

where  $\langle \dot{\mathbf{R}}(0) \cdot \dot{\mathbf{R}}(0) \rangle_T$  is the second moment of the velocity obtained through the velocity correlation function (given by Eq. (3.33)) when  $t = 0$ . As moment of inertia vanishes, the ballistic dynamics approaches

$$\lim_{J \rightarrow 0} \langle (\mathbf{R}(t) - \mathbf{R}_0)^2 \rangle = \left( 2D\gamma + \mathcal{K}(\omega, D_r) \right) t^2, \quad (3.40)$$

while as  $J$  grows, it goes to

$$\lim_{J \rightarrow \infty} \langle (\mathbf{R}(t) - \mathbf{R}_0)^2 \rangle = \left( 2D\gamma + \mathcal{K}(\omega, 0) \right) t^2. \quad (3.41)$$

The function  $\mathcal{K}(\omega, D_r)$  is introduced as

$$\mathcal{K}(\omega, D_r) = \frac{v_0^2 \gamma (\gamma + D_r)}{(\gamma + D_r)^2 + \omega^2}. \quad (3.42)$$

The difference between these two limiting behaviors is that in the latter, the impact of rotational fluctuations fades away because of large moment of inertia, i.e. huge resistance towards changing the direction of motion causes the circle flyer to not be influenced by the fluctuating torque. The fact that the term  $2D\gamma$  in Eqs (3.40) and (3.41) is thermal energy, implies that the rest terms are the injected kinetic energy.

The flying dynamics ends up in diffusion for long-time limit with the long-time diffusion coefficient

$$D_L = D + \frac{v_0^2}{2\gamma_r} \operatorname{Re} \left[ \mathcal{D}(\omega) \right]. \quad (3.43)$$

The first term in Eq. (3.43) captures the diffusive behavior of a passive particle when  $v_0 = 0$ . Comparing to microswimmers whose long-time diffusion coefficient is  $D_L = D + v_0^2 D_r^{-1}/2$  when  $\omega = 0$  [94], we characterize the effective persistence time of the circle flyer as

$$\tau(\omega) = \frac{1}{\gamma_r} \operatorname{Re} \left[ \mathcal{D}(\omega) \right]. \quad (3.44)$$

The long-term diffusive behavior therefore depends, not explicitly on mass, but on the mass distribution around the axis of rotation, i.e. on the moment of inertia.

In case of small moments of inertia, the long-time diffusion coefficient of the circle flyer asymptotically goes to

$$D_L = D + \frac{v_0^2}{2} \tau_{cs}(\omega) + \frac{v_0^2 D_r}{2\xi_r} \tau_{cs}(\omega) J + \mathcal{O}(J^2), \quad (3.45)$$

which grows dominantly proportional to moment of inertia. Here

$$\tau_{cs}(\omega) = \frac{D_r}{D_r^2 + \omega^2}, \quad (3.46)$$

represents the effective persistence time of a circle swimmer [95].

The asymptotic behavior of the long-time diffusion coefficient for large moments of inertia in case of vanishing circling frequency is

$$D_L = D + v_0^2 \sqrt{\frac{\pi}{8D_r\xi_r}} \sqrt{J} + \mathcal{O}\left(\sqrt{J}^{-1}\right). \quad (3.47)$$

In case of nonvanishing circling frequency, as moment of inertia grows, the long-time diffusion coefficient goes asymptotically to zero. The reason is that the diffusive circling motion becomes more and more difficult by increasing more and more the moment of inertia, i.e. the circle flyer may get trapped in a circular path since due to its huge moment of inertia, it can not leave this circular *cage*. This results in suppressing the diffusive dynamics.

The function  $\mathcal{F}(\omega, t)$ , provided by Eq. (3.38), captures the oscillating behavior of the mean-square displacement, which is damped by thermal fluctuations with damping rate  $D_r$ . The transient middle time behavior of the mean-square displacement also decays due to the translational friction force. Rotational friction force induces an additional decaying rate to the dynamics, too.

The velocity of the circle flyer –opposed to that of circle swimmer– does not instantaneously follow the orientation. The retarded response of the velocity to the variations of the orientation can be quantified via the average difference between the projection of the velocity on the initial orientation and the projection of the orientation on the initial velocity, i.e.,

$$\begin{aligned} C(\dot{\mathbf{R}}(t), \mathbf{n}(t)) &= \frac{\langle \dot{\mathbf{R}}(t) \cdot \mathbf{n}(0) \rangle_T - \langle \dot{\mathbf{R}}(0) \cdot \mathbf{n}(t) \rangle_T}{v_0} \\ &= \tilde{\gamma} e^{-\gamma t} \operatorname{Re} \left[ c(\omega, t) \right], \end{aligned} \quad (3.48)$$

with

$$\begin{aligned}
 c(\omega, t) = e^{\tilde{D}_r \tilde{D}_r^{-}(\tilde{D}_r - i\tilde{\omega} + \tilde{\gamma})} & \left[ \tilde{D}_r^{2\tilde{\gamma}} \gamma(\tilde{D}_r - i\tilde{\omega} - \tilde{\gamma}, \tilde{D}_r) \right. \\
 & + \gamma(\tilde{D}_r - i\tilde{\omega} + \tilde{\gamma}, \tilde{D}_r) - e^{2\gamma t} \gamma(\tilde{D}_r - i\tilde{\omega} + \tilde{\gamma}, \tilde{D}_r e^{-\gamma_r t}) \\
 & \left. - \tilde{D}_r^{2\tilde{\gamma}} \gamma(\tilde{D}_r - i\tilde{\omega} - \tilde{\gamma}, \tilde{D}_r e^{-\gamma_r t}) \right]. \quad (3.49)
 \end{aligned}$$

Since the nonvanishing identity of the dimensionless correlation  $C(\dot{\mathbf{R}}(t), \mathbf{n}(0))$  stems from the inertial effects, we call it “inertial delay”.

As a function of time,  $C(\dot{\mathbf{R}}(t), \mathbf{n}(0))$  starts from zero at  $t = 0$  and re-approaches zero for times much larger than the damping times. Before decaying, the inertial delay reaches its maximum value, when the velocity direction pursues the orientation with a pronounced delay. Fluctuating torque accelerates the decay rate such that in case of small random torque, the velocity and the orientation remain correlated for a longer time. Circling motion can cause the inertial delay to oscillate between positive and negative values while decaying, until the oscillations damped to zero. During the moments with negative inertial delay, the orientation, due to circling, gets lag behind the velocity direction.

The asymptotic behavior of the inertial delay for small moments of inertia is

$$C(\dot{\mathbf{R}}(t), \mathbf{n}(t)) = 2\mathcal{A}(\omega)\gamma(1 + \frac{D_r}{\xi_r}J) + \mathcal{O}(J^2), \quad (3.50)$$

which intuitively demonstrates, how, the leading order  $J$  increases the inertial delay. Here, the function  $\mathcal{A}(\omega)$  is described as

$$\begin{aligned}
 \mathcal{A}(\omega) = & \left[ D_r(\gamma^2 - Dr^2 - \omega^2)(\cos(\omega t)e^{-D_r t} - e^{-\gamma t}) \right. \\
 & \left. + \omega(\gamma^2 + Dr^2 + \omega^2)\sin(\omega t)e^{-D_r t} \right] \\
 & \times \left[ ((\gamma + D_r)^2 + \omega^2)((\gamma - D_r)^2 + \omega^2) \right]^{-1}. \quad (3.51)
 \end{aligned}$$

As the moment of inertia grows such that it goes to infinity, the inertial delay approaches

$$\lim_{J \rightarrow \infty} C(\dot{\mathbf{R}}(t), \mathbf{n}(t)) = \frac{2\gamma\omega}{\gamma^2 + \omega^2} \sin(\omega t), \quad (3.52)$$

which is independent of  $D_r$ . Specifically, large moments of inertia put the impact of the rotational noise in the shade; hence no decoherence arises in correlations.

### 3.4 Time-dependent self-propulsion, inertia, damping, and fluctuations

Here we study the influence of temporal behavior of different parameters on the dynamics of the circle flyer. To do so, we focus on two different cases: First, slowly varying parameters with respect to time; second, rapidly oscillating parameters. We also present the first order non-adiabatic correction to the adiabatic approximation.

#### 3.4.1 Adiabatic approximation for slow variations

When the parameters involved in the dynamics change gradually in time, the system can be analyzed through adiabatic approximation. Specifically, the microflyer can adapt such rapidly to the slow variations that dynamically it has the same experience as that when the concerning parameters are time-independent; hence we use the results of the previous section, i.e. sec.3.3, to investigate the behavior of a microflyer with temporally varying parameters within adiabatic approximation. Here the variations are considered to be slow if the temporal changes happen on a time-scale much larger than the time-scales of the system.

We investigate the adiabatic dynamics of a microflyer with power-law time dependence in moment of inertia, self-propulsion, rotational friction and diffusion coefficients, namely

$$J(t) = j_0 t^\alpha, \quad V_p(t) = v_0 t^\beta, \quad \xi_r(t) = \xi_{r0} t^\delta, \quad D_r(t) = D_{r0} t^\varepsilon, \quad (3.53)$$

and vanishing circling frequency. In practice, a gradually varying dynamics is obtainable from power-law varying parameters through a two-fold process; first, the time  $t$  is scaled with a large factor  $t_0$ , while  $t \ll t_0$ . Second, the measurements are set to initiate at  $t = t_0$ . Then, for instance, the power-law time dependence  $t^\alpha$  transforms to  $(1 + t/t_0)^\alpha$ . In order to have a gradually varying temporal behavior, the larger the absolute value of the law's exponent, i.e.  $|\alpha|$ , is, the larger the scaling factor  $t_0$  requires.

In case of large moments of inertia, which happens for large  $J_0$ , the long-time mean-square displacement is proportional to

$$\langle (\mathbf{R}(t) - \mathbf{R}_0)^2 \rangle \sim v_0^2 \sqrt{\frac{j_0}{D_{r0} \xi_{r0}}} t^{1+2\beta+(\alpha-\delta-\varepsilon)/2}, \quad (3.54)$$

which is obtained by Eq. (3.47) within adiabatic approximation and gives rise manifestly to anomalous diffusion. If

$$2\beta + (\alpha - \delta - \varepsilon)/2 > 0, \quad (3.55)$$

superdiffusive behavior emerges in long-time dynamics. The microflyer can not undertake subdiffusion in long-time limit since even for  $-1 < 2\beta + (\alpha - \delta - \varepsilon)/2 < 0$ , the subdiffusive behavior of Eq. (3.54) is suppressed by the first term in Eq. (3.47) and a normal diffusive behavior arises, which is equivalent to the passive diffusion with  $\langle (\mathbf{R}(t) - \mathbf{R}_0)^2 \rangle = 4Dt$ .

When  $j_0$  reduces to be small enough, through Eq. (3.45) within adiabatic approximation, we obtain the long-time diffusive behavior to be proportional to

$$\langle (\mathbf{R}(t) - \mathbf{R}_0)^2 \rangle \sim \frac{v_0^2}{D_{r0}} t^{1+2\beta-\varepsilon} + \frac{v_0^2 j_0}{\xi_{r0}} t^{1+2\beta+\alpha-\delta}. \quad (3.56)$$

When

$$2\beta - \varepsilon > 0, \quad (3.57)$$

or

$$2\beta + \alpha - \delta > 0, \quad (3.58)$$

the microflyer performs superdiffusive motion in long-time limit. when the moment of inertia vanishes, i.e. in the limit  $j_0 \rightarrow 0$ , the mean-square displacement agrees with the results of a microswimmer with power-law time-dependent self-propulsion as reported in Ref[111]. In case of  $-1 < 2\beta - \varepsilon < 0$  and  $-1 < 2\beta + \alpha - \delta < 0$ , the subdiffusion, which appears in Eq. (3.56), is overwhelmed by normal diffusion, that stems from random forces.

Temporally varying mass or translational friction coefficient can not alter the long-time dynamics of the circle flyer; however, the short-time dynamics gets affected by variations in mass or  $\xi$  (see Eqs. (3.40) and (3.41)). In case of vanishing noise, which is relevant to the macro variable-mass systems such as rockets, taking into account a time-dependent mass can also change the dynamics significantly (see Eqs. (3.16) and (3.17)).

### 3.4.2 Non-adiabatic correction to the adiabatic approximation

We are interested in the first order non-adiabatic correction to the adiabatic approximation of the temporally-varying parameters. To do so, we use Taylor expansion and keep the linear terms up to the first time derivative of the parameters; for instance,

$$\gamma_r(t) \simeq \gamma_r + \gamma_r' t, \quad (3.59)$$

$$e^{\pm \int_0^t d\tau \gamma_r(\tau)} \simeq e^{\pm \gamma_r t} (1 \pm \gamma_r' \frac{t^2}{2}), \quad (3.60)$$

where  $\gamma_r'$  denotes the first derivative of  $\gamma_r(t)$ . For reason of simplicity, we just present here the corrections to long-time dynamics regarding slow variations in  $\xi_r$  and  $D_r$ . Within adiabatic approximation, the dominant first order non-adiabatic correction to the adiabatic approximation of the long-term diffusive behavior is characterized as

$$\begin{aligned} \langle (\mathbf{R}(t) - \mathbf{R}_0)^2 \rangle (\gamma', D_r') = \text{Re} \left\{ {}_2F_2(\tilde{\Omega}, \tilde{\Omega}; \tilde{\Omega} + 1, \tilde{\Omega} + 1; -\tilde{D}_r) \right. \\ \times \left( \frac{D_r' \gamma_r}{D_r^2} - \frac{\gamma_r'}{D_r} \right) + \gamma_r' D_r \frac{D_r - i\omega + \gamma_r}{\gamma_r (D_r - i\omega)^2} \\ \left. - \frac{D_r'}{(D_r - i\omega)} \right\} 4 \frac{v_0^2}{\gamma_r} e^{D_r/\gamma_r} t^2, \end{aligned} \quad (3.61)$$

where  ${}_2F_2$  denotes the generalized hypergeometric function and  $\tilde{\Omega} = \tilde{D}_r - i\tilde{\omega}$ . Therefore, the first order non-adiabatic correction induces a ballistic phase to the long-time dynamics of the circle flyer. Here we use the notation  $\langle (\mathbf{R}(t) - \mathbf{R}_0)^2 \rangle (\gamma', D_r')$  to emphasize non-adiabatic correction; whereas the full mean-square displacement is obtained within adiabatic approximation through the summation of Eqs. (3.35) and (3.61) and replacing constant  $\gamma_r$  and  $D_r$  with the time-dependent ones.

### 3.4.3 Fast variations

Rapidly varying parameters prevent the system from adapting instantaneously to the changes. Therefore, the dynamics can be approximated by the response of the system to the mean variations of the corresponding time-dependent parameter over a time-window; which should be sufficiently long for the system to perceive the variations and be able to respond to them. Here the variations are fast if the rate of change is much faster than the damping rates.

When the mean variations yield a constant value, the results of sec.3.3 for time-independent parameters are retrieved as a rough estimate for the behavior of the system. For instance, in case of a rapidly oscillating moment of inertia

$$J(t) = j_0 (1 + \sin(\nu_j t)), \quad (3.62)$$

with large frequency  $\nu_j \rightarrow \infty$ , the system can respond to just the average of these fast oscillations over one period, i.e.

$$\overline{J(t)} = j_0 + j_0 \frac{\nu_j}{2\pi} \int_0^{2\pi/\nu_j} dt \sin(\nu_j t) = j_0. \quad (3.63)$$

When  $\omega = 0$ , in the limit  $j_o \rightarrow \infty$  and by using Eq. (3.63), the long-time mean-square displacement yields

$$\langle (\mathbf{R}(t) - \mathbf{R}_0)^2 \rangle \sim 4Dt + 2v_0^2 \sqrt{\frac{\pi j_0}{2D_r \xi_r}} t, \quad (3.64)$$



which is equivalent to the long-time dynamics of a microflyer with large time-independent moment of inertia given by Eq. (3.47). For a sufficiently small moment of inertia, the long-time diffusive behavior becomes

$$\langle (\mathbf{R}(t) - \mathbf{R}_0)^2 \rangle \sim 4Dt + 2\frac{v_0^2}{D_r}t + 2\frac{v_0^2 j_0}{\xi_r}t, \quad (3.65)$$

which resembles the long-time diffusion of a microflyer whose moment of inertia is sufficiently small (see Eq. (3.45)).

### 3.5 Oscillating self-propulsion speed

Here the dynamics of a circle flyer with oscillating propulsion speed is investigated, while inertia, damping, fluctuations, and circling frequency are time-independent. The self-propulsion speed is modeled by

$$V_p(t) = v_0 \left( 1 + \chi \sin(\nu t + \theta_0) \right), \quad (3.66)$$

with the propulsion oscillation frequency  $\nu$ . Here  $v_0\chi$  and  $\theta_0$  are the amplitude and initial phase of the oscillation, respectively, with  $\chi \leq 1$ . We start the discussion with noise-free situation. Then, we take the effect of Brownian noise into account. Subsequently, we just focus on the translational dynamics since the oscillatory behavior of the self-propulsion does not affect the rotational dynamics; namely the rotational dynamics is the same as that in sec.3.3.

#### 3.5.1 Results for vanishing noise

As thermal fluctuations vanish, the noise-free translational velocity becomes

$$\begin{aligned} \dot{\mathbf{R}}(t) = & \tilde{\gamma} v_0 \hat{\mathbb{P}} \left[ e^{i(\phi_0 + \dot{\phi}_0 - \tilde{\omega})} \left( \mathcal{L}(\tilde{\omega}, -1, 0) - i\frac{\chi}{2} e^{i\theta_0} \mathcal{L}(\tilde{\omega} + \tilde{\nu}, -1, 0) \right. \right. \\ & \left. \left. + i\frac{\chi}{2} e^{-i\theta_0} \mathcal{L}(\tilde{\omega} - \tilde{\nu}, -1, 0) \right) \right] + \dot{\mathbf{R}}_0 e^{-\gamma t}, \end{aligned} \quad (3.67)$$

which results in the noise-free translational coordinate

$$\begin{aligned} \mathbf{R}(t) = & \frac{v_0}{\gamma_r} \hat{\mathbb{P}} \left[ e^{i(\phi_0 + \dot{\phi}_0 - \tilde{\omega})} \left( \mathcal{L}(\tilde{\omega}, 1, 1) - i\frac{\chi}{2} e^{i\theta_0} \mathcal{L}(\tilde{\omega} + \tilde{\nu}, 1, 1) \right. \right. \\ & \left. \left. + i\frac{\chi}{2} e^{-i\theta_0} \mathcal{L}(\tilde{\omega} - \tilde{\nu}, 1, 1) \right) \right] + \mathbf{R}_0 + \frac{\dot{\mathbf{R}}_0}{\gamma} (1 - e^{-\gamma t}). \end{aligned} \quad (3.68)$$

Here  $\mathcal{L}(\tilde{\omega}, a, b)$  is provided by Eq. (3.18). The subsequent results are for the situation when the ratio of the frequencies  $\omega$  and  $\nu$  is rational and  $\omega \neq 0$ .

After some transient revolutions, circle flyer arrives in a periodic trajectory with period  $T = 2\pi \text{LCM}(\omega^{-1}, (\omega + \nu)^{-1}, |\omega + \nu|^{-1})$ . Here LCM denotes the lowest common multiple. In special case  $\omega = \nu$ , the period of the trajectory is simply  $T = 2\pi/\omega$ .

Equation (3.68) demonstrates that compared to the *shrunk* circle flyer with smaller  $J$ , when the circle flyer is *stretched*, i.e. in case of larger moment of inertia, the transient initial regime takes longer and during which the particle flies farther away through initial transient revolutions. The transient initial regime eventually relaxes to a periodic motion around the center

$$\begin{aligned} \mathbf{R}_c = & \frac{v_0}{\gamma_r} \hat{\mathbb{P}} \left[ e^{i(\phi_0 + \dot{\phi}_0 - \tilde{\omega})} \left( \mathcal{L}(\tilde{\omega}, 0, 1) - i \frac{\chi}{2} e^{i\theta_0} \mathcal{L}(\tilde{\omega} + \tilde{\nu}, 0, 1) \right. \right. \\ & \left. \left. + i \frac{\chi}{2} e^{-i\theta_0} \mathcal{L}(\tilde{\omega} - \tilde{\nu}, 0, 1) \right) \right] + \mathbf{R}_0 + \frac{\dot{\mathbf{R}}_0}{\gamma}. \end{aligned} \quad (3.69)$$

The final periodic flying path is characterized by

$$\begin{aligned} \mathbf{R}_{\text{osc}}(t) = & \gamma v_0 \hat{\mathbb{P}} \left[ e^{i(\phi_0 + \dot{\phi}_0 - \tilde{\omega})} \left( \mathcal{C}(t, \omega) - i \frac{\chi}{2} e^{i\theta_0} \mathcal{C}(t, \omega + \nu) \right. \right. \\ & \left. \left. + i \frac{\chi}{2} e^{-i\theta_0} \mathcal{C}(t, \omega - \nu) \right) \right], \end{aligned} \quad (3.70)$$

where the function  $\mathcal{C}$  is defined in Eq. (3.21). The final flying path after relaxation of the initial regime is due to an interplay between circling and propulsion frequencies and independent of the moment of inertia. The center of the periodic flying path, on the other hand, is an increasing function of the moment of inertia which illustrates that through transient initial revolutions, the stretched particle flies away farther than the shrunk one.

### 3.5.2 Effect of Brownian noise

In the presence of thermal fluctuations, the translational velocity correlation function is described by

$$\begin{aligned} \langle \dot{\mathbf{R}}(t) \cdot \dot{\mathbf{R}}(0) \rangle_T = & 2D\gamma e^{-\gamma t} + \frac{v_0^2}{2} \tilde{\gamma} e^{-\gamma t} \text{Re} \left[ \mathcal{V}(\omega, t) + \frac{\chi^2}{4} \mathcal{V}(\omega + \nu, t) \right. \\ & \left. + \frac{\chi^2}{4} \mathcal{V}(\omega - \nu, t) \right], \end{aligned} \quad (3.71)$$

where the function  $\mathcal{V}$  is given by Eq. (3.34). This yields the mean-square displacement [92]

$$\begin{aligned} \langle (\mathbf{R}(t) - \mathbf{R}_0)^2 \rangle = & 2 \frac{v_0^2}{\gamma_r} t \operatorname{Re} \left[ \mathcal{D}(\omega) + \frac{\chi^2}{4} \mathcal{D}(\omega + \nu) + \frac{\chi^2}{4} \mathcal{D}(\omega - \nu) \right] \\ & + \frac{v_0^2}{\gamma \gamma_r} e^{-\gamma t} \operatorname{Re} \left[ \Delta(\omega, t) + \frac{\chi^2}{4} \Delta(\omega + \nu, t) + \frac{\chi^2}{4} \Delta(\omega - \nu, t) \right] \\ & + 2v_0^2 \operatorname{Re} \left[ \mathcal{F}(\omega, t) + \frac{\chi^2}{4} \mathcal{F}(\omega + \nu, t) + \frac{\chi^2}{4} \mathcal{F}(\omega - \nu, t) \right] \\ & + 4D \left( t + \frac{e^{-\gamma t} - 1}{\gamma} \right), \end{aligned} \quad (3.72)$$

where functions  $\mathcal{D}$ ,  $\Delta$ , and  $\mathcal{F}$  are provided by Eqs. (3.36), (3.37), and (3.38), respectively.

In the short-time limit, the circle flyer undergoes ballistic motion such that

$$\langle (\mathbf{R}(t) - \mathbf{R}_0)^2 \rangle = \langle \dot{\mathbf{R}}(0) \cdot \dot{\mathbf{R}}(0) \rangle_T t^2. \quad (3.73)$$

As moment of inertia vanishes, the ballistic dynamics approaches

$$\begin{aligned} \lim_{J \rightarrow 0} \langle (\mathbf{R}(t) - \mathbf{R}_0)^2 \rangle = & \left( 2D\gamma + \mathcal{K}(\omega, D_r) + \frac{\chi^2}{4} \mathcal{K}(\omega + \nu, D_r) \right. \\ & \left. + \frac{\chi^2}{4} \mathcal{K}(\omega - \nu, D_r) \right) t^2, \end{aligned} \quad (3.74)$$

while as  $J$  grows, it goes to

$$\begin{aligned} \lim_{J \rightarrow \infty} \langle (\mathbf{R}(t) - \mathbf{R}_0)^2 \rangle = & \left( 2D\gamma + \mathcal{K}(\omega, 0) + \frac{\chi^2}{4} \mathcal{K}(\omega + \nu, 0) \right. \\ & \left. + \frac{\chi^2}{4} \mathcal{K}(\omega - \nu, 0) \right) t^2. \end{aligned} \quad (3.75)$$

The function  $\mathcal{K}$  is introduced in Eq. (3.42). The difference between these two limiting behaviors stems from the fact that a large moment of inertia eliminates the impact of rotational fluctuations. In Eqs (3.74) and (3.75), the term  $2D\gamma$  associates to the thermal energy and the rest is the contribution of the injected kinetic energy.

The long-time diffusion coefficient

$$D_L = D + \frac{v_0^2}{2} \mathcal{T}(\omega, \nu), \quad (3.76)$$

is characterized in terms of the effective persistence time of a circle flyer with oscillating propulsion speed

$$\mathcal{T}(\omega, \nu) = \tau(\omega) + \frac{\chi^2}{4} \tau(\omega + \nu) + \frac{\chi^2}{4} \tau(\omega - \nu). \quad (3.77)$$

Here the function  $\tau$  represents the effective persistence time of a circle flyer with time-independent propulsion speed as shown by Eq.(3.44). The inertial effects affect the long-term diffusive behavior through the moment of inertia.

In case of small moments of inertia, the long-time diffusion coefficient of the circle flyer asymptotically approaches

$$D_L = D + \frac{v_0^2}{2} \mathcal{T}_{cs}(\omega, \nu) + \frac{v_0^2 D_r}{2\xi_r} \mathcal{T}_{cs}(\omega, \nu) J + \mathcal{O}(J^2), \quad (3.78)$$

which is dominantly proportional to the moment of inertia. Here

$$\mathcal{T}_{cs}(\omega, \nu) = \tau_{cs}(\omega) + \frac{\chi^2}{4} \tau_{cs}(\omega + \nu) + \frac{\chi^2}{4} \tau_{cs}(\omega - \nu), \quad (3.79)$$

represents the effective persistence time of a circle swimmer with oscillating propulsion speed [111, 112]. The function  $\tau_{cs}$ , as defined in Eq.(3.46), indicates the effective persistence time of a circle swimmer with time-independent propulsion speed.

As moment of inertia grows, the long-time diffusion coefficient goes asymptotically to zero. This stems from the fact that diffusive circling becomes more difficult by increasing the moment of inertia due to getting trapped in circular cages of the trajectory.

However, the long-time diffusion coefficient of a circle flyer with oscillating propulsion speed asymptotically grows proportional to  $\sqrt{J}$  when  $\omega = \nu$ . This stems from the fact that in this resonance situation, the particle flies with optimum speed along a preferred direction, here  $x$ -direction; circling becomes suppressed and diffusion gets enhanced. The term  $\tau(\omega - \nu)$  in Eq.(3.76) captures the resonance situation while the terms proportional to  $\omega$  and  $\omega + \nu$  vanish as  $J$  grows. As soon as  $\nu$  drives out of resonance, circling motion dominates and long-time diffusion fades away by increasing the moment of inertia.

The oscillatory nature of the self-propulsion does not change the inertial delay, namely the inertial delay is the same as that for a circle flyer with constant propulsion speed. The reason is that the oscillations cancel out each other over the course of each propulsion period, hence only the term corresponding to the constant propulsion, i.e.  $v_0$ , contributes in the inertial delay.

## 3.6 Conclusion

We have investigated the dynamics of a single circling inertia-dominated Brownian particle, which is named circle flyer, by including time-dependence with regard to inertia, self-propulsion, damping and fluctuations. A time delay between the orientation variations and the subsequent changes in the velocity direction depicts the profound influence of inertia on dynamics.

In case of a circle flyer with oscillating propulsion speed and constant inertia, damping, circling frequency and fluctuations, we have found an interesting interplay between circling frequency and propulsion frequency. In the absence of thermal fluctuations, periodic trajectories are observed after passing a transient initial regime. The final flying path is independent of the moment of inertia; however, for larger moments of inertia, it takes more transient revolutions until the regular periodic path is reached. By including thermal noise, we have specifically provided general results for mean-square displacement and inertial delay; whereas the inertial delay is not affected by propulsion oscillations.

Moreover, we have studied the dynamics of a microflyer with time-dependent inertia, damping, self-propulsion and fluctuations. To do so, we have addressed two limiting cases; slow variations and rapid oscillations. We have highlighted that a microflyer can undergo anomalous diffusion if temporally varying parameters are included. The first order non-adiabatic correction to the adiabatic approximation is also presented, which demonstrates a transition to the ballistic regime.

This study emphasizes that the diffusion transport process can be adjusted by taking into account an appropriate time-dependence with regard to the system's parameters. For future studies, it is interesting to take a mixture of inertia-dominated Brownian particles into account and investigate the collective behavior of such a system in simple or complex environments.





## 4 Localization of a microswimmer in a triangular trap

This chapter is according to the basic model of the following paper submitted to Science Advances

### **Realization of a motility-trap for active particles**

Soudeh Jahanshahi, Celia Lozano, Benno Liebchen, Hartmut Löwen, and Clemens Bechinger

### **Statement of contribution corresponding to this submitted paper**

C.B. and H.L. have planned the project. C.L. has performed the experimental research. I have written the simulation codes and performed and analyzed the simulations. B.L. has proposed the theory for sensing. I have prepared the theoretical results. All authors have discussed and interpreted the results and have written and edited the manuscript.

## 4.1 Introduction

The development of particle trapping techniques which allows controlling the number density and configuration of micron- and nano-sized objects has promoted some of the most spectacular advancements in fundamental and applied science throughout the past few decades. In particular at small length scales, where the particle's motion is governed by thermal noise, their spatial confinement requires additional effort which has lead to the development of e.g. Paul and Penning traps or optical and magnetic tweezers [147, 148, 149].

The resemblance of active colloids with living organisms, makes them versatile model systems to study the response of organisms to external stimuli [150]. However, confinement of these active Brownian agents in an efficient and experimentally realizable mechanism is still a challenge. So far, only little attempts have been performed to develop generic mechanisms for localizing Brownian self-propelled particles, for instance, some studies have presented near-harmonic trap models for confinement within external potentials via utilizing optical landscapes [121], acoustic tweezers [151], or even gravitation [55], or using optical gradient [78] to trap such particles.

In this letter, we introduce a trapping mechanism induced by phototaxis for localizing active colloids. We report one-dimensional confinement of a single self-propelled particle, which moves on a two-dimensional substrate, by phototactic motion in a triangular trap. This creates a semi one-dimensional active diffusion, which brings about an improved functionality of microswimmers in sensing applications, such as telemetry and monitoring.

## 4.2 Theory

In our trapping mechanism, the bias in dynamics required generally for a tactic motion is created by an aligning torque which rotates the orientation towards intensity extremum, i.e. towards minimum or maximum of intensity for negative and positive phototaxis, respectively. In fact, the key quantity in confining process is the aligning rate, which reads as

$$\omega(\varphi, x) = \frac{c}{\sigma} v_p(x) v_p'(x) \sin \varphi. \quad (4.1)$$

Here,  $c$  is a common prefactor, which follows from experiments;  $c$  is negative (positive) for positive (negative) phototaxis case.  $v_p(x)$  and  $v_p'(x) = \frac{dv_p(x)}{dx}$  denote the propulsion velocity and its gradient, respectively. The magnitude of the aligning torque is inversely tuned by the particle diameter  $\sigma$ .

An active particle phototaxes by a net motion of its center along the gradient of the light intensity field, i.e. along the  $x$ -direction, in a steady triangular motility

profile. For negative phototactic motion, the active particle is trapped by oscillating along a short path around the trap center where the propulsion velocity is minimum. Whereas in case of positive phototaxis, the confinement is limited to the regions with the highest propulsion velocities. By attributing an effective temperature to the self-propulsion speed, we call the former case “cooling trap” and the latter one “heating trap”.

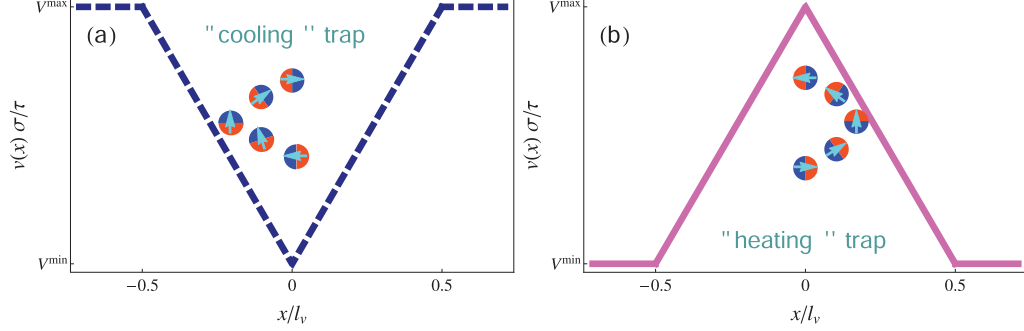


**Figure 4.1:** Schematic view of (a) cooling trap and (b) heating trap.

We describe the motion of particle’s center-of-mass  $\mathbf{r}(t) = (x(t), y(t))$  and orientation  $\hat{\mathbf{n}} = (\cos(\varphi), \sin(\varphi))$  by coupled overdamped Langevin equations with Gaussian noise. In detail, the respective translational and rotational motion are governed by

$$\dot{\mathbf{r}}(t) = v_p(x) \hat{\mathbf{n}} + \sqrt{2D} \boldsymbol{\xi}(t), \quad (4.2)$$

and

$$\dot{\varphi}(t) = \omega(\varphi, x) + \sqrt{2D_r} \xi_\varphi(t). \quad (4.3)$$

$\boldsymbol{\xi}(t) = (\xi_x(t), \xi_y(t))$  and  $\xi_\varphi(t)$  describe zero-mean Markovian white noise, with the variance

$$\langle \boldsymbol{\xi}(t) \otimes \boldsymbol{\xi}(t') \rangle = \delta(t - t') \mathbf{1} \quad (4.4)$$

and

$$\langle \xi_\phi(t) \xi_\phi(t') \rangle = \delta(t - t'), \quad (4.5)$$

where  $\langle \cdot \rangle$  indicates a noise average,  $\otimes$  denotes the dyadic product, and  $\mathbf{1}$  is the unit matrix. The translational and rotational diffusion coefficients are represented by  $D$  and  $D_r$ , respectively.

For cooling trap (see Fig.4.1 (a)), the steady triangular motility profile is defined as

$$v_p(x) = \begin{cases} 2 \frac{V^{\max} - V^{\min}}{l_v} |x| + V^{\min} & \text{for } |x| \leq l_v/2 \\ V^{\max} & \text{else} \end{cases}, \quad (4.6)$$

while in case of heating trap (see Fig.4.1 (b)), it is specified by

$$v_p(x) = \begin{cases} -2 \frac{V^{\max} - V^{\min}}{l_v} |x| + V^{\max} & \text{for } |x| \leq l_v/2 \\ V^{\min} & \text{else} \end{cases}. \quad (4.7)$$

Here,  $l_v$  is the characteristic spacing of the motility field spatially varying between the maximum value  $V^{\max}$  and the minimum value  $V^{\min}$ . In simulation, the typical Brownian time  $\tau = \sigma^2/D$  and the diameter of the particle  $\sigma$  are considered as time and length scales, respectively.

The noise-free dynamics can be obtained by solving Eqs.(4.2) and (4.3) for vanishing diffusion coefficients. Specifically, when thermal noise vanishes and  $V^{\min} = 0$ , the dynamics of  $x$ -coordinate follows from the integral equation

$$\int_{x_0}^{x(t)} \frac{dx'}{|x'| \sqrt{1 - \sin^2(\varphi_0) \exp[4 \frac{c V^{\max}}{\sigma l_v} (|x'| - |x_0|)]}} = 2 \frac{V^{\max}}{l_v} t. \quad (4.8)$$

Here, the particle starts its motion from the trap center  $x_0$  with the initial rotational angle  $\varphi_0$ .

Since the swimmer's motion along  $x$ -direction is confined, the mean-square displacement of the  $x$ -coordinate reaches a plateau after some time. We introduce the *confinement length* as the square root of the mean-square displacement at the plateau. The confinement length tunes inversely with the motility contrast.

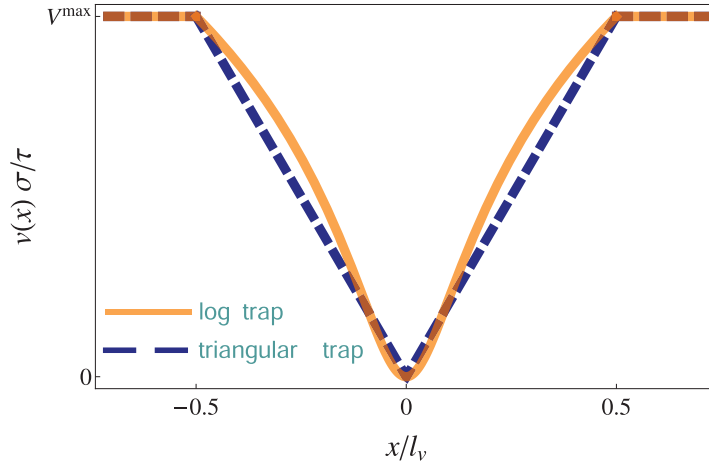


**Figure 4.2:** Schematic view of how a triangular trap can be mimicked by a logarithmic one.

In order to investigate the transition from delocalization to localization, we introduce a negative phototaxis logarithmic trap through a motility profile

$$v_p(x) = \frac{V^{\max}}{\ln \left( \sqrt{(l_v/2)^2 + 1} \right)} \ln \left( \sqrt{x^2 + 1} \right) \quad \text{for } |x| \leq l_v/2, \quad (4.9)$$

in which  $V^{\min}$  is assumed to be zero. In principle, the triangular trap can be assumed to be mimicked by this logarithmic trap with curved walls and smooth bottom (see Fig.4.2). The noise-free probability distribution along  $x$ -direction is obtained as follows

$$P(x) = \frac{c V^{\max}}{\sigma \pi} \frac{|x|}{\ln \left( \sqrt{(l_v/2)^2 + 1} \right)} (x^2 + 1)^{-1 - \frac{c V^{\max}}{2\sigma \ln \left( \sqrt{(l_v/2)^2 + 1} \right)}} \left( 1 - (x^2 + 1)^{-\frac{c V^{\max}}{\sigma \ln \left( \sqrt{(l_v/2)^2 + 1} \right)}} \right)^{-1/2}. \quad (4.10)$$

Based on the leading order analysis, by taking the second moment  $\langle x^2 \rangle$  into account, the condition to have a localized particle is

$$\delta = \frac{c V^{\max}}{2\sigma \ln \left( \sqrt{(l_v/2)^2 + 1} \right)} > 1. \quad (4.11)$$

For  $\delta < 1$  the particle is delocalized and the transition from localization to delocalization happens when  $\delta = 1$ .





# 5 Colloidal Brazil nut effect in microswimmer mixtures induced by motility contrast

Reproduced from

Soudeh Jahanshahi, Celia Lozano, Borge ten Hagen, Clemens Bechinger, and  
Hartmut Löwen

The Journal of Chemical Physics **150**, 114902 (2019)

published by *AIP Publishing*

Digital Object Identifier (DOI): 10.1063/1.5083098

Link to version of record:

<https://aip.scitation.org/doi/full/10.1063/1.5083098>

with the permission of AIP Publishing

## Statement of contribution

H.L. and C.B. have planned the project. I and C.L. have performed the theoretical and experimental research, respectively. All authors have discussed and interpreted the results and have written and edited the manuscript.

## Copyright and license notice

©AIP Publishing LLC

AIP Publishing permits authors to reuse their own AIP Publishing article in their theses or dissertations.

## Colloidal Brazil nut effect in microswimmer mixtures induced by motility contrast F

Cite as: J. Chem. Phys. **150**, 114902 (2019); <https://doi.org/10.1063/1.5083098>

Submitted: 28 November 2018 . Accepted: 25 January 2019 . Published Online: 19 March 2019

Soudeh Jahanshahi, Celia Lozano , Borge ten Hagen, Clemens Bechinger , and Hartmut Löwen

### **COLLECTIONS**

Note: This article is part of the Special Topic "Chemical Physics of Active Matter" in J. Chem. Phys.

F This paper was selected as Featured



View Online



Export Citation



CrossMark

### **ARTICLES YOU MAY BE INTERESTED IN**

[Brownian dynamics of a neutral protein moving through a nanopore in an electrically biased membrane](#)

The Journal of Chemical Physics **150**, 115103 (2019); <https://doi.org/10.1063/1.5080944>

[Theory of light-activated catalytic Janus particles](#)

The Journal of Chemical Physics **150**, 114903 (2019); <https://doi.org/10.1063/1.5080967>

[Modeling and analyzing a photo-driven molecular motor system: Ratchet dynamics and non-linear optical spectra](#)

The Journal of Chemical Physics **150**, 114103 (2019); <https://doi.org/10.1063/1.5086948>

Where in the **world** is AIP Publishing?  
*Find out where we are exhibiting next*



J. Chem. Phys. **150**, 114902 (2019); <https://doi.org/10.1063/1.5083098>

**150**, 114902

© 2019 Author(s).

# Colloidal Brazil nut effect in microswimmer mixtures induced by motility contrast



Cite as: J. Chem. Phys. 150, 114902 (2019); doi: 10.1063/1.5083098

Submitted: 28 November 2018 • Accepted: 25 January 2019 •

Published Online: 19 March 2019



Soudeh Jahanshahi,<sup>1</sup> Celia Lozano,<sup>2</sup> Borge ten Hagen,<sup>3</sup> Clemens Bechinger,<sup>2</sup> and Hartmut Löwen<sup>1</sup>

## AFFILIATIONS

<sup>1</sup>Institut für Theoretische Physik II: Weiche Materie, Heinrich-Heine-Universität Düsseldorf, D-40225 Düsseldorf, Germany

<sup>2</sup>Fachbereich Physik, Universität Konstanz, Konstanz D-78457, Germany

<sup>3</sup>Physics of Fluids Group and Max Planck Center Twente, Department of Science and Technology, MESA+ Institute, and J. M. Burgers Centre for Fluid Dynamics, University of Twente, 7500 AE Enschede, The Netherlands

**Note:** This article is part of the Special Topic "Chemical Physics of Active Matter" in J. Chem. Phys.

## ABSTRACT

We numerically and experimentally study the segregation dynamics in a binary mixture of microswimmers which move on a two-dimensional substrate in a static periodic triangular-like light intensity field. The motility of the active particles is proportional to the imposed light intensity, and they possess a motility contrast, i.e., the prefactor depends on the species. In addition, the active particles also experience a torque aligning their motion towards the direction of the negative intensity gradient. We find a segregation of active particles near the intensity minima where typically one species is localized close to the minimum and the other one is centered around in an outer shell. For a very strong aligning torque, there is an exact mapping onto an equilibrium system in an effective external potential that is minimal at the intensity minima. This external potential is similar to (height-dependent) gravity such that one can define effective "heaviness" of the self-propelled particles. In analogy to shaken granular matter in gravity, we define a "colloidal Brazil nut effect" if the heavier particles are floating on top of the lighter ones. Using extensive Brownian dynamics simulations, we identify system parameters for the active colloidal Brazil nut effect to occur and explain it based on a generalized Archimedes' principle within the effective equilibrium model: heavy particles are levitated in a dense fluid of lighter particles if their effective mass density is lower than that of the surrounding fluid. We also perform real-space experiments on light-activated self-propelled colloidal mixtures which confirm the theoretical predictions.

Published under license by AIP Publishing. <https://doi.org/10.1063/1.5083098>

## I. INTRODUCTION

The physics of active colloidal matter is a rapidly expanding research area on nonequilibrium phenomena. Typically, active suspensions are composed of self-propelled particles on the micron scale, swimming in a fluid at low Reynolds number.<sup>1–5</sup> The main focus of research has been both on the individual swimming mechanism and on collective effects of many such microswimmers.<sup>6</sup> The individual swimming speed of a single particle, also called particle motility, is typically of the order of microns per second and can be steered externally by various means.<sup>7–21</sup>

Recently, the behavior of microswimmers has been explored in externally imposed motility fields where the

swimming speed depends on the spatial coordinate.<sup>22</sup> This not only mimics the chemotactic escape of a living swimming object from toxins or its attraction by nutrient gradients<sup>23–27</sup> but is also important to steer the directed motion of swimmers for specific applications such as targeted drug delivery<sup>28</sup> and nanorobotics.<sup>29</sup> Various kinds of motility fields have recently been considered including constant gradients,<sup>30,31</sup> stepwise profiles,<sup>32,33</sup> and ratchets,<sup>34,35</sup> as well as time-dependent motility fields.<sup>36–39</sup> In particular, the tunability of the colloid motility by light<sup>9–14,40–42</sup> provides the opportunity to impose almost arbitrary laser-optical motility fields. When the prescribed light intensity is proportional to the local motility, a particle will get dynamically trapped in the dark spots where its motility is low.<sup>32,33,43</sup>

Here we explore a repulsively interacting binary mixture of small self-propelled spherical colloidal particles doped with large ones. The binary mixture of self-propelled colloids is confined to a two-dimensional substrate in a static periodic triangular-like light intensity field. The motility of the particles is proportional to the imposed light intensity, but the prefactor depends on the species. In line with previous experimental findings, the light-activated particles also experience a torque aligning their motion towards the direction of the negative intensity gradient, i.e., swimmers exhibit negative phototaxis.<sup>35</sup> This strongly favors the dynamical trapping effect near motility minima. Using Brownian dynamics computer simulations, we find indeed a demixing of the active particles mixture, where typically one species of particles is close to the minimum and the other is centered around in an outer shell. In the limit of very strong aligning torque, we demonstrate that an exact mapping of the nonequilibrium system onto an equilibrium system is possible. This equilibrium system involves an effective external potential that is minimal at the intensity minima. The external potential is piecewise parabolic around the intensity minima. Therefore, it can be understood as an external gravitational potential, where the gravity force depends on the height. Using this analogy, one can define an effective “heaviness” of the self-propelled particles. Thereby, there is an important link between motility fields of active colloids and equilibrium sedimentation of passive colloids where a lot of theoretical<sup>44–48</sup> and experimental knowledge<sup>49–53</sup> exists, see Ref. 54 for a review. In analogy to shaken granular matter in gravity<sup>55–60</sup> and to the sedimentation of colloidal mixtures,<sup>61–67</sup> we define a “colloidal Brazil nut effect (BNE)” if the heavier particles are floating on top of the lighter ones. We identify system parameters for the colloidal Brazil nut effect to occur and explain it based on a generalized Archimedes’ principle<sup>68</sup> within the effective equilibrium model: heavy particles are levitated in a dense fluid of lighter particles if their effective mass density is lower than that of the surrounding fluid. As an aside, another application of the Archimedes’ principle has been recently applied to the lift of passive particles in an active bath.<sup>69</sup>

We also perform real-space tracking experiments on light-activated colloidal mixtures. The experimental results agree quantitatively with the simulation predictions.

The paper is organized as follows: in Sec. II, we introduce the theoretical model, define the colloidal Brazil nut effect, and propose a simple depletion bubble picture to predict the basic physics. Our experiments are described in Sec. III. Results from both theory and experiment are presented in Sec. IV. Finally, we conclude in Sec. V.

## II. THEORY

### A. Active Brownian particle model

We consider an active Brownian particle model for a mixture of big and small spheres moving in the two-dimensional  $xy$ -plane at temperature  $T$ . The particles have a diameter  $\sigma_\alpha$ , where  $\alpha = b, s$  (for big and small particles) is a species index. The self-propulsion speed of the particles  $v_\alpha(x)$  depends on their position and is periodic in the  $x$ -coordinate with a

characteristic spacing  $l_v$ , but independent of the  $y$ -coordinate. Having a light motility landscape in mind,<sup>35</sup> we assume the same function for both types of particles except for a different prefactor. In detail, we assume a triangular velocity profile (see Fig. 1), for which in one period

$$v_\alpha(x) = 2|x|V_\alpha^{\max}/l_v \quad \text{for } |x| \leq l_v/2, \quad (1)$$

where  $V_\alpha^{\max}$  indicates the maximum propulsion velocity of species  $\alpha$ . We consider a large field with several of such velocity grooves, which accommodates  $N_\alpha$  particles of species  $\alpha$  ( $\alpha = b, s$ ). The system is considered in a rectangular box of edge lengths  $L_x$  and  $L_y$  with periodic boundary conditions in both directions. Then the partial system densities can either be described by areal densities  $\rho_\alpha^{(a)} = N_\alpha/(L_x L_y)$  or line densities per wedge  $\rho_\alpha = \rho_\alpha^{(a)} l_v$ .

The direction of the self-propulsion velocity defines an internal particle orientation degree of freedom which is described by the angle  $\varphi$  between the velocity and the  $x$ -axis. In addition, there is a torque aligning the particle orientation along the negative gradient of the motility field, which leads to an angular velocity  $\omega_\alpha$ . Note that, in a homogeneous motility field, where  $v_\alpha(x)$  is constant, this angular velocity obviously vanishes. In general, following our modeling in a previous study,<sup>35</sup> the angular velocity  $\omega_\alpha(\varphi, x)$  also depends on the  $x$  coordinate via

$$\omega_\alpha(\varphi, x) = \frac{c}{\sigma_\alpha} v_\alpha(x) v'_\alpha(x) \sin(\varphi), \quad (2)$$

where  $v'_\alpha(x) = \frac{dv_\alpha(x)}{dx}$  denotes the velocity gradient and  $c$  is a common prefactor. Moreover, it was shown<sup>35</sup> that the magnitude of the angular velocity scales with the inverse of the particle diameter.

The particles interact via a short-ranged repulsive Weeks-Chandler-Andersen (WCA) pair potential<sup>70</sup>

$$u_{\alpha\beta}(r) = \begin{cases} u_{\alpha\beta}^{\text{LJ}}(r) - u_{\alpha\beta}^{\text{LJ}}(R_\alpha + R_\beta) & r \leq \frac{\sigma_\alpha + \sigma_\beta}{2}, \\ 0 & r > \frac{\sigma_\alpha + \sigma_\beta}{2}, \end{cases} \quad (3)$$

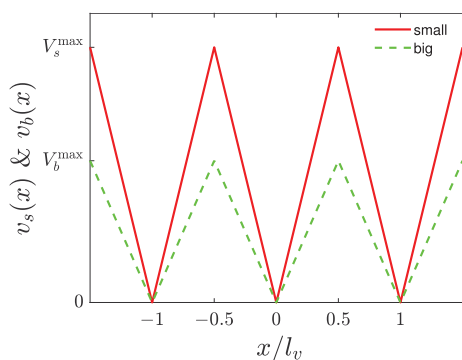


FIG. 1. Schematic view of the propulsion velocity as a function of  $x/l_v$  for the two different particle species as originating from a triangular-like light intensity field.

where  $r$  is the interparticle distance,  $u_{\alpha\beta}^{LJ}(r) = 4\epsilon[(\sigma_{\alpha\beta}/r)^{12} - (\sigma_{\alpha\beta}/r)^6]$  is the Lennard-Jones potential, and the additive repulsion diameters are  $\sigma_{\alpha\beta} = 2^{-1/6}(\sigma_\alpha + \sigma_\beta)$  ( $\alpha, \beta \in \{s, b\}$ ). The repulsion strength  $\epsilon$  is fixed to  $100k_B T$ , where  $k_B T$  is the (effective) thermal energy.

We describe the center-of-mass positions of the particles with

$$\mathbf{r}_{\alpha,k}(t) = (x_{\alpha,k}(t), y_{\alpha,k}(t)) \quad (4)$$

and their orientations by the unit vectors

$$\hat{\mathbf{u}}_{\alpha,k} = (\cos(\varphi_{\alpha,k}), \sin(\varphi_{\alpha,k})), \quad (5)$$

where  $\varphi_{\alpha,k}$  are the orientational angles. Here,  $k \in \{1, N_\alpha\}$  labels the particles of the same species.

In the active Brownian model, the equations of motion for the translational and orientational degrees of freedom are coupled overdamped Langevin equations with stochastic noise. In detail, the translational motion of the  $k$ th particle of species  $\alpha$  is governed by

$$\frac{d}{dt}\mathbf{r}_{\alpha,k} = v_\alpha(x_{\alpha,k})\hat{\mathbf{u}}_{\alpha,k} + \frac{1}{\gamma_\alpha}\mathbf{F}_{\alpha,k}^{\text{int}} + \sqrt{2\frac{k_B T}{\gamma_\alpha}}\boldsymbol{\xi}_{\alpha,k}(t). \quad (6)$$

Here, the pairwise repulsive interaction force  $\mathbf{F}_{\alpha,k}^{\text{int}}$  is obtained from

$$\mathbf{F}_{\alpha,k}^{\text{int}} = -\nabla_{\mathbf{r}_{\alpha,k}} \sum_{\beta=b,s} \sum_{i=1}^{N_\beta'} u_{\alpha,\beta}(|\mathbf{r}_{\beta,i} - \mathbf{r}_{\alpha,k}|). \quad (7)$$

The prime symbol indicates the exclusion of the self-interaction, i.e., if  $\beta = \alpha$ , then  $i$  cannot take the value  $k$ .

The rotational motion of the  $k$ th particle of species  $\alpha$  is governed by

$$\frac{d}{dt}\varphi_{\alpha,k}(t) = \omega_\alpha(\varphi_{\alpha,k}, x_{\alpha,k}) + \sqrt{2\frac{k_B T}{\gamma_\alpha^r}}\xi_{\alpha,k}^\varphi(t). \quad (8)$$

$\xi_{\alpha,k}(t) = (\xi_{\alpha,k}^x(t), \xi_{\alpha,k}^y(t))$  and  $\xi_{\alpha,k}^\varphi(t)$  describe zero-mean Markovian white noise, with the variance

$$\langle \xi_{\alpha,k}(t) \otimes \xi_{\alpha',k'}(t') \rangle = \delta(t-t')\delta_{\alpha\alpha'}\delta_{kk'}\mathbf{1} \quad (9)$$

and

$$\langle \xi_{\alpha,k}^\varphi(t) \xi_{\alpha',k'}^\varphi(t') \rangle = \delta(t-t')\delta_{\alpha\alpha'}\delta_{kk'}, \quad (10)$$

where  $\langle \dots \rangle$  indicates a noise average,  $\otimes$  denotes the dyadic product, and  $\mathbf{1}$  is the unit matrix. For species  $\alpha$ , the translational and rotational friction coefficients are represented by  $\gamma_\alpha$  and  $\gamma_\alpha^r$ , respectively. We neglect hydrodynamic interactions between particles.<sup>71</sup>

For spherical particles with a hydrodynamic diameter  $\sigma_\alpha$ , the friction coefficients are given by  $\gamma_\alpha = 3\pi\eta\sigma_\alpha$  and  $\gamma_\alpha^r = \pi\eta\sigma_\alpha^3$ , where  $\eta$  is the viscosity of the medium. The respective short-time translational and rotational diffusion coefficients  $D_\alpha$  and  $D_\alpha^r$  are characterized by the corresponding friction coefficients such that

$$D_\alpha = k_B T / \gamma_\alpha \quad (11)$$

and

$$D_\alpha^r = k_B T / \gamma_\alpha^r. \quad (12)$$

Thus, for spherical particles,  $D_\alpha$  and  $D_\alpha^r$  fulfill

$$D_\alpha / D_\alpha^r = \sigma_\alpha^2 / 3 \quad (13)$$

when in equilibrium ( $v_\alpha = 0$ ).

In our active Brownian model, particles will localize where the self-propulsion velocity is zero, i.e., around  $x = nl_v$  with an integer  $n$ . There are two reasons for that: first of all, a vanishing mobility implies a larger resting time. Consequently, even for  $c = 0$ , the probability density of an ideal non-fluctuating particle will scale as  $1/v_\alpha(x)$ . Fluctuations will lead to an algebraic decay with distance  $x$  (when  $l_v \rightarrow \infty$ ).<sup>72</sup> Second, and much more importantly here, for  $c > 0$ , there is an aligning torque that rotates the particles back such that they travel back to the intensity minimum. The second effect yields exponential localization of an ideal particle in the groove as a function of  $x$  when  $l_v \rightarrow \infty$ .

## B. Effective equilibrium model

In the experiments, the aligning torque towards the negative gradient of the velocity field is strong<sup>35</sup> relative to the rotational noise. In this limit, formally achieved by very large prefactors  $c$  in Eq. (2), one can neglect the stochastic term in Eq. (8). Then, for all particles, the orientation is fixed along the  $x$ -axis such that in one period

$$\phi_{\alpha,k}(x_{\alpha,k}) = \begin{cases} \pi & 0 < x_{\alpha,k} < \frac{l_v}{2}, \\ 0 & -\frac{l_v}{2} < x_{\alpha,k} < 0, \end{cases} \quad (14)$$

since misalignments are quickly oriented back. This implies that the self-propulsion velocity in the translational Langevin equation (6) is directed along the  $x$ -axis and the resulting term can be derived as a gradient from a “potential” function. This means that the equations of motion in this limit can be written as

$$\frac{d}{dt}\mathbf{r}_{\alpha,k} = \frac{1}{\gamma_\alpha}(\mathbf{F}_\alpha^{\text{ext}}(x_{\alpha,k}) + \mathbf{F}_{\alpha,k}^{\text{int}}) + \sqrt{2\frac{k_B T}{\gamma_\alpha}}\boldsymbol{\xi}_{\alpha,k}(t), \quad (15)$$

where the external force  $\mathbf{F}_\alpha^{\text{ext}}(x)$  is a gradient of a potential energy  $U_\alpha(x)$ ,

$$\mathbf{F}_\alpha^{\text{ext}}(x) = -\frac{d}{dx}U_\alpha(x)\hat{\mathbf{e}}_x. \quad (16)$$

The equations of motion (15) describe ordinary Brownian particles—with translational coordinates only—in *equilibrium* and define our *effective equilibrium model*. In general, in analogy to the velocity profile of the active mixture defined via Eq. (1),  $U_\alpha(x)$  is periodic in  $x$  with periodicity length  $l_v$  and is piecewise parabolic, see Fig. 2. In one period, it is given by

$$U_\alpha^{\text{ext}}(x) = -\gamma_\alpha \int_0^x dx' v(x') = -2V_\alpha^{\text{max}} \frac{\gamma_\alpha}{l_v} \int_0^x dx' |x'| \\ = V_\alpha^{\text{max}} \frac{\gamma_\alpha}{l_v} x^2 \quad \text{for } |x| \leq l_v/2. \quad (17)$$

In this equilibrium model, particles would clearly accumulate in the minimum of the potential energy, e.g., around

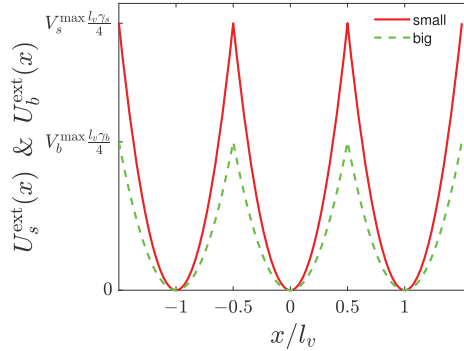


FIG. 2. Schematic view of the external potential applied to the particles in the effective equilibrium model as a function of  $x/l_v$ .

$x = 0$ , in qualitative agreement with the active Brownian particle model.

### C. Definition of the colloidal Brazil nut effect

The Brazil nut effect (BNE) is directly connected to the space-dependent accumulation around the motility minima in the steady state. Information about particle distributions is contained in the inhomogeneous one-particle density profiles in the resulting steady state. For a system homogeneous in the  $y$ -direction, the corresponding density profiles only depend on  $x$  and are  $l_v$ -periodic non-negative functions. In analogy to equilibrium systems,<sup>73</sup> we hence define line-density profiles

$$\rho_\alpha(x) = \left\langle \sum_{i=1}^{N_\alpha} \delta(x - x_{\alpha,i}) \right\rangle. \quad (18)$$

Here, the brackets  $\langle \dots \rangle$  denote a steady state average and become a traditional canonical average in equilibrium (for  $v_\alpha(x) \equiv 0$ , respectively, in the effective equilibrium model).

In order to characterize the Brazil nut effect, we define a spatial extension (or a width)  $h_\alpha$  of the line-density profile in one groove by considering the normalized second moment

$$h_\alpha = \sqrt{\frac{\int_{-l_v/2}^{l_v/2} dx x^2 \rho_\alpha(x)}{\int_{-l_v/2}^{l_v/2} dx \rho_\alpha(x)}}. \quad (19)$$

For sedimentation, this would correspond to an averaged sedimentation height of species  $\alpha$ .

The effective equilibrium model now helps to define a “heaviness” of the particle species. The prefactor  $\gamma_\alpha V_\alpha^{\max}$   $\sim \sigma_\alpha V_\alpha^{\max}$  in Eq. (17) for the potential energy corresponds to effective heaviness. Therefore, we define that the big particles are “heavier” than the small ones if the following condition is fulfilled:

$$\sigma_b V_b^{\max} > \sigma_s V_s^{\max}, \quad (20)$$

while obviously in the opposite case the smaller particles are heavier than the bigger ones. By definition, a Brazil nut effect occurs if the heavier particles are on top of the lighter ones, i.e., if the height of the heavier particles is larger than the height of the lighter particles. Clearly, there are three possibilities for that:

1. The bigger particles are heavier than the smaller ones, i.e.,  $\sigma_b V_b^{\max} > \sigma_s V_s^{\max}$ . Then a BNE occurs if  $h_b > h_s$ . We call this situation BNE<sup>(1)</sup>. Conversely, if  $h_b < h_s$ , there is a state with the reverse effect, which we refer to as reverse BNE<sup>(1)</sup>.
2. The smaller particles are heavier than the bigger ones, i.e.,  $\sigma_s V_s^{\max} > \sigma_b V_b^{\max}$ . Then a BNE occurs if  $h_s > h_b$ , this situation is referred to as BNE<sup>(2)</sup>. Conversely, if  $h_s < h_b$ , there is a reverse BNE referred to as reverse BNE<sup>(2)</sup>.
3. The special case when  $h_s = h_b$  is termed no BNE.

In conclusion, we have classified the system within a scheme of five possible states: BNE<sup>(1)</sup>, reverse BNE<sup>(1)</sup>, BNE<sup>(2)</sup>, reverse BNE<sup>(2)</sup>, and no BNE. Two of these states correspond to a Brazil nut effect where the heavier particles float on the lighter ones. We remark that in the sequel, gravity in our two dimensional system is directed along the  $x$ -direction (not along the conventional  $y$ -direction). So, floating on the top means an outermost layer along the  $y$ -direction.

### D. Depletion bubble picture

We now provide a minimal theory that describes the physics driving the colloidal BNE in terms of a generalized Archimedes’ law. This approach is based on the effective equilibrium model and was discussed in the context of sedimenting colloidal mixtures in Ref. 68. When a big particle excludes small particles, it creates a bubble or a cavity depleted by small particles. This “depletion” bubble is attached to the big particle and effectively provides a buoyant force which lifts the big particle. For the sake of simplicity, let us assume that the density field of the small particles around the groove is piecewise constant, i.e., there is a block of fluid at (areal) density  $\bar{\rho}_s$  (see Fig. 3).

When a big particle is embedded into this active fluid at a distance  $x_b$  from the origin, it will create an encircling depletion bubble of radius  $R_d = (\sigma_b + \sigma_s)/2$  due to the repulsive interactions. This bubble is attached to the big particles. According to the effective equilibrium model, one can locally apply Archimedes’ principle such that the big particle experiences a buoyant lift force  $F_b^{\text{buoy}}$  given by

$$F_b^{\text{buoy}}(x_b) = \pi R_d^2 \bar{\rho}_s F_s^{\text{ext}}(x_b), \quad (21)$$

where, from Eq. (16),

$$F_s^{\text{ext}}(x_b) = -2V_s^{\max} \frac{\gamma_s}{l_v} |x_b| \quad \text{for } |x_b| \leq l_v/2. \quad (22)$$

If the buoyant lift force dominates the inward effective force [see Eq. (16) again], i.e., if

$$F_b^{\text{ext}}(x_b) < F_b^{\text{buoy}}(x_b) \quad (23)$$



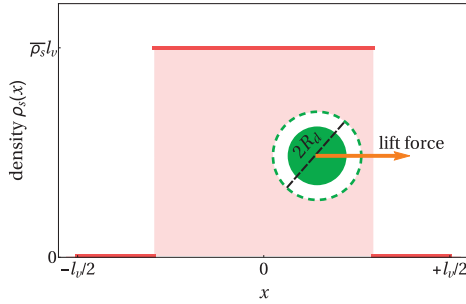


**FIG. 3.** Schematic picture of the depletion bubble mechanism. Small particles are considered to be uniformly distributed in a fluid block of constant density  $\bar{\rho}_s$ . When a big particle delves into this fluid, it will create a depletion bubble of radius  $R_d = (\sigma_b + \sigma_s)/2$ . This will result in an equilibrium buoyant force according to Archimedes' principle.

is fulfilled, the big particles are expelled from the central area of the grooves by the small ones. Obviously, the dependence on  $x_b$  drops out in Eq. (23) such that the condition can be rewritten as

$$\frac{V_b^{\max}}{V_s^{\max}} \lesssim \pi \bar{\rho}_s \left( \frac{\sigma_b + \sigma_s}{2} \right)^2 \frac{\sigma_s}{\sigma_b}. \quad (24)$$

Combined with our previous classification of the Brazil nut effect, for a given particle heaviness, this approach makes explicit predictions about whether the state BNE<sup>(1)</sup> occurs or not. However, it requires an input for  $\bar{\rho}_s$  from simulations and is therefore not fully microscopic. Moreover, this approach only works in the case that the big particles are much more diluted than the small ones.

We finish with two remarks: first of all, correlations will lead to density oscillations in the density profile of the small particles around the big one as discussed in Ref. 74. Second, the converse situation BNE<sup>(2)</sup>, where a heavy small particle is floating on a sea of big particles, is also conceivable. This would result from a strongly non-additive large radius  $R_d$ . A similar depletion bubble picture can be established in this case by interchanging the species indices  $b$  and  $s$  which we shall, however, not consider further in detail. For more details to the BNE<sup>(2)</sup> state, we refer to previous studies on passive colloids.<sup>74,75</sup>

### E. Brownian dynamics simulations

We have solved the equations of motion for the active Brownian model and the effective equilibrium model by using Brownian dynamics computer simulations. In detail,  $N_b = 14$  big and  $N_s = 2068$  small particles were simulated in a periodic square simulation box with size  $L_x = L_y = 102\sigma_s$ , which contained 3 complete periods of the motility field, at room temperature. The partial line densities per wedge,  $\rho_\alpha$ , are thus given by  $\rho_s = 6.76\sigma_s^{-1}$  and  $\rho_b = 0.046\sigma_s^{-1}$ . In terms of a typical Brownian time  $\tau = \sigma_s^2/D_s$ , the time step  $\Delta t$  was chosen to be  $\Delta t = 10^{-5}\tau$ . The initial configuration was an ideal gas, and the

system was equilibrated for an initial time of about  $60\tau$ . Statistics for the density profiles was gathered during an additional subsequent time window of typically  $200\tau$ .

In line with the experiments, the maximum velocity of the small particles was fixed at  $V_s^{\max} = 34.5\sigma_s/\tau$  and the prefactor  $c$  was chosen to be  $c = 0.6\tau$ .<sup>35</sup> The simulation results are obtained for different diameter ratios, where  $\sigma_s$  has been kept fixed. For each diameter ratio, the maximum velocity of the big particles was varied from  $V_b^{\max} = 0.25V_s^{\max}$  to  $V_b^{\max} = 3V_s^{\max}$  with steps of  $0.25V_s^{\max}$ . Then, for every value of  $V_b^{\max}/V_s^{\max}$ , the occurrence of BNE or reverse BNE has been investigated.

### III. EXPERIMENTS

We experimentally studied concentrated active colloidal mixtures with different size ratios. As small active particles, we used silica spheres of diameter  $\sigma_s = 2.7\mu\text{m}$  half-capped with a carbon layer of thickness  $d = 20\text{nm}$ . We doped the active suspension with a few large active colloids of diameters  $\sigma_b = 13\mu\text{m}$ ,  $7.75\mu\text{m}$ , and  $4.96\mu\text{m}$ , respectively, while keeping the diameter of small spheres constant. The partial line densities per wedge were approximately  $\rho_s = 2.6\mu\text{m}^{-1}$  and  $\rho_b = 0.027\mu\text{m}^{-1}$  for small and big particles, which are comparable to the line densities used in the simulation ( $\rho_s = 2.5\mu\text{m}^{-1}$  and  $\rho_b = 0.017\mu\text{m}^{-1}$ ), respectively.

The colloids were suspended in a critical mixture of water and 2,6-lutidine (lutidine mass fraction 0.286), whose lower critical point is at  $T_c = 34.1^\circ\text{C}$ . When the solution is kept well below this value, the capped colloids perform an entire diffusive Brownian motion. Upon laser illumination (at wavelength  $\lambda = 532\text{nm}$ ), which is only absorbed by the particle's cap, the solvent locally demixes, and then persistent particle motion is achieved with a constant swimming velocity  $v$  which linearly depends on the incident laser intensity.<sup>9,10</sup> For a given cap thickness, independent of the size of the active particles, the same linear dependence  $v \propto I$  is observed. Since the propulsion velocity  $v$  depends on the absorbed intensity across the particle's cap, the speed can be varied by the cap thickness with the linear dependence  $v \propto Id$ .<sup>76</sup>

To vary the propulsion velocity in mixtures of big and small particles, our experiments were performed with three different carbon cap thicknesses of the big particles:  $d = 5\text{nm}$ ,  $20\text{nm}$ , and  $30\text{nm}$ . Under our experimental conditions, the maximum velocity of the small species was fixed at  $V_s^{\max} = 1\mu\text{m/s}$ . For the big species,  $V_b^{\max}$  was varied as follows:  $V_b^{\max} = 0.25\mu\text{m/s}$ ,  $1\mu\text{m/s}$ , and  $1.5\mu\text{m/s}$ . The experiments for each combination of big and small particles were repeated between 5 and 20 times to yield good statistical averages.

Periodic triangle-like light patterns were created by a laser line focus being scanned across the sample plane with a frequency of 200 Hz. Synchronization of the scanning motion with the input voltage of an electro-optical modulator leads to a quasi-static illumination landscape.<sup>35</sup> Particle positions and orientations were obtained by digital video microscopy with a frame rate of 13 fps. The particle orientation was determined directly from the optical contrast due to the carbon cap.<sup>77</sup> To be more precise, because of the optical contrast between

the dark carbon cap and the transparent silica, the angular coordinate  $\varphi$  of the active particle can be obtained from the vector connecting the particle center and the intensity centroid of the particle image. The error of this detection is less than 5% as confirmed by comparison with stuck particles whose orientation can be precisely varied using a rotational stage.

#### IV. RESULTS

Figure 4 summarizes our main findings in the  $(V_b^{\max}/V_s^{\max}, \sigma_b/\sigma_s)$  parameter space of the motility and size ratio of the mixture. The results are shown for (a) the experiment, (b) the active mixture model, (c) the effective equilibrium model, and (d) the depletion bubble picture. For the considered parameter span, three different states, namely, reverse BNE<sup>(2)</sup>, BNE<sup>(1)</sup>, and reverse BNE<sup>(1)</sup>, were identified (plus the trivial special case of the no BNE state), see the legend with the different symbols in Fig. 4(a). Remarkably, the topology of the state diagram is the same in Figs. 4(a)–4(d) and there is a quantitative agreement between experiment and theory. As compared to the active mixture model [shown in Fig. 4(b)], the equilibrium model shows qualitative but not full quantitative agreement. Moreover, the simple depletion bubble pictures are in line with the equilibrium model.

As expected, the reverse BNE<sup>(2)</sup> state is favored when  $V_b^{\max}/V_s^{\max}$  is small (i.e., small particles are heavier). When both species are equally heavy, the crossover from the reverse BNE<sup>(2)</sup> to the BNE<sup>(1)</sup> state takes place, as expressed by the condition  $\sigma_b V_b^{\max} = \sigma_s V_s^{\max}$ , which is shown as the olive green reference line in Figs. 4(a)–4(d). In the BNE<sup>(1)</sup> state, the big particles are heavier but float on the interface. Increasing  $V_b^{\max}/V_s^{\max}$  further leads ultimately to the reverse BNE<sup>(1)</sup>, as the big particles are getting too heavy to be lifted by the depletion bubble and sink to the motility minima. Hence, as the motility asymmetry  $V_b^{\max}/V_s^{\max}$  is increased, the state sequence

$$\text{reverse BNE}^{(2)} \rightarrow \text{BNE}^{(1)} \rightarrow \text{reverse BNE}^{(1)}$$

is observed. This sequence is reproduced in all of our 4 approaches considered in Figs. 4(a)–4(d).

Let us now comment on the comparison between the active mixture and the equilibrium model. The widening of the stability region of the BNE<sup>(1)</sup> state in the equilibrium model can be qualitatively understood in terms of the aligning torque which is strongest in the equilibrium model. If the aligning torque is weakened, the demixing is expected to get weaker, favoring the standard reverse BNE<sup>(1)</sup> case relative to the BNE<sup>(1)</sup> state. This is indeed observed when comparing Figs. 4(b) and 4(c).

The value of  $V_b^{\max}/V_s^{\max}$ , where the threshold for the crossover from BNE<sup>(1)</sup> to reverse BNE<sup>(1)</sup> happens, grows monotonically with  $\sigma_b/\sigma_s$ . This can be explained qualitatively within the depletion bubble picture via the generalized Archimedes' law. Assuming that the size  $\sigma_s$  and the areal density  $\bar{\rho}_s$  of the small species are fixed, the number of small

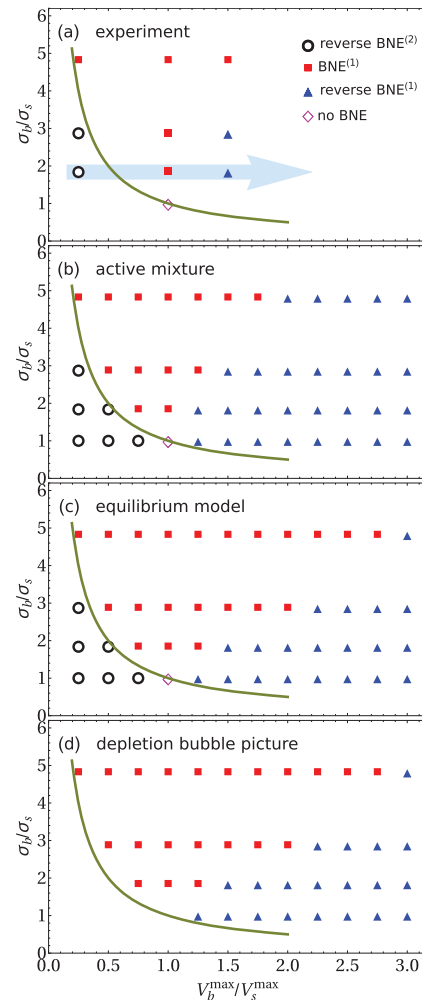


**FIG. 4.** Occurrence of the Brazil nut effect (BNE) in the parameter space spanned by the motility ratio  $V_b^{\max}/V_s^{\max}$  and the size ratio  $\sigma_b/\sigma_s$  of the binary mixture. Results are shown for (a) experiment, (b) the active mixture model, (c) the effective equilibrium model, and (d) the depletion bubble picture. The olive green curve indicates the boundary when  $F_b^{\text{eff}} = F_s^{\text{eff}}$ . Data are presented for four diameter ratios:  $\sigma_b/\sigma_s = 1, 1.84, 2.87$ , and  $4.82$  at fixed  $\sigma_s$ . More detailed results are shown in Fig. 5 for the three parameter combinations highlighted by the light blue arrow in (a).

particles excluded by a big one grows by increasing the diameter ratio  $\sigma_b/\sigma_s$ , which results in a stronger buoyant lift force. Based on Eq. (24), the crossover from BNE<sup>(1)</sup> to reverse BNE<sup>(1)</sup>

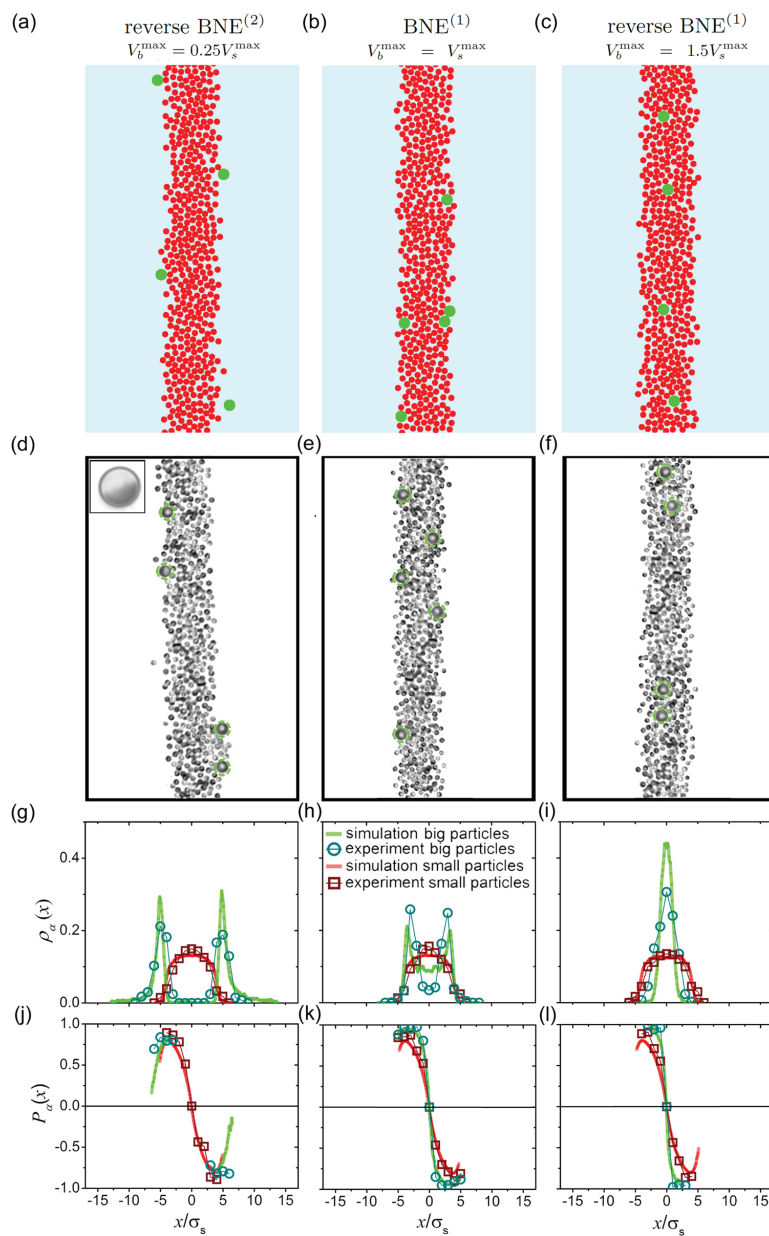


**FIG. 5.** Comparison of experiment and simulation: (a)–(c) simulation snapshots, (d)–(f) experimental snapshots, (g)–(i) line-density profiles  $\rho_\alpha(x)$  [defined via Eq. (18)], and (j)–(l) polarizations  $P_\alpha(x)$  [introduced in Eq. (26)]. The results are shown for the reverse BNE<sup>(2)</sup> with  $V_b^{\max} = 0.25V_s^{\max}$  (first column), the BNE<sup>(1)</sup> state with  $V_b^{\max} = V_s^{\max}$  (second column), and the reverse BNE<sup>(1)</sup> with  $V_b^{\max} = 1.5V_s^{\max}$  (third column). The size ratio is kept constant at  $\sigma_b/\sigma_s = 1.84$ . Since gravity in our 2D system is along the  $x$ -direction, floating on the top occurs along the  $y$ -direction. The inset of (d) shows the microscope picture of a single active particle.

is roughly governed by

$$\frac{V_b^{\max}}{V_s^{\max}} \approx \frac{\pi}{4} \tilde{\rho}_s \sigma_s^2 \left( \frac{1}{\sigma_b/\sigma_s} + 1 \right)^2 \frac{\sigma_b}{\sigma_s}. \quad (25)$$

The right hand side of Eq. (25) is an increasing function in  $\sigma_b/\sigma_s$  (for  $\sigma_b/\sigma_s \geq 1$ ). This implies that the crossover from BNE<sup>(1)</sup> to reverse BNE<sup>(1)</sup> occurs at larger  $V_b^{\max}/V_s^{\max}$  if the diameter ratio  $\sigma_b/\sigma_s$  is increased. Note that this consideration does not capture the situations on the left hand side of the olive green curve in the parameter space, where the big particles are lighter than the small ones, since the depletion bubble picture does not hold here. Finally, we remark that we never observe a BNE<sup>(2)</sup> state for the parameters considered here. However, this state is expected to occur in principle in a strongly non-additive binary mixture.

Simulation and experimental snapshots together with averaged partial density and polarization profiles are summarized in Fig. 5 for the three states: reverse BNE<sup>(2)</sup>, BNE<sup>(1)</sup>, and reverse BNE<sup>(1)</sup> at fixed size asymmetry and increasing motility asymmetry  $V_b^{\max}/V_s^{\max}$ . The associated path of parameters is marked by a light blue arrow in Fig. 4(a). The snapshots clearly indicate whether the big particles are floating on the layer of small particles or are confined to the motility minima and therefore directly reveal the different states. The partial line-density profiles  $\rho_\alpha(x)$  [defined in Eq. (18)] reveal a remarkable quantitative agreement between experiment and simulation in all three states, see Figs. 5(g)–5(i). Most of the deviations are within the statistical errors, and small systematic deviations may be attributed to polydispersity and hydrodynamic interactions which are neglected in our model.

Finally, we show polarization profiles in Figs. 5(j)–5(l). For a one-component active system under conventional gravity, polarization effects have been studied in theory<sup>78,79</sup> and experiments.<sup>80</sup> Likewise, we define the partial polarization profiles here as

$$P_\alpha(x) = \frac{\left\langle \sum_{i=1}^{N_\alpha} \cos(\varphi_{\alpha,i}) \delta(x - x_{\alpha,i}) \right\rangle}{\rho_\alpha(x)}. \quad (26)$$

Clearly, the polarization is strongly affected by the aligning torque. When a particle crosses the motility minimum from left to right (respectively, right to left), the torque quickly changes its orientation by 180°. In the ideal case of instantaneous orientational flips as embodied in the effective equilibrium model, the polarization profile would exhibit a sharp kink-like sign function  $\text{sgn}(x)$ . A finite torque will lead to a smearing of this sign-function, where at the motility minima  $P_\alpha(x=0) = 0$  vanishes due to symmetry. If one particle species floats on top of a fluid of the other species, there is a non-monotonicity in the polarization, which is well-pronounced for the big particles in Fig. 5(j) and for the small particles in Fig. 5(l). This peak in  $P_\alpha(x)$  roughly corresponds to the outermost particle layering and has its physical origin in the fact that active particles near repulsive walls show a polarization peak in general.<sup>81,82</sup> Clearly, the stronger the motility, the sharper the polarization profiles. Again there is a very good agreement between experiment and simulation, supporting earlier findings that the used propulsion mechanism employed

in our experiments remains largely unaffected by the presence of other nearby particles.<sup>41,76</sup>

## V. CONCLUSIONS

We have presented a systematic study of demixing (or segregation) in binary mixtures of active particles moving on a motility contrast landscape by comparing theory, computer simulations, and experiments. Our findings are based on the strong orientational response of the active particles towards the local minima, which depends on their size and velocity.<sup>35</sup> We have shown that the colloidal Brazil nut effect, well established for sedimenting mixtures of passive colloids in the presence of gravity,<sup>68</sup> can also be achieved in mixtures of active colloids being exposed to an inhomogeneous motility field. We define a Brazil nut effect as a situation where the particles of the heavier species are floating on the lighter ones. Thus, “heaviness” is defined by their coupling to the motility contrast. Within this viewpoint, we have considered different parameter combinations for the size and motility asymmetry and, then, mapped out the BNE occurrence.

We remark that, while active systems consisting of one particle species have been extensively studied in gravitational fields<sup>8,42,83,84</sup> (see also Refs. 85 and 86 for other aspects of gravity), there are no studies on dense active mixtures under nonuniform motility fields so far. Our theoretical approach can be flexibly applied to other active mixtures regardless of the details of the static external field. This is demonstrated by mapping our active system onto an equilibrium one with a static effective external potential.

Our qualitative findings can also be exploited for applications. In particular, different kinds of active particles (see Refs. 87–90 for recent studies) can be separated and sorted. This is of particular importance since an inhomogeneous motility field (e.g., an external light gradient) can be better controlled than gravity. Moreover, in contrast to dynamical separation phenomena (e.g., in ratchets<sup>22</sup>), the separation procedure proposed here is static in the steady state such that the uppermost layer of floating particles can be removed more easily. Extensions to ternary mixtures are straight-forward and will be considered in future work, where understanding such demixing structures is a prerequisite to create novel materials through active phase separation and self-assembly.

## ACKNOWLEDGMENTS

H.L. and C.B. acknowledge funding from the SPP 1726 of the Deutsche Forschungsgemeinschaft (DFG, German Research Foundation); C.B. by the ERC Advanced Grant ASCIR (Grant No. 693683). B.t.H. gratefully acknowledges financial support through a Postdoctoral Research Fellowship from the Deutsche Forschungsgemeinschaft—HA 8020/1-1.

## REFERENCES

- <sup>1</sup>P. Romanczuk, M. Bär, W. Ebeling, B. Lindner, and L. Schimansky-Geier, *Eur. Phys. J. Spec. Top.* **202**, 1 (2012).
- <sup>2</sup>J. Elgeti, R. G. Winkler, and G. Gompfer, *Rep. Prog. Phys.* **78**, 056601 (2015).
- <sup>3</sup>M. E. Cates, *Rep. Prog. Phys.* **75**, 042601 (2012).

- <sup>4</sup>C. Bechinger, R. Di Leonardo, H. Löwen, C. Reichhardt, G. Volpe, and G. Volpe, *Rev. Mod. Phys.* **88**, 045006 (2016).
- <sup>5</sup>A. Zöttl and H. Stark, *J. Phys.: Condens. Matter* **28**, 253001 (2016).
- <sup>6</sup>G. Gompper, C. Bechinger, S. Herminghaus, R. Isele-Holder, U. B. Kaupp, H. Löwen, H. Stark, and R. G. Winkler, *Eur. Phys. J. Spec. Top.* **225**, 2061 (2016).
- <sup>7</sup>W. F. Paxton, K. C. Kistler, C. C. Olmeda, A. Sen, S. K. St. Angelo, Y. Cao, T. E. Mallouk, P. E. Lammert, and V. H. Crespi, *J. Am. Chem. Soc.* **126**, 13424 (2004).
- <sup>8</sup>J. Palacci, C. Cottin-Bizonne, C. Ybert, and L. Bocquet, *Phys. Rev. Lett.* **105**, 088304 (2010).
- <sup>9</sup>G. Volpe, I. Buttinoni, D. Vogt, H.-J. Kümmerer, and C. Bechinger, *Soft Matter* **7**, 8810 (2011).
- <sup>10</sup>I. Buttinoni, G. Volpe, F. Kümmel, G. Volpe, and C. Bechinger, *J. Phys.: Condens. Matter* **24**, 284129 (2012).
- <sup>11</sup>J. Palacci, S. Sacanna, A. Vatchinsky, P. M. Chaikin, and D. J. Pine, *J. Am. Chem. Soc.* **135**, 15978 (2013).
- <sup>12</sup>J. Palacci, S. Sacanna, A. Preska Steinberg, D. J. Pine, and P. M. Chaikin, *Science* **339**, 936 (2013).
- <sup>13</sup>J. Palacci, S. Sacanna, S.-H. Kim, G.-R. Yi, D. J. Pine, and P. M. Chaikin, *Phil. Trans. R. Soc. A* **372**, 20130372 (2014).
- <sup>14</sup>H. Moyses, J. Palacci, S. Sacanna, and D. G. Grier, *Soft Matter* **12**, 6357 (2016).
- <sup>15</sup>W. Wang, L. A. Castro, M. Hoyos, and T. E. Mallouk, *ACS Nano* **6**, 6122 (2012).
- <sup>16</sup>R. Dreyfus, J. Baudry, M. L. Roper, M. Fermigier, H. A. Stone, and J. Bibette, *Nature* **437**, 862 (2005).
- <sup>17</sup>G. Grosjean, G. Lagubeau, A. Darras, M. Hubert, G. Lumay, and N. Vandewalle, *Sci. Rep.* **5**, 16035 (2015).
- <sup>18</sup>G. Steinbach, S. Gemming, and A. Erbe, *Eur. Phys. J. E* **39**, 69 (2016).
- <sup>19</sup>A. Kaiser, A. Snezhko, and I. S. Aranson, *Sci. Adv.* **3**, e1601469 (2017).
- <sup>20</sup>A. Bricard, J.-B. Caussin, N. Desreumaux, O. Dauchot, and D. Bartolo, *Nature* **503**, 95 (2013).
- <sup>21</sup>A. Morin, N. Desreumaux, J.-B. Caussin, and D. Bartolo, *Nat. Phys.* **13**, 63 (2017).
- <sup>22</sup>C. J. Olson Reichhardt and C. Reichhardt, *Annu. Rev. Condens. Matter Phys.* **8**, 51 (2017).
- <sup>23</sup>O. Pohl and H. Stark, *Phys. Rev. Lett.* **112**, 238303 (2014).
- <sup>24</sup>S. Saha, R. Golestanian, and S. Ramaswamy, *Phys. Rev. E* **89**, 062316 (2014).
- <sup>25</sup>B. Liebchen, D. Marenduzzo, I. Pagonabarraga, and M. E. Cates, *Phys. Rev. Lett.* **115**, 258301 (2015).
- <sup>26</sup>B. Liebchen, D. Marenduzzo, and M. E. Cates, *Phys. Rev. Lett.* **118**, 268001 (2017).
- <sup>27</sup>C. Jin, C. Krüger, and C. C. Maass, *Proc. Natl. Acad. Sci. U. S. A.* **114**, 5089 (2017).
- <sup>28</sup>W. Gao, D. Kagan, O. S. Pak, C. Clawson, S. Campuzano, E. Chuluun-Erdene, E. Shipton, E. E. Fullerton, L. Zhang, E. Lauga, and J. Wang, *Small* **8**, 460 (2012).
- <sup>29</sup>Y. Hong, D. Velegol, N. Chaturvedi, and A. Sen, *Phys. Chem. Chem. Phys.* **12**, 1423 (2010).
- <sup>30</sup>Y. Hong, N. M. K. Blackman, N. D. Kopp, A. Sen, and D. Velegol, *Phys. Rev. Lett.* **99**, 178103 (2007).
- <sup>31</sup>P. K. Ghosh, Y. Li, F. Marchesoni, and F. Nori, *Phys. Rev. E* **92**, 012114 (2015).
- <sup>32</sup>M. P. Magiera and L. Brendel, *Phys. Rev. E* **92**, 012304 (2015).
- <sup>33</sup>J. Grauer, H. Löwen, and L. M. C. Janssen, *Phys. Rev. E* **97**, 022608 (2018).
- <sup>34</sup>J. Stenhammar, R. Wittkowski, D. Marenduzzo, and M. E. Cates, *Sci. Adv.* **2**, e1501850 (2016).
- <sup>35</sup>C. Lozano, B. ten Hagen, H. Löwen, and C. Bechinger, *Nat. Commun.* **7**, 12828 (2016).
- <sup>36</sup>A. Geiseler, P. Hänggi, F. Marchesoni, C. Mulhern, and S. Savel'ev, *Phys. Rev. E* **94**, 012613 (2016).
- <sup>37</sup>A. Geiseler, P. Hänggi, and F. Marchesoni, *Entropy* **19**, 97 (2017).
- <sup>38</sup>A. Geiseler, P. Hänggi, and F. Marchesoni, *Sci. Rep.* **7**, 41884 (2017).
- <sup>39</sup>A. Sharma and J. M. Brader, *Phys. Rev. E* **96**, 032604 (2017).
- <sup>40</sup>F. Kümmel, B. ten Hagen, R. Wittkowski, I. Buttinoni, R. Eichhorn, G. Volpe, H. Löwen, and C. Bechinger, *Phys. Rev. Lett.* **110**, 198302 (2013).
- <sup>41</sup>I. Buttinoni, J. Bialké, F. Kümmel, H. Löwen, C. Bechinger, and T. Speck, *Phys. Rev. Lett.* **110**, 238301 (2013).
- <sup>42</sup>B. ten Hagen, F. Kümmel, R. Wittkowski, D. Takagi, H. Löwen, and C. Bechinger, *Nat. Commun.* **5**, 4829 (2014).
- <sup>43</sup>N. Razin, R. Voituriez, J. Elgeti, and N. S. Gov, *Phys. Rev. E* **96**, 052409 (2017).
- <sup>44</sup>H. Löwen, T. Horn, T. Neuhaus, and B. ten Hagen, *Eur. Phys. J. Spec. Top.* **222**, 2961 (2013).
- <sup>45</sup>H. Löwen, *J. Phys.: Condens. Matter* **10**, L479 (1998).
- <sup>46</sup>A. Torres, A. Cuetos, M. Dijkstra, and R. van Roij, *Phys. Rev. E* **75**, 041405 (2007).
- <sup>47</sup>T.-Y. Wang, H.-T. Li, Y.-J. Sheng, and H.-K. Tsao, *J. Chem. Phys.* **129**, 204504 (2008).
- <sup>48</sup>H. Löwen and E. Allahyarov, *J. Chem. Phys.* **135**, 134115 (2011).
- <sup>49</sup>A. P. Philipse, *Curr. Opin. Colloid Interface Sci.* **2**, 200 (1997).
- <sup>50</sup>M. Raša and A. P. Philipse, *Nature* **429**, 857 (2004).
- <sup>51</sup>R. Piazza, T. Bellini, and V. Degiorgio, *Phys. Rev. Lett.* **71**, 4267 (1993).
- <sup>52</sup>N. J. Lorenz, H. J. Schöep, and T. Palberg, *J. Chem. Phys.* **131**, 134501 (2009).
- <sup>53</sup>G. Brambilla, S. Buzzaccaro, R. Piazza, L. Berthier, and L. Cipelletti, *Phys. Rev. Lett.* **106**, 118302 (2011).
- <sup>54</sup>R. Piazza, *Rep. Prog. Phys.* **77**, 056602 (2014).
- <sup>55</sup>A. P. J. Breu, H.-M. Ensner, C. A. Krüelle, and I. Rehberg, *Phys. Rev. Lett.* **90**, 014302 (2003).
- <sup>56</sup>V. Garzó, *Phys. Rev. E* **78**, 020301(R) (2008).
- <sup>57</sup>S. Godoy, D. Riso, R. Soto, and P. Cordero, *Phys. Rev. E* **78**, 031301 (2008).
- <sup>58</sup>C. Lozano, I. Zuriguel, A. Garcimartín, and T. Mullin, *Phys. Rev. Lett.* **114**, 178002 (2015).
- <sup>59</sup>D. C. Hong, P. V. Quinn, and S. Luding, *Phys. Rev. Lett.* **86**, 3423 (2001).
- <sup>60</sup>A. Rosato, K. J. Strandburg, F. Prinz, and R. H. Swendsen, *Phys. Rev. Lett.* **58**, 1038 (1987).
- <sup>61</sup>T. Biben and J.-P. Hansen, *Mol. Phys.* **80**, 853 (1993).
- <sup>62</sup>A. Esztermann and H. Löwen, *Europhys. Lett.* **68**, 120 (2004).
- <sup>63</sup>J. Zwanikken and R. van Roij, *Europhys. Lett.* **71**, 480 (2005).
- <sup>64</sup>E. Spruijt and P. M. Biesheuvel, *J. Phys.: Condens. Matter* **26**, 075101 (2014).
- <sup>65</sup>M. Dijkstra, J. Zwanikken, and R. van Roij, *J. Phys.: Condens. Matter* **18**, 825 (2006).
- <sup>66</sup>P. M. Biesheuvel and J. Lyklema, *J. Phys.: Condens. Matter* **17**, 6337 (2005).
- <sup>67</sup>S.-C. Kim and Y.-S. Han, *J. Mol. Liq.* **208**, 298 (2015).
- <sup>68</sup>T. Kruppa, T. Neuhaus, R. Messina, and H. Löwen, *J. Chem. Phys.* **136**, 134106 (2012).
- <sup>69</sup>N. Razin, R. Voituriez, J. Elgeti, and N. S. Gov, *Phys. Rev. E* **96**, 032606 (2017).
- <sup>70</sup>J. D. Weeks, D. Chandler, and H. C. Andersen, *J. Chem. Phys.* **54**, 5237 (1971).
- <sup>71</sup>B. Liebchen and H. Löwen, e-print [arXiv:1808.07389](https://arxiv.org/abs/1808.07389) (2018).
- <sup>72</sup>A. P. Solon, J. Stenhammar, R. Wittkowski, M. Kardar, Y. Kafri, M. E. Cates, and J. Tailleur, *Phys. Rev. Lett.* **114**, 198301 (2015).
- <sup>73</sup>R. Evans, *Adv. Phys.* **28**, 143 (1979).
- <sup>74</sup>A. Parola, S. Buzzaccaro, E. Secchi, and R. Piazza, *J. Chem. Phys.* **138**, 114907 (2013).
- <sup>75</sup>R. Piazza, S. Buzzaccaro, E. Secchi, and A. Parola, *Soft Matter* **8**, 7112 (2012).
- <sup>76</sup>J. R. Gomez-Solano, S. Samin, C. Lozano, P. Ruedas-Batuecas, R. van Roij, and C. Bechinger, *Sci. Rep.* **7**, 14891 (2017).
- <sup>77</sup>C. Lozano, J. R. Gomez-Solano, and C. Bechinger, *New J. Phys.* **20**, 015008 (2018).
- <sup>78</sup>M. Enculescu and H. Stark, *Phys. Rev. Lett.* **107**, 058301 (2011).
- <sup>79</sup>K. Wolff, A. M. Hahn, and H. Stark, *Eur. Phys. J. E* **36**, 43 (2013).
- <sup>80</sup>F. Ginot, A. Solon, Y. Kafri, C. Ybert, J. Tailleur, and C. Cottin-Bizonne, *New J. Phys.* **20**, 115001 (2018).

<sup>81</sup>F. Smalenburg and H. Löwen, *Phys. Rev. E* **92**, 032304 (2015).

<sup>82</sup>N. Nikola, A. P. Solon, Y. Kafri, M. Kardar, J. Tailleur, and R. Voituriez, *Phys. Rev. Lett.* **117**, 098001 (2016).

<sup>83</sup>F. Ginot, I. Theurkauff, D. Levis, C. Ybert, L. Bocquet, L. Berthier, and C. Cottin-Bizonne, *Phys. Rev. X* **5**, 011004 (2015).

<sup>84</sup>A. I. Campbell, R. Wittkowski, B. ten Hagen, H. Löwen, and S. J. Ebbens, *J. Chem. Phys.* **147**, 084905 (2017).

<sup>85</sup>A. Dominguez, P. Magaretti, M. N. Popescu, and S. Dietrich, *Soft Matter* **12**, 8398 (2016).

<sup>86</sup>F. Martinez-Pedrero, E. Navarro-Argemí, A. Ortiz-Ambriz, I. Pagonabarraga, and P. Tierno, *Sci. Adv.* **4**, eaap9379 (2018).

<sup>87</sup>A. Wysocki, R. G. Winkler, and G. Gompper, *New J. Phys.* **18**, 123030 (2016).

<sup>88</sup>N. Bain and D. Bartolo, *Nat. Commun.* **8**, 15969 (2017).

<sup>89</sup>S. Kumari, A. S. Nunes, N. A. M. Araújo, and M. M. Telo da Gama, *J. Chem. Phys.* **147**, 174702 (2017).

<sup>90</sup>R. Wittmann, J. M. Brader, A. Sharma, and U. M. B. Marconi, *Phys. Rev. E* **97**, 012601 (2018).



## 6 Concluding remarks

Here I briefly summarize the most important features of my research during my Ph.D. study and I present a short perspective. I have studied the dynamics of active Brownian particles both as a single agent and when in interaction with other particles, while the translational and rotational motions are confined to a two-dimensional plane. The here-presented studies include active Brownian particles with non-negligible inertial effects referred to as microflyers, and active Brownian particles with negligible inertial effects referred to as microswimmers.

I have shown that, opposed to the long-time behavior of passive particles, which is independent of the moment of inertia and dependent just on friction coefficient through Stokes-Einstein relation, the long-time dynamics of microflyers depends explicitly on the moment of inertia. These results provide a route towards novel control strategies in active systems using the moment of inertia as a variable parameter. For instance, animals can change their moment of inertia –since changing of mass is not usually a rapid process for them– through restyling their mass distribution around their axis of rotation leading to stabilizing their motion, for example, in fast turns [152]. Due to vanishing inertial effects, the velocity of microswimmers pursues instantaneously the changes in their orientation, however, the inertial effects in microflyers result in a time delay between the orientation variations and the subsequent changes in the velocity direction, which demonstrates the profound influence of inertia on dynamics.

For circle flyers, the transient initial regime of the noise-free dynamics depends on the moment of inertia in motion; explicitly, the higher the moment of inertia is, the longer the initial regime takes. This reflects the fact that the moment of inertia quantifies the resistance to changing the angular momentum. However, after the relaxation of the initial regime, the final flying path is independent of the moment of inertia and just dependent on mass.

I have found an interesting interplay between circling frequency and propulsion frequency in the dynamics of a circle flyer with oscillating propulsion speed. I have specifically presented general results for mean-square displacement and inertial delay. I have demonstrated that the inertial delay is not affected by propulsion oscillations and is the same as that for a circle flyer with time-independent self-propulsion.

I have studied the dynamics of a microflyer with time-dependent inertia, damping, self-propulsion, and fluctuations in two limiting cases; when variations are slow, and for rapid oscillations. I have highlighted that a microflyer can undergo anomalous diffusion if temporally varying parameters are included. This study emphasizes that the diffusion transport process can be adjusted by taking into account an appropriate time-dependence with regard to the system's parameters.

For future studies, it is interesting to study the interaction of microflyers with physical obstacles and boundaries in complex environments. For example, geometric confinements can drastically alter the transport properties of microswimmers [153, 154, 155]. Moreover, future studies should focus on mixtures of interacting microflyers and investigate the collective behavior of such systems in simple or complex environments [156].

Furthermore, we presented a generic scheme to trap microswimmers, without requiring any body-forces. By specifically exploiting self-propulsion to systematically bias the motion towards the trapping center, it serves as an alternative to conventional trapping schemes involving body-forces competing with self-propulsion. This leads to exponential localization, even for fast active particles. This mechanism can hence be used as a tweezer to transfer fast microswimmers over a barrier; specifically, self-propulsion helps to overcome the barrier. This is in contrast to force-based trapping where self-propulsion away from the trapping center is suppressed by the body-forces used to achieve trapping.

Our trapping mechanism opens a route towards widespread novel applications, e.g. as a tool to measure unknown coupling coefficients of microswimmers to external fields, which may help to better understand their mutual interactions. Such controlled localization may also be useful in situations where directed motion of autonomous self-propelled objects is required, for example, in applications where they serve as microshuttles for directed cargo delivery.

Future studies should include a finite concentration of microswimmers in a one-dimensional periodic landscape of the groove geometry of our trapping mechanism. In such a landscape, repulsive microswimmers will form crystalline one-dimensional arrays which exhibit novel dynamical modes, even in the absence of noise. While negatively phototactic microswimmers will basically assemble in the motility minima, positively phototactic ones exhibit motility-induced oscillatory modes which are very different from thermally activated phonons. In some analogy to crystals of trapped atoms and ions [157, 158, 159], such a chain of vibrating particles is expected to buckle [160, 161] and synchronize showing topologically protected solitons, novel defect dynamics and active nano-frictional effects.

# Bibliography

- [1] S. Ramaswamy, *The mechanics and statistics of active matter*, **1**, 323 (2010).
- [2] D. Needleman and Z. Dogic, *Active matter at the interface between materials science and cell biology*, *Nat. Rev. Mater.* **2**, 17048 (2017).
- [3] A. Doostmohammadi, J. Ignés-Mullol, J. M. Yeomans, and F. Sagués, *Active nematics*, *Nat. Commun.* **9**, 3246 (2018).
- [4] X. Chen, C. Zhou, and W. Wang, *Colloidal motors 101: A beginner's guide to colloidal motor research*, *Chem. Asian J.* **14**, 2388 (2019).
- [5] M. C. Marchetti, J. F. Joanny, S. Ramaswamy, T. B. Liverpool, J. Prost, M. Rao, and R. A. Simha, *Hydrodynamics of soft active matter*, *Rev. Mod. Phys.* **85**, 1143 (2013).
- [6] G. M. Viswanathan, M. G. E. da Luz, E. P. Raposo, and H. E. Stanley, *The physics of foraging: An introduction to random searches and biological encounters* (Cambridge University Press, Cambridge, UK, 2011).
- [7] V. Méndez, D. Campos, and F. Bartumeus, *Stochastic foundations in movement ecology: Anomalous diffusion, front propagation and random searches* (Springer-Verlag, Berlin, 2014).
- [8] J. Wang and W. Gao, *Nano/microscale motors: Biomedical opportunities and challenges*, *ACS Nano* **6**, 5745 (2012).
- [9] L. K. E. A. Abdelmohsen, F. Peng, Y. Tu, and D. A. Wilson, *Micro- and nano-motors for biomedical applications*, *J. Mater. Chem. B* **2**, 2395 (2014).
- [10] M. Brambilla, E. Ferrante, M. Birattari, and M. Dorigo, *Swarm robotics: a review from the swarm engineering perspective*, *Swarm Intelligence* **7**, 1 (2013).
- [11] D. Helbing, *Traffic and related self-driven many-particle systems*, *Rev. Mod. Phys.* **73**, 1067 (2001).
- [12] W. Gao and J. Wang, *The environmental impact of micro/nanomachines: A review*, *ACS Nano* **8**, 3170 (2014).
- [13] C. W. Reynolds, *Flocks, herds and schools: A distributed behavioral model*, *SIGGRAPH Comput. Graph.* **21**, 25 (1987).
- [14] T. Vicsek, A. Czirok, E. Ben-Jacob, I. Cohen, and O. Shochet, *Novel type of phase transition in a system of self-driven particles*, *Phys. Rev. Lett.* **75**, 1226 (1995).

- [15] J. Buhl, D. J. T. Sumpter, I. D. Couzin, J. J. Hale, E. Despland, E. R. Miller, and S. J. Simpson, *From disorder to order in marching locusts*, Science **312**, 1402 (2006).
- [16] D. Babič, C. Schmitt, and C. Bechinger, *Colloids as model systems for problems in statistical physics*, Chaos **15**, 026114 (2005).
- [17] U. Erdmann, W. Ebeling, L. Schimansky-Geier, and F. Schweitzer, *Brownian particles far from equilibrium*, Eur. Phys. J. B **15**, 105 (2000).
- [18] P. Hänggi and F. Marchesoni, *Artificial brownian motors: Controlling transport on the nanoscale*, Rev. Mod. Phys. **81**, 387 (2009).
- [19] E. Lauga, W. R. DiLuzio, G. M. Whitesides, and H. A. Stone, *Swimming in circles: motion of bacteria near solid boundaries*, Biophys. J. **90**, 400 (2006).
- [20] A. S. Utada, R. R. Bennett, J. C. N. Fong, M. L. Gibiansky, F. H. Yildiz, R. Golestanian, and G. C. L. Wong, *Vibrio cholerae use pili and flagella synergistically to effect motility switching and conditional surface attachment*, Nat. Commun. **5**, 4913 (2014).
- [21] G. Volpe, I. Buttinoni, D. Vogt, H.-J. Kümmerer, and C. Bechinger, *Microswimmers in patterned environments*, Soft Matter **7**, 8810 (2011).
- [22] I. Buttinoni, G. Volpe, F. Kümmel, G. Volpe, and C. Bechinger, *Active brownian motion tunable by light*, J. Phys. Condens. Matter **24**, 284129 (2012).
- [23] F. Kümmel, B. ten Hagen, R. Wittkowski, I. Buttinoni, R. Eichhorn, G. Volpe, H. Löwen, and C. Bechinger, *Circular motion of asymmetric self-propelling particles*, Phys. Rev. Lett. **110**, 198302 (2013).
- [24] C. Bechinger, R. Di Leonardo, H. Löwen, C. Reichhardt, G. Volpe, and G. Volpe, *Active particles in complex and crowded environments*, Rev. Mod. Phys. **88**, 045006 (2016).
- [25] B. ten Hagen, R. Wittkowski, D. Takagi, F. Kümmel, C. Bechinger, and H. Löwen, *Can the self-propulsion of anisotropic microswimmers be described by using forces and torques?*, J. Phys. Condens. Matter **27**, 194110 (2015).
- [26] J. Elgeti, U. B. Kaupp, and G. Gompper, *Hydrodynamics of sperm cells near surfaces*, Biophys. J. **99**, 1018 (2010).
- [27] A. A. Evans and E. Lauga, *Propulsion by passive filaments and active flagella near boundaries*, Phys. Rev. E **82**, 041915 (2010).
- [28] S. E. Spagnolie and E. Lauga, *Hydrodynamics of self-propulsion near a boundary: predictions and accuracy of far-field approximations*, J. Fluid Mech. **700**, 105 (2012).
- [29] S. Das, A. Garg, A. I. Campbell, J. Howse, A. Sen, D. Velegol, R. Golestanian, and S. J. Ebbens, *Boundaries can steer active janus spheres*, Nat. Commun. **6**, 8999 (2015).

- [30] J. Simmchen, J. Katuri, W. E. Usual, M. N. Popescu, M. Tasinkevych, and S. Sánchez, *Topographical pathways guide chemical microswimmers*, Nat. Commun. **7**, 10598 (2016).
- [31] J. Deseigne, O. Dauchot, and H. Chaté, *Collective motion of vibrated polar disks*, Phys. Rev. Lett. **105**, 098001 (2010).
- [32] C. Scholz, M. Engel, and T. Pöschel, *Rotating robots move collectively and self-organize*, Nat. Commun. **9**, 931 (2018).
- [33] H. Wioland, F. G. Woodhouse, J. Dunkel, J. O. Kessler, and R. E. Goldstein, *Confinement stabilizes a bacterial suspension into a spiral vortex*, Phys. Rev. Lett. **110**, 268102 (2013).
- [34] B. Liebchen and H. Löwen, *Which interactions dominate in active colloids?*, J. Chem. Phys. **150**, 061102 (2019).
- [35] B. Liebchen and H. Löwen, *Response to “comment on ‘which interactions dominate in active colloids?’”* [*j. chem. phys.* **151**, 067101 (2019)], J. Chem. Phys. **151**, 067102 (2019).
- [36] D. S. Lemons and A. Gythiel, *Paul langevin’s 1908 paper “on the theory of brownian motion”* [*“sur la théorie du mouvement brownien,” c. r. acad. sci. (paris)* **146**, 530–533 (1908)], Am. J. Phys. **65**, 1079 (1997).
- [37] C. A. Weber, T. Hanke, J. Deseigne, S. Léonard, O. Dauchot, E. Frey, and H. Chaté, *Long-range ordering of vibrated polar disks*, Phys. Rev. Lett. **110**, 208001 (2013).
- [38] Z. Mokhtari, T. Aspelmeier, and A. Zippelius, *Collective rotations of active particles interacting with obstacles*, EPL **120**, 14001 (2017).
- [39] A. Goldman, R. Cox, and H. Brenner, *Slow viscous motion of a sphere parallel to a plane wall—I motion through a quiescent fluid*, Chem. Eng. Sci. **22**, 637 (1967).
- [40] H. Löwen. *Inertial effects of self-propelled particles: from active brownian to active langevin motion*. (to be published).
- [41] G. E. Morfill and A. V. Ivlev, *Complex plasmas: An interdisciplinary research field*, Rev. Mod. Phys. **81**, 1353 (2009).
- [42] K. R. Sütterlin, A. Wysocki, A. V. Ivlev, C. Râth, H. M. Thomas, M. Rubin-Zuzic, W. J. Goedheer, V. E. Fortov, A. M. Lipaev, V. I. Molotkov, O. F. Petrov, G. E. Morfill, and H. Löwen, *Dynamics of lane formation in driven binary complex plasmas*, Phys. Rev. Lett. **102**, 085003 (2009).
- [43] L. Couëdel, V. Nosenko, A. V. Ivlev, S. K. Zhdanov, H. M. Thomas, and G. E. Morfill, *Direct observation of mode-coupling instability in two-dimensional plasma crystals*, Phys. Rev. Lett. **104**, 195001 (2010).
- [44] M. Chaudhuri, A. V. Ivlev, S. A. Khrapak, H. M. Thomas, and G. E. Morfill, *Complex plasma-the plasma state of soft matter*, Soft Matter **7**, 1287 (2011).

- [45] A. V. Ivlev, J. Bartnick, M. Heinen, C.-R. Du, V. Nosenko, and H. Löwen, *Statistical mechanics where newton's third law is broken*, Phys. Rev. X **5**, 011035 (2015).
- [46] A. Ivlev, H. Löwen, G. Morfill, and C. P. Royall, *Complex Plasmas and Colloidal Dispersions* (World Scientific, 2012).
- [47] V. Narayan, S. Ramaswamy, and N. Menon, *Long-lived giant number fluctuations in a swarming granular nematic*, Science **317**, 105 (2007).
- [48] A. Kudrolli, G. Lumay, D. Volfson, and L. S. Tsimring, *Swarming and swirling in self-propelled polar granular rods*, Phys. Rev. Lett. **100**, 058001 (2008).
- [49] J. Deseigne, O. Dauchot, and H. Chaté, *Collective motion of vibrated polar disks*, Phys. Rev. Lett. **105**, 098001 (2010).
- [50] L. Giomi, N. Hawley-Weld, and L. Mahadevan, *Swarming, swirling and stasis in sequestered bristle-bots*, Proc. Royal Soc. A **469**, 20120637 (2013).
- [51] C. A. Weber, T. Hanke, J. Deseigne, S. Léonard, O. Dauchot, E. Frey, and H. Chaté, *Long-range ordering of vibrated polar disks*, Phys. Rev. Lett. **110**, 208001 (2013).
- [52] G. A. Patterson, P. I. Fierens, F. Sangiuliano Jimka, P. G. König, A. Garcimartín, I. Zuriguel, L. A. Pugnaloni, and D. R. Parisi, *Clogging transition of vibration-driven vehicles passing through constrictions*, Phys. Rev. Lett. **119**, 248301 (2017).
- [53] G. Junot, G. Briand, R. Ledesma-Alonso, and O. Dauchot, *Active versus passive hard disks against a membrane: Mechanical pressure and instability*, Phys. Rev. Lett. **119**, 028002 (2017).
- [54] A. Deblais, T. Barois, T. Guerin, P. H. Delville, R. Vaudaine, J. S. Lintuvuori, J. F. Boudet, J. C. Baret, and H. Kellay, *Boundaries control collective dynamics of inertial self-propelled robots*, Phys. Rev. Lett. **120**, 188002 (2018).
- [55] O. Dauchot and V. Démery, *Dynamics of a self-propelled particle in a harmonic trap*, Phys. Rev. Lett. **122**, 068002 (2019).
- [56] M. Rubenstein, A. Cornejo, and R. Nagpal, *Programmable self-assembly in a thousand-robot swarm*, Science **345**, 795 (2014).
- [57] Z. Zhakypov, K. Mori, K. Hosoda, and J. Paik, *Designing minimal and scalable insect-inspired multi-locomotion millirobots*, Nature **571**, 381 (2019).
- [58] J. Rabault, R. A. Fauli, and A. Carlson, *Curving to fly: Synthetic adaptation unveils optimal flight performance of whirling fruits*, Phys. Rev. Lett. **122**, 024501 (2019).



- [59] R. A. Fauli, J. Rabault, and A. Carlson, *Effect of wing fold angles on the terminal descent velocity of double-winged autorotating seeds, fruits, and other diaspores*, Phys. Rev. E **100**, 013108 (2019).
- [60] J. Toner and Y. Tu, *Long-range order in a two-dimensional dynamical XY model: How birds fly together*, Phys. Rev. Lett. **75**, 4326 (1995).
- [61] J. Toner and Y. Tu, *Flocks, herds, and schools: A quantitative theory of flocking*, Phys. Rev. E **58**, 4828 (1998).
- [62] A. Attanasi, A. Cavagna, L. Del Castello, I. Giardina, T. S. Grigera, A. Jelic, S. Melillo, L. Parisi, O. Pohl, E. Shen, and M. Viale, *Information transfer and behavioural inertia in starling flocks*, Nat. Phys. **10**, 692 (2014).
- [63] E. Chiappini, in *Encyclopedia of Entomology*, edited by J. L. Capinera (Springer Netherlands, Dordrecht, 2008).
- [64] J. Bartussek and F. O. Lehmann, *Proprioceptive feedback determines visuo-motor gain in drosophila*, Royal Soc. Open Sci. **3**, 150562 (2016).
- [65] H. Mukundarajan, T. C. Bardon, D. H. Kim, and M. Prakash, *Surface tension dominates insect flight on fluid interfaces*, J. Exp. Biol. **219**, 752 (2016).
- [66] J. Bartussek and F. O. Lehmann, *Sensory processing by motoneurons: a numerical model for low-level flight control in flies*, J. Royal Soc. Interface **15**, 20180408 (2018).
- [67] M. Enculescu and H. Stark, *Active colloidal suspensions exhibit polar order under gravity*, Phys. Rev. Lett. **107**, 058301 (2011).
- [68] M. Joyeux and E. Bertin, *Pressure of a gas of underdamped active dumbbells*, Phys. Rev. E **93**, 032605 (2016).
- [69] A. Manacorda and A. Puglisi, *Lattice model to derive the fluctuating hydrodynamics of active particles with inertia*, Phys. Rev. Lett. **119**, 208003 (2017).
- [70] S. C. Takatori and J. F. Brady, *Inertial effects on the stress generation of active fluids*, Phys. Rev. Fluids **2**, 094305 (2017).
- [71] S. Das, G. Gompper, and R. G. Winkler, *Local stress and pressure in an inhomogeneous system of spherical active brownian particles*, Sci. Rep. **9**, 6608 (2019).
- [72] H. Löwen, *Active particles in noninertial frames: How to self-propel on a carousel*, Phys. Rev. E **99**, 062608 (2019).
- [73] F. Kümmel, B. ten Hagen, R. Wittkowski, I. Buttinoni, R. Eichhorn, G. Volpe, H. Löwen, and C. Bechinger, *Circular motion of asymmetric self-propelling particles*, Phys. Rev. Lett. **110**, 198302 (2013).
- [74] B. ten Hagen, F. Kümmel, R. Wittkowski, D. Takagi, H. Löwen, and C. Bechinger, *Gravitaxis of asymmetric self-propelled colloidal particles*, Nat. Commun. **5**, 4829 (2014).

- [75] D. Takagi, A. B. Braunschweig, J. Zhang, and M. J. Shelley, *Dispersion of self-propelled rods undergoing fluctuation-driven flips*, Phys. Rev. Lett. **110**, 038301 (2013).
- [76] J.-F. Rupprecht, N. Waisbord, C. Ybert, C. Cottin-Bizonne, and L. Bocquet, *Velocity condensation for magnetotactic bacteria*, Phys. Rev. Lett. **116**, 168101 (2016).
- [77] L. Baraban, D. Makarov, R. Streubel, I. Moench, D. Grimm, S. Sanchez, and O. G. Schmidt, *Catalytic janus motors on microfluidic chip: Deterministic motion for targeted cargo delivery*, ACS Nano **6**, 3383 (2012).
- [78] H. Moyses, J. Palacci, S. Sacanna, and D. G. Grier, *Trochoidal trajectories of self-propelled janus particles in a diverging laser beam*, Soft Matter **12**, 6357 (2016).
- [79] C. Scholz, S. D'Silva, and T. Pöschel, *Ratcheting and tumbling motion of vibrots*, New J. Phys. **18**, 123001 (2016).
- [80] E. Altshuler, J. M. Pastor, A. Garcimartín, I. Zuriguel, and D. Maza, *Vibrot, a simple device for the conversion of vibration into rotation mediated by friction: Preliminary evaluation*, PLoS One **8**, 1 (2013).
- [81] N. Koumakis, A. Gnoli, C. Maggi, A. Puglisi, and R. D. Leonardo, *Mechanism of self-propulsion in 3d-printed active granular particles*, New J. Phys. **18**, 113046 (2016).
- [82] H. M. Jaeger, S. R. Nagel, and R. P. Behringer, *Granular solids, liquids, and gases*, Rev. Mod. Phys. **68**, 1259 (1996).
- [83] J. Blum, S. Bruns, D. Rademacher, A. Voss, B. Willenberg, and M. Krause, *Measurement of the translational and rotational brownian motion of individual particles in a rarefied gas*, Phys. Rev. Lett. **97**, 230601 (2006).
- [84] T. Li, S. Kheifets, D. Medellin, and M. G. Raizen, *Measurement of the instantaneous velocity of a brownian particle*, Science **328**, 1673 (2010).
- [85] R. Huang, I. Chavez, K. M. Taute, B. Lukic, S. Jeney, M. G. Raizen, and E.-L. Florin, *Direct observation of the full transition from ballistic to diffusive brownian motion in a liquid*, Nat. Phys. **7**, 576 (2011).
- [86] G. D. Birkhoff, *Proof of the ergodic theorem*, Proc. Natl. Acad. Sci. **17**, 656 (1931).
- [87] J. v. Neumann, *Proof of the quasi-ergodic hypothesis*, Proc. Natl. Acad. Sci. **18**, 70 (1932).
- [88] C. C. Moore, *Ergodic theorem, ergodic theory, and statistical mechanics*, Proc. Natl. Acad. Sci. **112**, 1907 (2015).
- [89] C. Hoell, H. Löwen, and A. M. Menzel, *Dynamical density functional theory for circle swimmers*, New J. Phys. **19**, 125004 (2017).

- [90] C. Weber, P. K. Radtke, L. Schimansky-Geier, and P. Hänggi, *Active motion assisted by correlated stochastic torques*, Phys. Rev. E **84**, 011132 (2011).
- [91] R. Wittmann, C. Maggi, A. Sharma, A. Scacchi, J. M. Brader, and U. M. B. Marconi, *Effective equilibrium states in the colored-noise model for active matter i. pairwise forces in the fox and unified colored noise approximations*, J. Stat. Mech.: Theory Exp. **2017**, 113207 (2017).
- [92] J. Hansen and I. McDonald. *Theory of Simple Liquids*. Academic Press, Burlington, (2006).
- [93] R. B. Paris, in *NIST Handbook of Mathematical Functions*, edited by F. W. J. Olver, D. M. Lozier, R. F. Boisvert, and C. W. Clark (Cambridge University Press, 2010).
- [94] J. R. Howse, R. A. L. Jones, A. J. Ryan, T. Gough, R. Vafabakhsh, and R. Golestanian, *Self-motile colloidal particles: From directed propulsion to random walk*, Phys. Rev. Lett. **99**, 048102 (2007).
- [95] B. Hagen, S. van Teeffelen, and H. Löwen, *Non-gaussian behaviour of a self-propelled particle on a substrate*, Condens Matter Phys. **12**, 725 (2009).
- [96] C. Vandenberg and J. Rayner, *The moment of inertia of bird wings and the inertial power requirement for flapping flight*, J. Exp. Biol. **198**, 1655 (1995).
- [97] M. Qiao, B. Brown, and D. L. Jindrich, *Compensations for increased rotational inertia during human cutting turns*, J. Exp. Biol. **217**, (2014).
- [98] J. Embs, H. W. Müller, C. Wagner, K. Knorr, and M. Lücke, *Measuring the rotational viscosity of ferrofluids without shear flow*, Phys. Rev. E **61**, R2196 (2000).
- [99] B. A. Stickler, B. Schirnski, and K. Hornberger, *Rotational friction and diffusion of quantum rotors*, Phys. Rev. Lett. **121**, 040401 (2018).
- [100] F. O. Eke and T. C. Mao, *On the dynamics of variable mass systems*, IJMEE **30**, 123 (2002).
- [101] V. Panchal and R. Jangid, *Variable friction pendulum system for seismic isolation of liquid storage tanks*, Nucl. Eng. Des. **238**, 1304 (2008).
- [102] R. Metzler, E. Barkai, and J. Klafter, *Anomalous diffusion and relaxation close to thermal equilibrium: A fractional fokker-planck equation approach*, Phys. Rev. Lett. **82**, 3563 (1999).
- [103] R. Golestanian, *Anomalous diffusion of symmetric and asymmetric active colloids*, Phys. Rev. Lett. **102**, 188305 (2009).
- [104] F. Hoefling and T. Franosch, *Anomalous transport in the crowded world of biological cells*, Rep. Prog. Phys. **76**, 046602 (2013).
- [105] J. Bleibel, A. Dominguez, F. Gunther, J. Harting, and M. Oettel, *Hydrodynamic interactions induce anomalous diffusion under partial confinement*, Soft Matter **10**, 2945 (2014).

- [106] A. Morin, D. L. Cardozo, V. Chikkadi, and D. Bartolo, *Diffusion, subdiffusion, and localization of active colloids in random post lattices*, Phys. Rev. E **96**, 042611 (2017).
- [107] A. Taloni, O. Flomenbom, R. Castaneda-Priego, and F. Marchesoni, *Single file dynamics in soft materials*, Soft Matter **13**, 1096 (2017).
- [108] Y. Chen, X. Wang, and W. Deng, *Langevin picture of lévy walk in a constant force field*. arXiv:1909.13685, (2019).
- [109] C. Charalambous, M. Ángel García-March, G. Muñoz-Gil, P. R. Grzybowski, and M. Lewenstein. *Control of anomalous diffusion of a bose polaron*. arXiv:1910.01571, (2019).
- [110] F. A. Oliveira, R. M. S. Ferreira, L. C. Lapas, and M. H. Vainstein, *Anomalous diffusion: A basic mechanism for the evolution of inhomogeneous systems*, Front. Phys. **7**, 18 (2019).
- [111] S. Babel, B. ten Hagen, and H. Löwen, *Swimming path statistics of an active brownian particle with time-dependent self-propulsion*, J. Stat. Mech.: Theory Exp. **2014**, P02011 (2014).
- [112] S. Jahanshahi, H. Löwen, and B. ten Hagen, *Brownian motion of a circle swimmer in a harmonic trap*, Phys. Rev. E **95**, 022606 (2017).
- [113] B. ten Hagen, S. van Teeffelen, and H. Löwen, *Brownian motion of a self-propelled particle*, J. Phys.: Condens. Matter **23**, 194119 (2011).
- [114] C. Kurzthaler, C. Devailly, J. Arlt, T. Franosch, W. C. K. Poon, V. A. Martinez, and A. T. Brown, *Probing the spatiotemporal dynamics of catalytic janus particles with single-particle tracking and differential dynamic microscopy*, Phys. Rev. Lett. **121**, 078001 (2018).
- [115] E. M. Purcell, *Life at low reynolds number*, Am. J. Phys. **45**, 3 (1977).
- [116] D. Woolley, *Motility of spermatozoa at surfaces*, Reproduction **126**, 259 (2003).
- [117] I. Riedel, K. Kruse, and J. Howard, *A self-organized vortex array of hydrodynamically entrained sperm cells*, Science **309**, 300 (2005).
- [118] M. Eisenbach and L. Giojalas, *Sperm guidance in mammals - an unpaved road to the egg*, Nat. Rev. Mol. Cell Biol. **7**, 276 (2006).
- [119] H. BERG and D. BROWN, *Chemotaxis in escherichia-coli analyzed by 3-dimensional tracking*, Nature **239**, 500 (1972).
- [120] M. F. Copeland and D. B. Weibel, *Bacterial swarming: a model system for studying dynamic self-assembly*, Soft Matter **5**, 1174 (2009).
- [121] H.-R. Jiang, N. Yoshinaga, and M. Sano, *Active motion of a janus particle by self-thermophoresis in a defocused laser beam*, Phys. Rev. Lett. **105**, 268302 (2010).

- [122] W. C. K. Poon, in *Physics Of Complex Colloids*, edited by C. Bechinger, F. Sciortino, and P. Ziherl (IOS Press, 2013).
- [123] S. Ebbens, D. A. Gregory, G. Dunderdale, J. R. Howse, Y. Ibrahim, T. B. Liverpool, and R. Golestanian, *Electrokinetic effects in catalytic platinum-insulator janus swimmers*, EPL **106**, 58003 (2014).
- [124] S. Samin and R. van Roij, *Self-propulsion mechanism of active janus particles in near-critical binary mixtures*, Phys. Rev. Lett. **115**, 188305 (2015).
- [125] A. Würger, *Self-diffusiophoresis of janus particles in near-critical mixtures*, Phys. Rev. Lett. **115**, 188304 (2015).
- [126] S. van Teeffelen and H. Löwen, *Dynamics of a brownian circle swimmer*, Phys. Rev. E **78**, 020101 (2008).
- [127] R. Ledesma-Aguilar, H. Löwen, and J. M. Yeomans, *A circle swimmer at low reynolds number*, The European Physical Journal E **35**, 70 (2012).
- [128] H. BERG and L. TURNER, *Chemotaxis of bacteria in glass-capillary arrays - escherichia-coli, motility, microchannel plate, and light-scattering*, Biophys. J. **58**, 919 (1990).
- [129] W. DiLuzio, L. Turner, M. Mayer, P. Garstecki, D. Weibel, H. Berg, and G. Whitesides, *Escherichia coli swim on the right-hand side*, Nature **435**, 1271 (2005).
- [130] J. Hill, O. Kalkanci, J. L. McMurphy, and H. Koser, *Hydrodynamic surface interactions enable escherichia coli to seek efficient routes to swim upstream*, Phys. Rev. Lett. **98**, 068101 (2007).
- [131] B. M. Friedrich and F. Jülicher, *The stochastic dance of circling sperm cells: sperm chemotaxis in the plane*, New J. Phys. **10**, 123025 (2008).
- [132] C. Lozano, B. ten Hagen, H. Löwen, and C. Bechinger, *Phototaxis of synthetic microswimmers in optical landscapes*, Nat. Commun. **7**, 12828 (2016).
- [133] J. R. Gomez-Solano, S. Samin, C. Lozano, P. Ruedas-Batuecas, R. van Roij, and C. Bechinger, *Tuning the motility and directionality of self-propelled colloids*, Sci. Rep. **7**, 14891 (2017).
- [134] C. Lozano, J. R. Gomez-Solano, and C. Bechinger, *Run-and-tumble-like motion of active colloids in viscoelastic media*, New J. Phys. **20**, 015008 (2018).
- [135] C. Lozano, B. Liebchen, B. ten Hagen, C. Bechinger, and H. Löwen, *Propagating density spikes in light-powered motility-ratchets*, Soft Matter **15**, 5185 (2019).
- [136] C. Lozano and C. Bechinger, *Diffusing wave paradox of phototactic particles in traveling light pulses*, Nat. Commun. **10**, 2495 (2019).
- [137] S. Samin and R. van Roij, *Self-propulsion mechanism of active janus particles in near-critical binary mixtures*, Phys. Rev. Lett. **115**, 188305 (2015).



- 
- [138] T. Bickel, G. Zecua, and A. Würger, *Polarization of active janus particles*, Phys. Rev. E **89**, 050303 (2014).
- [139] M. P. Magiera and L. Brendel, *Trapping of interacting propelled colloidal particles in inhomogeneous media*, Phys. Rev. E **92**, 012304 (2015).
- [140] N. Razin, R. Voituriez, J. Elgeti, and N. S. Gov, *Forces in inhomogeneous open active-particle systems*, Phys. Rev. E **96**, 052409 (2017).
- [141] J. Grauer, H. Löwen, and L. M. C. Janssen, *Spontaneous membrane formation and self-encapsulation of active rods in an inhomogeneous motility field*, Phys. Rev. E **97**, 022608 (2018).
- [142] A. Rosato, K. J. Strandburg, F. Prinz, and R. H. Swendsen, *Why the brazil nuts are on top: Size segregation of particulate matter by shaking*, Phys. Rev. Lett. **58**, 1038 (1987).
- [143] J. D. Weeks, D. Chandler, and H. C. Andersen, *Role of repulsive forces in determining the equilibrium structure of simple liquids*, J. Chem. Phys. **54**, 5237 (1971).
- [144] P. Romanczuk, M. Bär, W. Ebeling, B. Lindner, and L. Schimansky-Geier, *Active brownian particles from individual to collective stochastic dynamics*, Eur. Phys. J. Spec. Top. **202**, 1 (2012).
- [145] J. Elgeti, R. G. Winkler, and G. Gompper, *Physics of microswimmers—single particle motion and collective behavior: a review*, Rep. Prog. Phys. **78**, 056601 (2015).
- [146] R. A. Askey and A. B. O. Daalhuis, in *NIST Handbook of Mathematical Functions*, edited by F. W. J. Olver, D. M. Lozier, R. F. Boisvert, and C. W. Clark (Cambridge University Press, 2010).
- [147] A. Ashkin and J. Dziedzic, *Optical trapping and manipulation of viruses and bacteria*, Science **235**, 1517 (1987).
- [148] D. Grier, *A revolution in optical manipulation*, Nature **424**, 810 (2003).
- [149] M. Wang, H. Yin, R. Landick, J. Gelles, and S. Block, *Stretching DNA with optical tweezers*, Biophys. J. **72**, 1335 (1997).
- [150] J. Palacci, S. Sacanna, A. Abramian, J. Barral, K. Hanson, A. Y. Grosberg, D. J. Pine, and P. M. Chaikin, *Artificial rheotaxis*, Sci Adv. **1**, e1400214 (2015).
- [151] S. C. Takatori, R. De Dier, J. Vermant, and J. F. Brady, *Acoustic trapping of active matter*, Nat. Commun. **7**, 10694 (2016).
- [152] A. M. Wilson, J. C. Lowe, K. Roskill, P. E. Hudson, K. A. Golabek, and J. W. McNutt, *Locomotion dynamics of hunting in wild cheetahs*, Nature **498**, 185 (2013).



- [153] A. Mozaffari, N. Sharifi-Mood, J. Koplik, and C. Maldarelli, *Self-diffusiophoretic colloidal propulsion near a solid boundary*, Phys. Fluids **28**, 053107 (2016).
- [154] A. Daddi-Moussa-Ider, M. Lisicki, C. Hoell, and H. Löwen, *Swimming trajectories of a three-sphere microswimmer near a wall*, J. Chem. Phys. **148**, 134904 (2018).
- [155] A. Daddi-Moussa-Ider, M. Lisicki, A. J. Mathijssen, C. Hoell, S. Goh, J. Bławdziewicz, A. M. Menzel, and H. Löwen, *State diagram of a three-sphere microswimmer in a channel*, J Phys.: Condens. Matter **30**, 254004 (2018).
- [156] S. Mandal, B. Liebchen, and H. Löwen. *Motility-induced temperature difference in coexisting phases*. arXiv:1902.06116, (2019).
- [157] J. Brox, P. Kiefer, M. Bujak, T. Schaetz, and H. Landa, *Spectroscopy and directed transport of topological solitons in crystals of trapped ions*, Phys. Rev. Lett. **119**, 153602 (2017).
- [158] H. L. Partner, R. Nigmatullin, T. Burgermeister, K. Pyka, J. Keller, A. Retzker, M. B. Plenio, and T. E. Mehlstäubler, *Dynamics of topological defects in ion coulomb crystals*, New J. Phys. **15**, 103013 (2013).
- [159] J. Kiethe, R. Nigmatullin, D. Kalincev, T. Schmirander, and T. E. Mehlstäubler, *Probing nanofriction and aubry-type signatures in a finite self-organized system*, Nat. Commun. **8**, 15364 (2017).
- [160] J. W. Swan, P. A. Vasquez, and E. M. Furst, *Buckling instability of self-assembled colloidal columns*, Phys. Rev. Lett. **113**, 138301 (2014).
- [161] S. Huang, G. Pessot, P. Cremer, R. Weeber, C. Holm, J. Nowak, S. Odenbach, A. M. Menzel, and G. K. Auernhammer, *Buckling of paramagnetic chains in soft gels*, Soft Matter **12**, 228 (2016).

